Trabajo Fin de Grado
Grado en Ingeniería Aeroespacial

Conjunction analysis for uncertain objects in close proximity

Autor: Luis Yepes Llorente

Tutor: Rafael Vázquez Valenzuela

Dpto. Ingeniería Aeroespacial y Mecánica de Fluidos
Escuela Técnica Superior de Ingeniería
Universidad de Sevilla

Sevilla, 2021

Ingeniería Aeroespacial
ESI - Universidad de Sevilla

Trabajo Fin de Grado
Grado en Ingeniería Aeroespacial

Conjunction analysis for uncertain objects in close proximity

Autor:
Luis Yepes Llorente

Tutor:
Rafael Vázquez Valenzuela
Profesor Titular

Dpto. Ingeniería Aeroespacial y Mecánica de Fluidos
Escuela Técnica Superior de Ingeniería
Universidad de Sevilla

Sevilla, 2021

Trabajo Fin de Grado: Conjunction analysis for uncertain objects in close proximity

Autor: Luis Yepes Llorente
Tutor: Rafael Vázquez Valenzuela

El tribunal nombrado para juzgar el trabajo arriba indicado, compuesto por los siguientes profesores:

Presidente:

Vocal/es:

Secretario:

acuerdan otorgarle la calificación de:

El Secretario del Tribunal

Fecha:

Agradecimientos

A pesar de que estas son las primeras palabras de mi trabajo, son las últimas que escribo. Y las escribo lleno de felicidad, porque el éxito consiste en conseguir lo que se desea, y la felicidad en disfrutar lo que se consigue. Y con estas últimas palabras pongo un exitoso punto y aparte a mis estudios.

Pero en este rinconcito no voy a hablar de mí. Voy a hablar de todas aquellas personas que me he ido encontrando a lo largo de lo que llevo de vida. Personas que me han dado, tanto suaves empujoncitos, como bruscos empujones, y que me han hecho llegar hasta este punto y convertirme en la persona que soy. Al fin y al cabo, el agradecimiento es la memoria del corazón, y mi Madre siempre dice que tengo muy buena memoria.

Debo comenzar a agradecer, cómo no, a mis Padres. A mi Papá y a mi Mamá. Las primeras personas que memoricé y que han mantenido su puesto con creces. Porque me han dado una educación que ojalá sea yo capaz de transmitir al menos una décima parte a mis hijos. Porque siempre han estado ahí para lo que he necesitado guiándome y aconsejándome, aunque saben que siempre me salgo con la mía. Porque al menos hasta que yo me vaya de este mundo ellos seguirán estando ahí, aunque se hayan mudado definitivamente a mi interior.

Debo agradecer también a mi Hermano, porque gran parte de la educación que he recibido ha sido gracias a él. Siempre ha sido mi persona de referencia y un modelo a seguir. Porque nos tenemos el uno al otro y le quiero mucho aunque nunca se lo diga.

Agradezco también a mis amigos, familia y a todas aquellas personas con las que he compartido momentos de felicidad. Si no existieran esos momentos la vida no tendría sentido, por lo que agradezco enormemente haberme cruzado con vosotros. Con especial mención al Consejo de Sabios.

Agradezco a mi tutor, Rafael, por haber confiado en mí y haberme guiado a lo largo de este trabajo. Porque de no ser por él la calidad del trabajo no hubiese sido ni la mitad. Agradezco también a todos aquellos profesores que han conseguido enseñarme algo a lo largo de mi vida.

Por último, pero no menos importante, te agradezco a ti. A mi lector. Porque sin tu existencia no habría tenido sentido hacer este trabajo. Gracias por dedicar tu tiempo en leer estas palabras.

Resumen global

Título: Análisis de conjunción para objetos inciertos en las proximidades.

Resumen del trabajo: Una vez presentado el problema actual de la basura espacial y definidos los conceptos básicos empleados en el trabajo, se pasa directamente a un análisis de los métodos actuales para computar la probabilidad de colisión entre dos cuerpos.

Se elige en concreto el método desarrollado por Patera. Posteriormente, se comprueba la precisión de dicho método y se analizan las posibles variaciones que rompen con las hipótesis ideales acercando el problema a la realidad. Finalmente se extraen las conclusiones y se propone trabajo futuro.

Palabras clave: Análisis de conjunción, Dilución de la probabilidad, Región de Dilución, Método de Patera.

Conclusiones: El método de Patera es bastante robusto y permite hacer variaciones que rompen con las hipótesis ideales iniciales. Las ecuaciones de HCW son muy útiles porque permiten propagar órbitas con rapidez pero su uso se limita a distancias relativas pequeñas. El tipo de órbita de los cuerpos influye notablemente en las consideraciones a tener en cuenta como los tiempos de encuentro o las perturbaciones a considerar.

Resumen

En un entorno espacial cada vez más denso, la prevención de colisiones se ha convertido en una tarea esencial en las operaciones de los satélites. Para evitar estas posibles colisiones, es necesario determinar una posible conjunción y su incertidumbre asociada. El análisis de conjunción de satélites es la evaluación del riesgo de colisión durante un encuentro cercano entre un satélite y otro objeto en órbita. En la literatura sobre análisis de conjunciones ha surgido un fenómeno contrario a la intuición, la dilución de la probabilidad, en el que, paradójicamente, los datos de menor calidad parecen reducir el riesgo de colisión.

Este trabajo presenta una revisión de los métodos actuales utilizados para estimar la probabilidad de colisión entre dos cuerpos en órbita así como un análisis exhaustivo de los factores a tener en cuenta en este proceso. Se desarrolla el concepto de propagación de la incertidumbre, dilución de la probabilidad y el efecto de las perturbaciones y el ruido.

Abstract

In an increasingly dense space environment, collision avoidance has become an essential task in satellite operations. In order to avoid these possible collisions, it is needed to determine a possible conjunction and its associated uncertainty. Satellite conjunction analysis is the assessment of collision risk during a close encounter between a satellite and another object in orbit. A counterintuitive phenomenon has emerged in the conjunction analysis literature, namely, probability dilution, in which lower quality data paradoxically appear to reduce the risk of collision.

This work presents a review of the current methods used to estimate the probability of collision between two bodies in orbit as well as an exhaustive analysis of the factors to take into account in this process. The concept of uncertainty propagation, probability dilution and the effect of perturbations and noise is developed.

Contents

List of Figures

List of Tables

Notation

P_c	Probability of collision
$\triangle V$	Delta-V
G	Gravitational constant
μ	Gravitational parameter
CM	Center of mass
a	Semimajor axis
p	Orbit parameter (Semi-latus rectum)
e	Eccentricity vector
i	Inclination of the orbit
θ	True anomaly
ω	Argument of periapsis
Ω	Longitude of the ascending node
υ	Ascending node
υ	Descending node
E	Eccentric anomaly
M	Mean anomaly
Υ	First point of Aries
$\overline{\omega}$	Perigee length
u	Latitude argument
λ_T	True length
n	Average orbital speed
U	Gravitational potential
$R_\oplus$	Earth's average radius
J_2	First zonal harmonic
ϕ	Latitude
$\dot{x}$	First time derivative of the variable x
$\ddot{x}$	Second time derivative of the variable x
$\mathbb{R}$	Set of real numbers
$E[X]$ or μ_X	Expected value of the random variable X
pdf	Probability density function
pmf	Probability mass function
cdf	Cumulative density function
σ^2	Variance
σ	Standard deviation
σ_{xy}	Covariance of the random variables X and Y
$exp(x)$	Exponential function e^x
Σ	Covariance matrix
d	Mahalanobis distance
ν	Gaussian white noise
σ_ν^2	Variance of the Gaussian white noise
f_i	Points of the combined hardbody in the inertial frame

f_{i_e}	Points of the combined hardbody in the encounter frame
PR_T	Total probability of collision
PR_I	Differential probability per unit of length
PR_C	Contour integral of the hardbody
PR_R	Collision probability rate

1 Introduction

1.1 Motivation

1.1.1 The current problem of space debris

The Space Age began with the development of many technologies that culminated on October 4, 1957, with the launch of Sputnik I by the Soviet Union, becoming the first artificial satellite in history.

From that moment on, there was a great development and interest about the space sector that has made that today over 6020 rocket launches have been carried out and around 10,680 satellites have been put into orbit. About 6250 of these satellites are still in orbit, with a total of 3900 being active and operating [6].

At each launch, not just the payload, but multiple objects are dropped into space (spent rocket stages, adapters, straps, fairings). The fragmentation of all these objects due to collisions and explosions in orbit leads to an even greater release of space debris. Currently, approximately 34,000 objects larger than 10 centimeters are estimated to be in orbit, with 28,210 of these objects being regularly monitored. On the other hand, with respect to the rest of the smaller objects, statistical estimations assume approximately 1 million objects with a size between 1 millimeter and 1 centimeter and up to 130 million objects with a size smaller than 1 millimeter in Earth orbit. Figure 1.1 shows the evolution of the number of objects in space from the beginning of the Space Age to 2019.

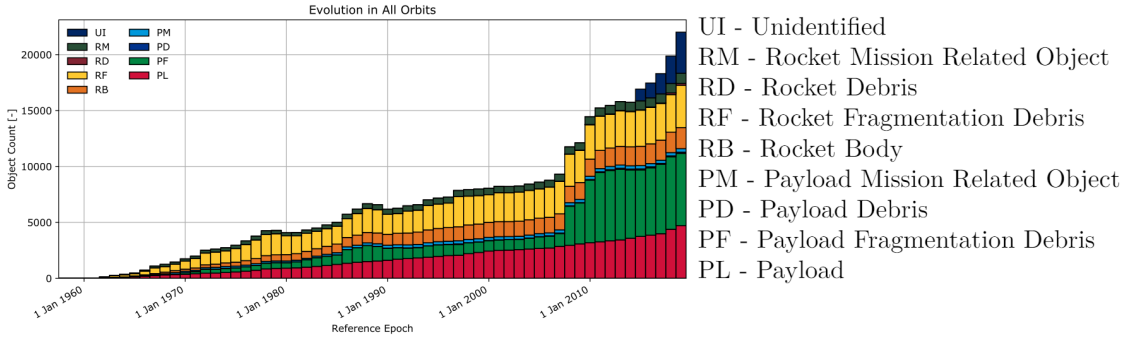

Figure 1.1 ESA 2019 report on space debris - evolution in all orbits. Shows the number of objects of each type in orbit.

A large number of today's space debris is due to fragmentation produced in collisions or explosions. When fragmentation occurs, a cloud of particles is generated that further pollutes the orbit, increasing the risk of collision and generating a chain reaction. To protect spacecraft in this dangerous environment, ESA's Space Debris Office supports operational collision avoidance for ESA missions as well as spacecraft of partner agencies. Every week hundreds of collision warnings

are received from multiple satellites and on average two collision avoidance maneuvers are carried out each year per satellite.

1.1.2 Historical collisions

Two main catastrophes demanded a major concern about space debris, the need to protect satellites, and the adaptation of an international law that allowed to regulate collisions between satellites. These catastrophes took place in 2007 and 2009, justifying the jump in the number of objects in space shown in Figure 1.1.

2007 Chinese Anti-Satellite (ASAT) Test

On January 11, 2007, China launched a ballistic missile from Xichang Space Launch Center [7]. The payload was a kinetic kill vehicle (KKV) that collided with a non-operational Chinese weather satellite, the Fengyun-1C (FY-1C), at an altitude of 863 km, destroying the satellite. Within minutes after the collision, the debris cloud started to spread around the satellite's original orbit. Ten days after the ASAT test, the debris had spread throughout the entire orbit, resulting in a "ring" of debris around the Earth. Three years after the test, the debris spread out, even more, effectively covering much of LEO. Scientists estimate that more than 32,000 small pieces from the event currently remain untracked. The debris from the destruction of the FY-1C currently spreads from an altitude as low as 175 km and as high as 3600 km. This is the largest debris cloud ever generated by a single event in orbit.

According to Celestrak, on January 22, 2007, there were 2864 active or inactive satellites in Earth orbit with known positional data. Of these, 1899 passed through the regime now affected by the debris from the Chinese ASAT test, which represented two-thirds of all payloads in Earth orbit. The first acknowledged maneuver to avoid a piece of debris from the Chinese ASAT test occurred on June 22, 2007, when flight controllers at NASA's Goddard Space Flight Center briefly fired the thrusters on their TERRA satellite to avoid a seven percent chance of being struck the following day. On October 10, 2007, a detailed analysis of the FY-1C debris predicted that just over six percent of the debris would reenter the Earth's atmosphere by 2017 and 79 percent will remain in orbit until 2108.

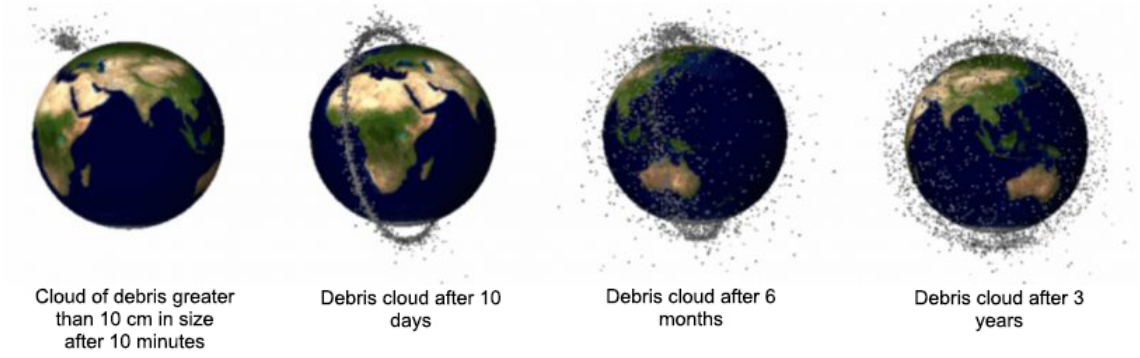

Figure 1.2 Evolution of the debris cloud from the Chinese ASAT Test (taken from [1]).

2009 Iridium-Cosmos Collision

On February 10, 2009, an inactive Russian communications satellite, named Cosmos 2251, collided with an active commercial communications satellite, the Iridium 33, operated by the U.S. company *Iridium Satellite LLC*. The incident occurred approximately 800 kilometers above Siberia. This collision produced at least 2.000 pieces of space debris larger than 10 centimeters and several thousand smaller pieces [8].

Analysis by NASA and outside experts indicate that more than half of the Iridium debris will remain in orbit for at least 100 years. Much of the Cosmos debris will remain in orbit for at least 20 to 30 years, posing a risk to other low-orbiting objects. This was the first unintentional collision in history between satellites.

There was no warning issued of a potential collision between the Iridium 33 and Cosmos 2251 before the collision. However, both the U.S. and Russian military had accurate tracking data on the two satellites before the event, and if analyzed, this data would have shown a very close approach between the two satellites. Calculations made by CelesTrak had expected these two satellites to miss by 584 meters.

In June 2007, the U.S. military had been providing daily warnings to Iridium of potential collisions between its satellites and other objects. However, as a result of the sheer number of these warnings and the inaccuracy of the data provided by the U.S. military, these warnings were stopped at some point before the collision in February 2009.

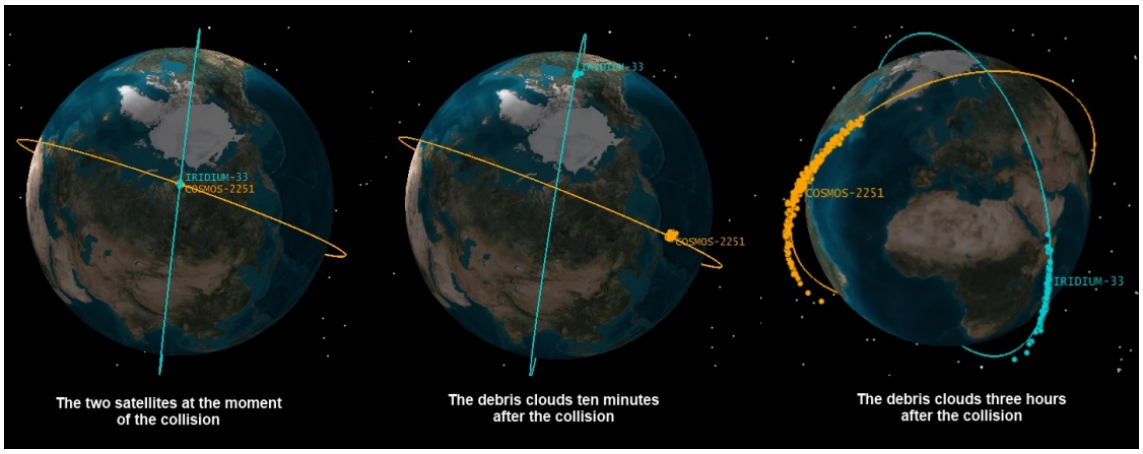

Figure 1.3 Visualization of the crash and subsequent spread of space debris from the Iridium-Cosmos collision (taken from [1]).

International law applicable to the collision is mainly derived from the 1967 Outer Space Treaty and the 1972 Liability Convention. Under these treaties, the "Launching State" is responsible for objects in orbit. According to the common legal definition of Launching State established by these treaties, Russia is the Launching State for the Cosmos 2251. However, it is unclear whether the Launching State for Iridium 33 is Russia, the United States, or Kazakhstan as Iridium 33 was not registered with the United Nations, as required by the 1974 Registration Convention.

The Liability Convention dictates that for damages that occur in orbit, the fault must be determined. Nevertheless, a legal definition does not currently exist for the fault within the context of the Liability Convention. The Liability Convention has also never been formally invoked as all incidents to date that could have resulted in potential claims under the Convention, including the Iridium-Cosmos collision, have been settled by the respective countries outside of the Convention.

This collision and numerous near-misses have renewed calls for mandatory disposal of defunct satellites (typically by deorbiting them, or at minimum, sending them to a graveyard orbit), but no such international law exists as of 2021. Nevertheless, some countries have adopted such a law domestically, such as France in December 2010. The United States Federal Communications Commission (FCC) requires all geostationary satellites launched after March 18, 2002, to commit to moving to a graveyard orbit at the end of their operational life.

1.1.3 How do operators deal with space debris: The example of the ISS

All current active satellites are constantly monitored and any warning sign is notified instantly. Normally, there are two limits that no other body in orbit can exceed without requiring an evasion maneuver or other countermeasure: Exceeding a certain limit in collision probability or exceeding a minimum distance limit. These limits are defined based on the economic cost of losing the satellite and the possible damage that the collision may cause to the rest of the orbiting bodies based on the cost of performing the evasion maneuver. In addition, it is necessary to set limits since the risk is never zero, and otherwise evasive maneuvers would be constantly executed unnecessarily.

The example of the ISS will be presented in this section, since being the satellite with the largest size and most expensive, it is the one with the greatest number of restrictions and information about them [9].

Risk identification

The ISS has *Whipple shielding* [10] to resist damage from small Micrometeoroids and Orbital Debris (MMOD). However, known larger debris with a relevant collision probability are avoided by maneuvering the station.

Personnel at the Joint Space Operations Center (JSpOC), located at Vandenberg Air Force Base, maintains a catalog of objects in orbit based on radar tracking. They screen the ISS trajectory against all other objects in the catalog three times per day and notify the ISS Trajectory Operations and Planning Officer (TOPO) if anything is predicted to pass within a ± 2 km (local vertical) x 25 km x 25 km (local horizontal) volume within the next 72 hours. TOPO uses data from JSpOC to compute the probability of collision P_c.

Maneuver Decision

TOPO continues to refine the probability of collision as new tracking information arrives on both ISS and threat objects. TOPO monitors trends in orbit determination, covariance behavior, miss distance, and P_c. Flight Rules govern when a Debris Avoidance Maneuver (DAM) should be performed to minimize the risk of collision.

P_c threshold to maneuver depends on ISS activities underway or planned in near future. Flight Rules dictate the exceptions to perform a DAM (for example, incoming crewed Soyuz launch requires a higher P_c to guarantee a DAM).

Action thresholds:

- Black: $P_c \geq 1 \cdot 10^{-2}$ (1 in 100)
- Red: $P_c \geq 1 \cdot 10^{-4}$ (1 in 10,000)
- Yellow: $P_c \geq 1 \cdot 10^{-5}$ (1 in 100,000)
- Green: $P_c < 1 \cdot 10^{-5}$ (no action taken)

Maneuver Execution: Pre-determined Debris Avoidance Maneuver (PDAM)

Established in late 2012 and currently the primary method for ISS DAM. Normally, ignition occurs approximately 2 hours and 20 minutes before the closest approach and the dedicated command script (cyclogram) is executed by Mission Control Center – Moscow (MCC-M) or the crew 1 hour before the PDAM ignition. The fixed $\triangle V$ options are:

- 0.3, 0.5, 0.7, 1.0 m/s using aft engines (Progress, Service Module)
- 0.3, 0.5 m/s using Progress docked to DC1-nadir port

1.2 Objectives of this work

The main objective of this work is to present, analyze and develop a method that allows to compute the probability of collision between two bodies given some initial conditions. The information of the bodies in orbit will be provided or obtained from a catalog (position, velocity and a measure of uncertainty), and with this information the probability of collision will be estimated. The method should serve to periodically analyze the bodies that are near the satellite under surveillance and hours before the encounter be able to give an idea of the imminent danger.

For this, a review of the different existing methods will be carried out and the most useful one will be analyzed in depth. The problem of uncertainty, its evolution when propagating bodies in the orbit, and the problem of probability dilution will also be reviewed. Likewise, it will be taken into account how the fact of increasing the size of the bodies or decreasing the minimum distance of encounter affects the estimated collision probability.

In addition, the limitations of the method, its possible simplifications, and the errors associated with any addition that implies seeking a more realistic approach will be analyzed in detail. We will start from an ideal model, with circular or slightly eccentric orbits, and it will be improved by adding the effect of perturbations and other variations of the initial orbit. The analysis will be carried out using both the Keplerian absolute propagator and a linear relative propagator.

Following the structure of the ISS risk prevention system, the identification of collision risk will be studied. The maneuver execution aspect will be left as future work.

1.3 Structure

The structure of this project is defined as follows:

Chapter 1: The context of the space debris problem is explained, the objectives to be met are defined, and the structure of the work is presented.

Chapter 2: The basic concepts of orbital mechanics are introduced, the solution to the two-body problem is developed, the orbital elements and perturbations are presented, a study of the non-sphericity of the Earth is made and the J_2 is studied in depth. Finally, the HCW equations are presented and their validity limit is analyzed.

Chapter 3: The basic concepts of statistics used in this work are introduced, the Gaussian and multivariate normal distribution are presented, the central limit theorem is exposed to justify the use of these distributions, the Monte Carlo method is developed and finally the stochastic processes are mentioned.

Chapter 4: A brief review is made of the current methods that allow estimating the probability of collision between two bodies and finally Patera's method is chosen. This method is developed in depth and tested in different types of encounters to check its validity at the same time as it is compared with an analytical solution and an alternative method based on the Monte Carlo method.
Likewise, an analysis is made of the variables that influence the problem such as the size of the bodies or the present uncertainty, being presented the problem of the probability dilution. Finally, the appropriate limits under which to use this method are analyzed.

Chapter 5: The method is analyzed in depth, adding aspects that bring it closer to reality. First, the method is adapted to the HCW equations by making appropriate considerations. Subsequently with these equations the probability of collision is studied considering that the uncertainty region grows during the propagation of the bodies. Likewise, the effect that the J_2 perturbation causes in the calculation of the collision probability is added and for this the evolution of the uncertainty region is simulated using the Monte Carlo method. Finally, the method is studied with the HCW equations for targets that do not follow circular orbits.

Chapter 6: The conclusions of the project are drawn and future work is proposed.

2 Background material on orbital mechanics

Throughout this chapter, all the physical and mathematical concepts related to orbital mechanics necessary to develop and understand the study of the probability of collision between two bodies are introduced and reviewed. Similarly, a common notation is introduced that will be consistent throughout the project.

2.1 Basic concepts

This section aims to introduce the basic equations of motion and reference frames used in this project to be able to work with them deeper in the next chapters. The two-body problem is developed in detail and finally the perturbations are analyzed.

2.1.1 Two-body problem

The two-body problem consists of predicting the motion of two objects that are considered as point particles. The problem assumes that the two objects interact only with each other; the only force affecting each object comes from the other, and all other objects are ignored.

The most prominent case of the classical two-body problem is the gravitational case (also known as Kepler's problem), which arises in astronomy to predict the orbits of objects such as satellites, planets, and stars. A two-point particle model of such a system almost always describes its behaviour well enough to provide useful information and predictions.

There is also the classical central-force problem, which treats one body as the immobile source of a force acting on another body. One can then focus on the only moving body. This problem, as we will see throughout this chapter, is a simplification of the two-body problem when one of the bodies is much more massive than the other and can therefore be treated as stationary. Although useful results can be obtained, this "one-body problem" is used exclusively as an intermediate step to obtain the solution to the two-body problem.

If one wants to study the motion of three or more bodies that interact with each other, then it is necessary to solve the n-body problem for $n \geq 3$, whose solution cannot be solved in terms of first integrals except in special cases [11].

Newton's Laws of Motion

To pose the two-body problem we will start from the most basic equations of motion given by Newton's laws.

Newton's first law of motion, often referred to as the law of inertia, defines the behaviour of a body in which all the forces are balanced. It states that, if all the forces are balanced (net force equals zero), the acceleration of that body will be zero.

Then, according to Newton, a body will only accelerate if there is a net force acting on it. Newton's second law of motion defines the behaviour of the body in this case. It states that the acceleration of a point mass depends on two variables: The net force acting upon the particle and its mass. Its relation is as follows:

The acceleration of a point mass produced by a net force is directly proportional to the magnitude of the net force, in the same direction as the net force, and inversely proportional to the mass of the particle.

$$\sum \vec{F} = m \cdot \vec{a} \tag{2.1}$$

Then, if we know all the forces that are exerted on a body and its mass distribution, we can obtain its acceleration. By integrating its acceleration we can determine its velocity and position along time. This means that the motion of the body is then uniquely defined by its mass distribution and the forces acting on it once an initial state has been set.

Note that for these laws to be applicable, an inertial reference frame must be used; this is a reference frame in which if a body does not experience the action of any active force, its acceleration is zero (and therefore Newton's first law is fulfilled).

Newton's gravitational law

Newton's gravitational law is the force with the greatest magnitude that acts on orbital bodies.

$$F = \frac{G \cdot m_1 \cdot m_2}{r^2} \tag{2.2}$$

The force F describes the attraction between two point masses m_1 and m_2 as proportional to the product of the masses and inversely proportional to the square of its relative distance $\vec{r}$.

Hence, one first approach to compute the trajectory of an orbiting body around another is by assuming this force to be exclusively the net force acting on it.

To get an expression that is feasible to solve analytically, two important assumptions are made:

- The system is considered isolated from the rest of the Universe (there is no force other than the mutual gravitational attraction between the two bodies).
- The masses can be considered as points located at the center of mass of each body.

This last assumption is given by the shell theorem proved by Newton:

A rigid body with a spherical shape and constant density generates the same gravitational field as a particle, located in the center of said sphere, with the same mass as the body.

These assumptions define the two-body problem. However, its solution does not reflect the real behaviour of orbiting bodies. A good approach to compute it is to obtain a solution using these assumptions and subsequently take into account the action of the other minor forces that disturb the solution of the two-body problem. These minor forces are called perturbations and can include a third (fourth, fifth, etc.) body, atmospheric or solar drag, and the off-center attraction of an oblate or otherwise misshapen body.

The gravitational force exerted on each mass, in vector form, is given by:

$$\vec{F_1} = \frac{G \cdot m_1 \cdot m_2}{r^2} \cdot \frac{\vec{r}}{r} \tag{2.3}$$

$$\vec{F_2} = -\frac{G \cdot m_1 \cdot m_2}{r^2} \cdot \frac{\vec{r}}{r} \tag{2.4}$$

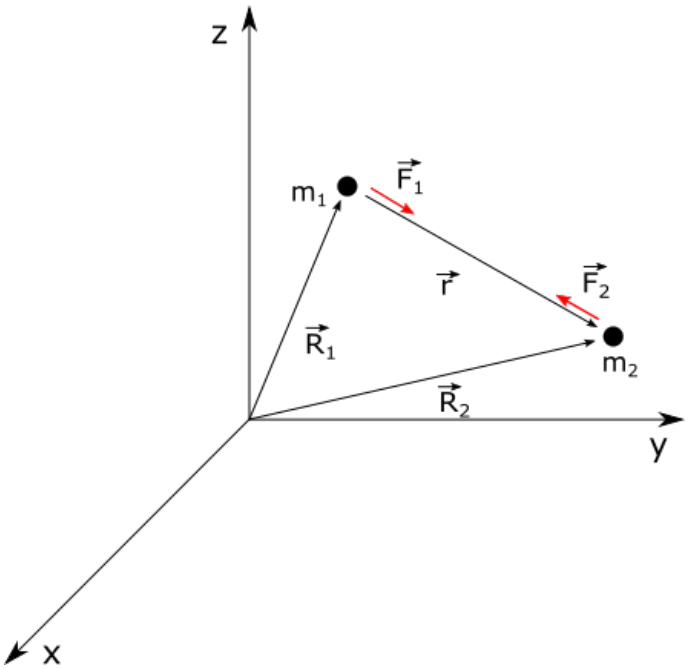

Figure 2.1 Newton's gravitational force between two isolated masses.

Where $\vec{r}$ is the position vector from the first body to the second one $\vec{r} = \vec{R}_2 - \vec{R}_1$ and G is the gravitational constant $G = 6.674 \cdot 10^{-11} \frac{N \cdot m^2}{kg^2}$.

Introducing the force acting on the first body (2.3) and the second one (2.4) into (2.1):

$$m_1 \cdot \ddot{\vec{R}}_1 = \vec{F}_1 \;\rightarrow\; \ddot{\vec{R}}_1 = \frac{G \cdot m_2}{r^2} \cdot \frac{\vec{r}}{r} \tag{2.5}$$

$$m_2 \cdot \ddot{\vec{R}}_2 = \vec{F}_2 \;\rightarrow\; \ddot{\vec{R}}_2 = -\frac{G \cdot m_1}{r^2} \cdot \frac{\vec{r}}{r} \tag{2.6}$$

If we use the definition of $\vec{r}$, we get the differential equation for the relative distance between the bodies:

$$\ddot{\vec{r}} = \ddot{\vec{R}}_2 - \ddot{\vec{R}}_1 = -G \cdot (m_1 + m_2) \cdot \frac{\vec{r}}{r^3} = -\mu \cdot \frac{\vec{r}}{r^3} \tag{2.7}$$

Where μ is the gravitational parameter defined as:

$$\mu = G \cdot (m_1 + m_2) \tag{2.8}$$

Equation (2.7) is the differential equation that defines the evolution of the relative distance between the bodies. However, to fully characterize the movement of each body a further step is necessary.

Let us call $\vec{R}_{CM}$ to the position of the center of mass defined by:

$$\vec{R}_{CM} = \frac{m_1 \cdot \vec{R}_1 + m_2 \cdot \vec{R}_2}{m_1 + m_2} \tag{2.9}$$

Then, the differential equation of the position of the center of mass is given by:

$$\ddot{\vec{R}}_{CM} = \frac{m_1 \cdot \ddot{\vec{R}}_1 + m_2 \cdot \ddot{\vec{R}}_2}{m_1 + m_2} = \frac{m_1 \cdot \frac{G \cdot m_2}{r^2} \cdot \frac{\vec{r}}{r} - m_2 \cdot \frac{G \cdot m_1}{r^2} \cdot \frac{\vec{r}}{r}}{m_1 + m_2} = 0 \tag{2.10}$$

Therefore, the position of the center of mass follows a uniform rectilinear motion. If we displace the origin of the reference frame to center of mass, the new reference frame remains inertial. In this new frame (Figure 2.2) the position of the bodies is given by:

$$\vec{r}_1 = \vec{R}_1 - \vec{R}_{CM} = \left(\vec{R}_1 - \vec{R}_2\right)\frac{m_1}{m_1+m_2} = -\vec{r}\frac{m_2}{m_1+m_2} \tag{2.11}$$

$$\vec{r}_2 = \vec{R}_2 - \vec{R}_{CM} = \left(\vec{R}_2 - \vec{R}_1\right)\frac{m_2}{m_1+m_2} = \vec{r}\frac{m_1}{m_1+m_2} \tag{2.12}$$

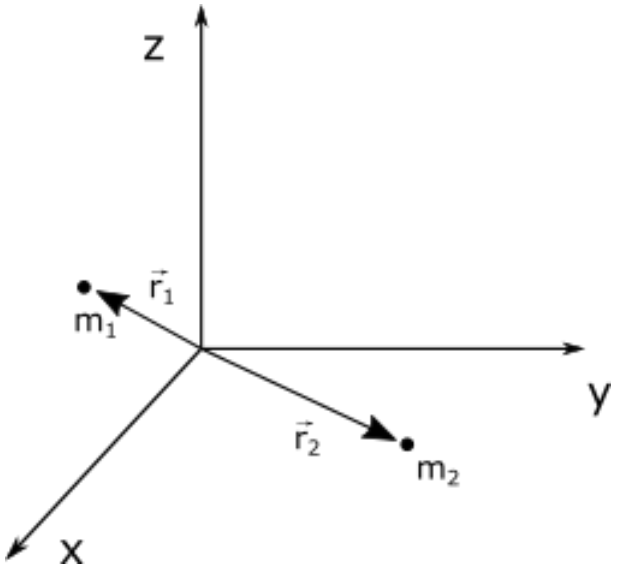

Figure 2.2 Origin of the inertial reference frame placed at the center of mass.

Hence, once equation (2.7) is solved, the position of each body can be obtained applying equations (2.11) and (2.12).

Note that if the mass of the first body is much greater than the one of the second body, the center of mass is located practically in the center of the massive body. In that case, we can approximate the value of the gravitational parameter (2.13) and study the relative motion of the small body by assuming the center of mass in the massive body and approximating $\ddot{\vec{r}} \approx \ddot{\vec{R}}_2$, which means that the massive body isn't affected by the gravity of the small one and therefore the small one orbits around the massive one.

$$\mu = G\cdot(m_1+m_2) \approx G\cdot m_1, \quad if\ m_1 \gg m_2 \tag{2.13}$$

Solution to the two-body problem

Equation (2.7) is a system of nonlinear ordinary differential equations that can be developed as:

$$\ddot{\vec{r}} = -\mu\cdot\frac{\vec{r}}{r^3} \rightarrow \begin{cases} \ddot{x} &= -\mu\dfrac{x}{(x^2+y^2+z^2)^{3/2}} \\ \ddot{y} &= -\mu\dfrac{y}{(x^2+y^2+z^2)^{3/2}} \\ \ddot{z} &= -\mu\dfrac{z}{(x^2+y^2+z^2)^{3/2}} \end{cases} \tag{2.14}$$

Which is easy to be solved numerically. In addition, it is possible to get an analytic solution by performing the appropriate operations [12]. It is then shown that the orbits of the planets are flat and follow the equation of a conic:

$$r(\theta) = \frac{p}{1+e\cos\theta} \tag{2.15}$$

Where:

- $\vec{e}$ is Laplace's vector or eccentricity vector. It is a vector that points from the origin of coordinates towards the point of the minimum distance between the bodies (*periapsis*).

- $p > 0$ is called "parameter" and it is defined by $p = h^2/\mu$, with $\vec{h}$ being the specific kinetic moment $\vec{h} = \vec{r} \times \vec{v}$.
- θ is the true anomaly and it is defined by the counter-clockwise angle between $\vec{r}$ and $\vec{e}$ such that $\vec{r} \cdot \vec{e} = r \cdot e \cdot \cos(\theta)$.

The parameter p is related to the amplitude of the orbit. For elliptical orbits, it is usually expressed as $p = a(1-e^2)$, where a is the semimajor axis of the ellipse. On the other hand, the eccentricity e defines the type of conic:

- If $e = 0$ the conic is a circunference.
- If $e \in (0,1)$ the conic is an ellipse.
- If $e = 1$ the conic is a parabola.
- if $e > 1$ the conic is a hyperbola.

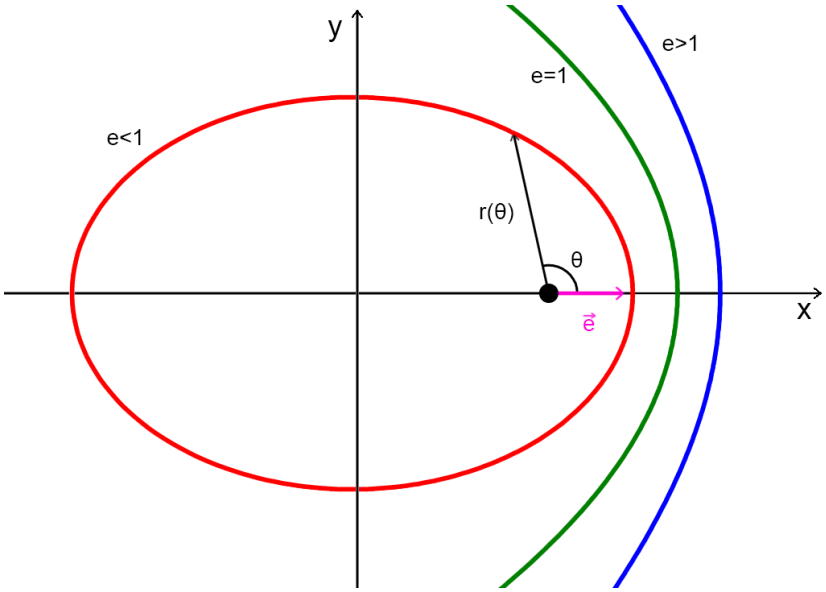

Figure 2.3 Types of conics as a function of eccentricity. Note how the eccentricity points towards the periapsis (defined as the positive x-axis).

Note that equation (2.15) defines the orbit of a body in its plane of motion with the x-axis pointing to the periapsis. However, in case of wanting to represent an orbit in a three-dimensional system not oriented with the plane of motion, it is necessary to define a series of additional parameters. We define the **orbital elements** as the set of parameters that fully characterise the orbit of a body with respect to a massive one.

First of all, we define the Geocentric Equatorial Frame. It is the most used inertial reference frame when studying the movement of bodies around the Earth. The origin of this reference frame is the center of the Earth.

The fundamental plane is the plane that contains the Earth's equator and its normal is defined as the z-axis (pointing towards the North Pole). This plane is defined by two directions:

- The primary direction (x-axis) points towards the vernal equinox (Υ-point).
- The y-axis is defined by a right-handed convention.

This reference frame does not rotate with the Earth. In fact, the Earth rotates around the z-axis.

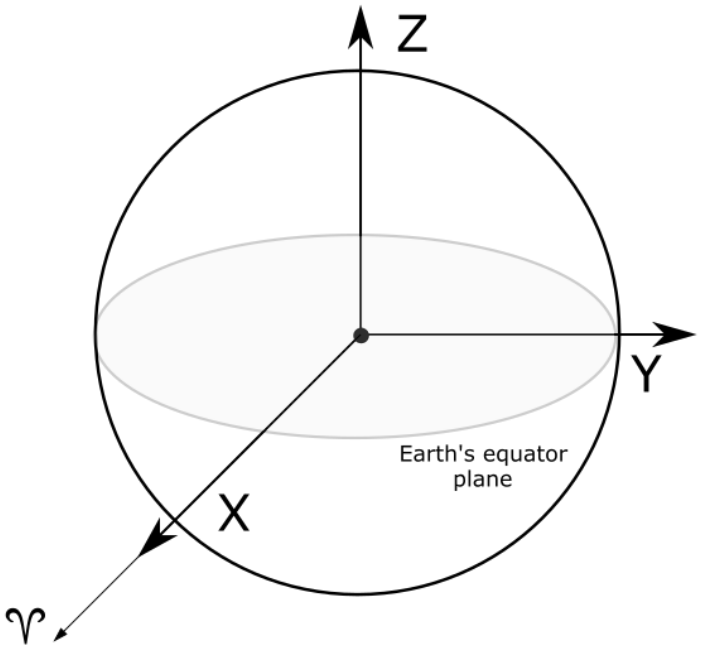

Figure 2.4 Geocentric Equatorial Frame.

If the plane of the orbit is intersected with the fundamental plane, the node line is obtained. The orbit in turn cuts the line of nodes at two points, the nodes. The one where the path "ascends" (from bottom to top) is the ascending node ☊; the other one is the descending node ☋ (see Figure 2.5).

- The first parameter that is then defined is the longitude of the ascending node Ω. It is defined as the counterclockwise angle between the first point of Aries Υ and the ascending node ☊.
- The next additional parameter is the argument of periapsis ω, which is defined as the angle in the direction of motion between the node line and the eccentricity vector (apse line).
- The last necessary parameter is the inclination $i \in [0,\pi]$, defined as the counterclockwise angle between the orbital plane and the fundamental plane (around the node line) measured at the ascending node ☊.

Hence, the orbital elements of an orbit are the following: a (or p), e, i, ω, Ω and θ. However, there are special cases in which some elements are not well defined.

- Equatorial elliptical orbits: Neither Ω nor ω is defined since the node line is undefined. Both elements are combined at the angle $\bar{\omega}$ (perigee length) defined as the angle between Υ and $\vec{e}$ counterclockwise such that $\bar{\omega} = \Omega + \omega$.
- Non-equatorial circular orbits: Neither ω nor θ is defined as there is no apse line. They are replaced by the angle $u = \omega + \theta$ (latitude argument) that measures the angle of the body from the ascending node ☊ in the direction of movement.
- Equatorial circular orbits: There is neither node line nor apse line. Therefore neither Ω, nor ω, nor θ are well defined. They are replaced by $\lambda_T = \Omega + \omega + \theta$ (true length), the angle between the body and the first point of Aries Υ measured counterclockwise.

It should be noted that from (2.7) to (2.15) the influence of time has been lost. With five elements the orbit is completely defined and with a sixth, the position of the body in the orbit is specified. θ has been used but this element can be written as a function of time and thus regain time dependency.

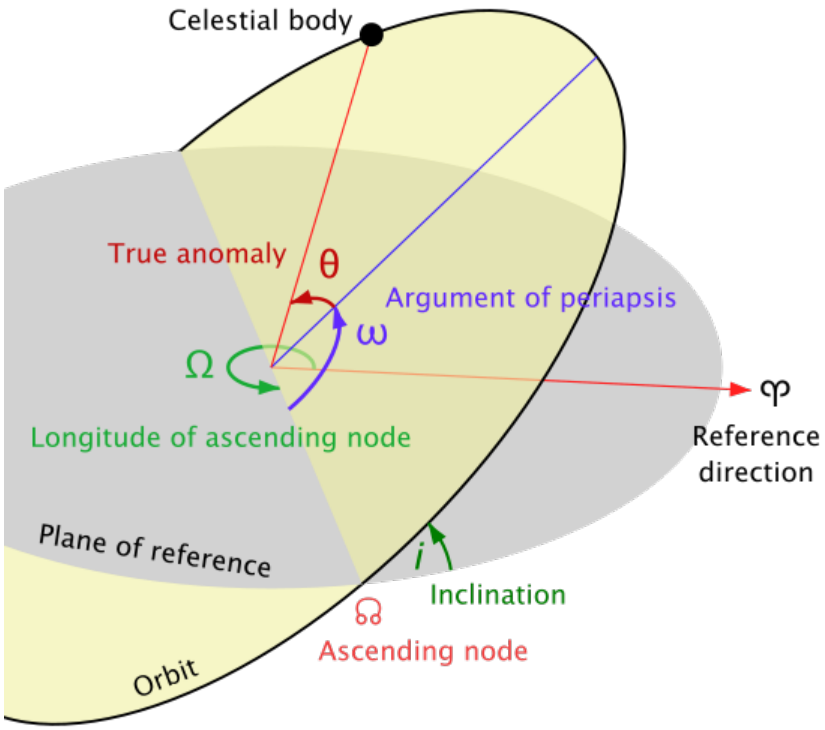

Figure 2.5 Intersection between the orbital plane and a reference plane showing the orbital elements.

For the elliptical case, Kepler's equation (2.16) makes it possible to relate the angle traveled with the time taken:

$$M = E - e \cdot \sin E \tag{2.16}$$

Where E is the eccentric anomaly defined geometrically according to Figure 2.6 and given by:

$$\tan\frac{\theta}{2} = \sqrt{\frac{1+e}{1-e}}\tan\frac{E}{2} \tag{2.17}$$

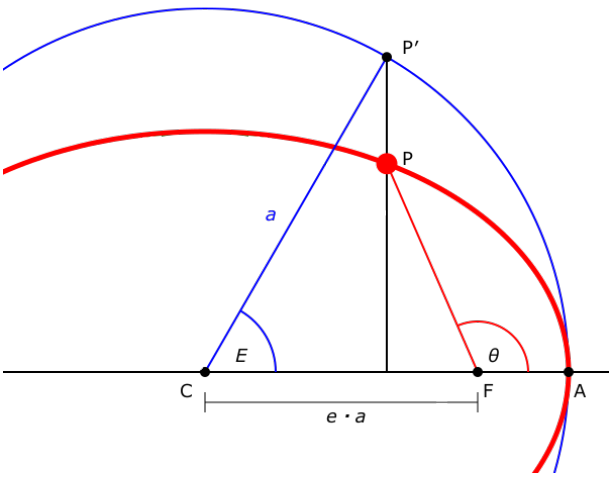

Figure 2.6 Geometric relation between θ and E.

And M is the mean anomaly defined as the angle that would be traveled in a $\triangle t$ if the orbit were circular:

$$M = n \cdot \triangle t \tag{2.18}$$

- $n = \frac{\mu}{a^3}$ is the average orbital speed. This velocity coincides with the actual angular velocity in the case of circular orbits.
- $\triangle t$ is the time elapsed since the last passage through the periapsis.

There is a variation of Kepler's equation that allows solving the hyperbolic case and for the parabolic case, Barker's equation is used. For the circular case, the true anomaly θ can be directly related to the time $\triangle t$ through the average orbital speed n.

2.1.2 Perturbations

As mentioned above, orbiting bodies follow slightly different trajectories than those estimated by the two-body problem. This is due to the effect of perturbations. The perturbations are nothing more than the rest of the forces that are exerted on the bodies and that break with the basic hypotheses of two isolated point bodies. Perturbations can produce on the orbital elements secular variations, that is, they tend to increase or decrease an orbital element constantly, periodical variations, causing the values to oscillate around a mean value, or both.

In general, four main perturbations are taken into account:

- **Non-spherical gravity:** The Earth is not a perfect sphere, nor is its mass evenly distributed within it. This makes the point-mass model of gravity inaccurate for orbits around Earth.
- **Third body perturbations:** The gravitational forces of third bodies can cause perturbations in an orbit. For example, the Sun and the Moon cause perturbations in the orbits around the Earth. These forces are modeled in the same way that gravity is modeled for the primary body by a simulation of n bodies.
- **Solar radiation:** The pressure of solar radiation (SRP) causes perturbations to the orbits.
- **Atmospheric drag:** The primary non-gravitational force acting on satellites in low Earth orbit (LEO) is atmospheric drag. This force will act opposite to the direction of velocity and remove energy from the orbit.

The effect that these perturbations have on the orbital elements is shown in Table 2.1. **P** refers to periodical and **S** to secular.

Table 2.1 Type of variation that each perturbation exerts on each orbital element [5].

	Non-spherical Gravity		Third Body	Atmospheric Drag	Solar Radiation
	Zonal	Sectorial			
a	P	P	P	P & S	P
e	P	P	P	P & S	P
i	P	P	P	P & S	P
Ω	P & S	P	P & S	P	P & S
ω	P & S	P	P & S	P	P & S
M	P & S	P	P & S	P	P & S

To deal with perturbations there are essentially two methodologies:

1. **General perturbations method:** Uses the orbital elements as the base, studying their variation with time. $\vec{\alpha} = [a,e,i,\Omega,\omega,M]$ is defined as the vector of orbital elements of an orbit under $\vec{\gamma_P}$ perturbations and the non-Keplerian orbit is obtained by solving $\dot{\vec{\alpha}} = \vec{F}(\vec{\alpha},\vec{\gamma_P})$. The difficulty is to model that $\vec{F}(\vec{\alpha},\vec{\gamma_P})$ function.
2. **Method of special perturbations:** Does not use orbital elements but directly the equations of motion. In turn, it is divided into two possible ways of treating the problem:

a) **Encke's method:** Computes a direct solution of the equations of motion, including perturbations and so many bodies as necessary. It is the most used nowadays.

b) **Cowell's method:** Solves the equations for a correction δr over a reference solution of the two-body problem $\ddot{\vec{r}} = -\mu \frac{\vec{r}}{r^3}$. If the correction grows, it is necessary to recalculate the reference solution. Little used today.

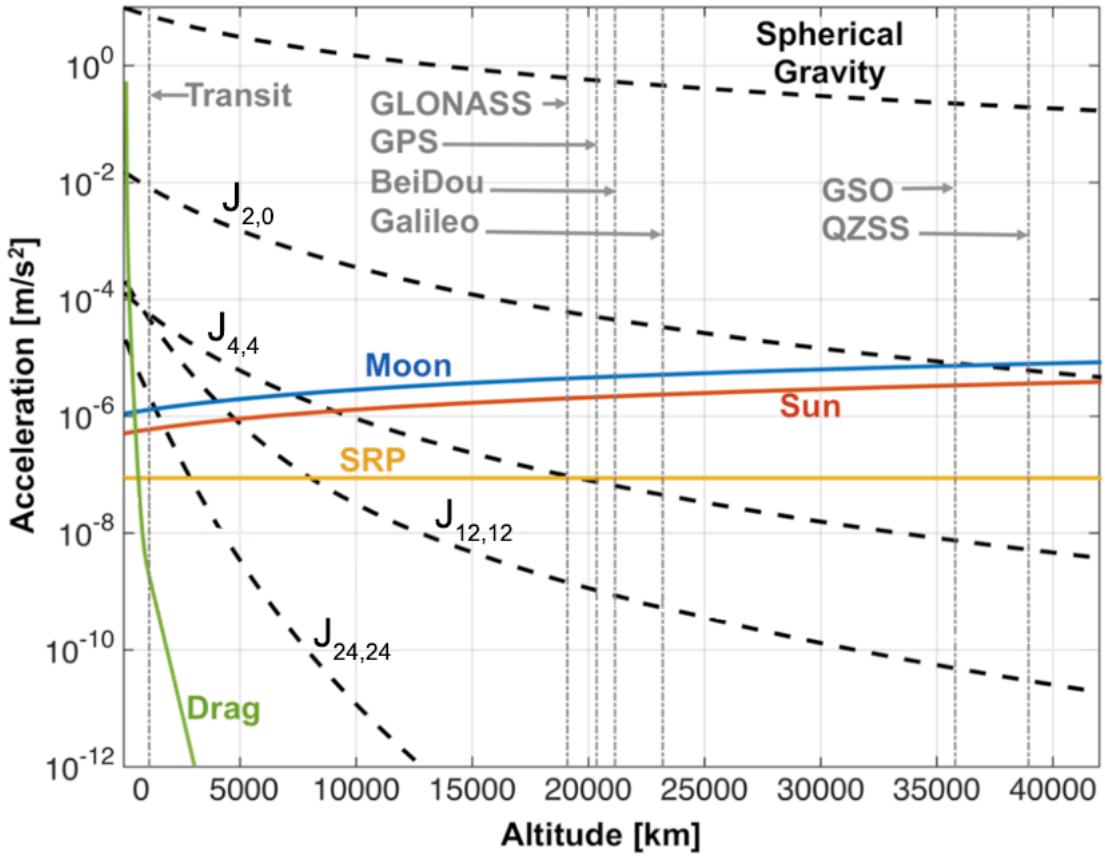

Figure 2.7 Breakdown of the acceleration suffered by an orbiting body around the Earth as a result of the forces acting on it as a function of height (edited from [2]).

Figure 2.7 shows a breakdown of the acceleration suffered by an orbiting body around the Earth as a result of the forces acting on it as a function of height. Until now, the only acceleration that had been considered is the one due to the supposed spherical Earth's gravitational field, that is, $\ddot{r} = \frac{G \cdot M}{r^2}$.

The most remarkable perturbation is the drag force: at low altitude it is the perturbation of greatest intensity but nevertheless its force is rapidly diluted with increasing height. Also noteworthy is the consideration that the earth is not completely spherical, which is the most powerful perturbation for all orbits. These perturbations due to non-sphericity are named as $J_{n,m}$, and its definition is discussed in detail below.

2.2 Non-spherical gravity

As the earth is not actually completely spherical, its gravitational potential is not constant for the same altitude. It depends on the region under consideration. The first step in modeling the perturbation is to obtain the analytical function of the potential energy created by a body of generic shape. Later, with the gravitational potential we can obtain the acceleration by making $\vec{a} = \frac{\partial \vec{U}}{\partial \vec{r}}$

and thus be able to model said force. Equation (2.19) shows the gravitational potential created by a body of generic shape:

$$U = \frac{\mu}{r}\left[1 - \sum_{n=2}^{\infty}\sum_{m=0}^{n} J_{n,m}\left(\frac{R_{\oplus}}{r}\right)^{n} p_{n,m}(sin(\phi)) \cdot cos\left(m(\lambda - \lambda_{n,m})\right)\right] \tag{2.19}$$

This equation is made up of the subtraction of two terms. The first term is $\frac{\mu}{r}$ and corresponds to the gravitational potential created by a sphere, that is, the spherical gravitational potential. The other is the sum of the spherical harmonics, which are corrections to the spherical model that allow characterizing the generic model.

Likewise, $J_{n,m}$ and $\lambda_{n,m}$ are coefficients related to the harmonic (n,m), ϕ is the body's latitude and $p_{n,m}(x)$ is Legendre's associated polynomial whose grade is n and order m. The mathematical expression of this polynomial is the following:

$$p_{n,m}(x) = \frac{(-1)^m}{2^n \cdot n!}(1-x^2)^{m/2}\frac{d^{n+m}}{dx^{n+m}}(x^2-1)^n \tag{2.20}$$

For $m = 0$, Legendre's associated polynomial takes the form of Legendre's polynomial:

$$p_n(x) = \frac{1}{2^n \cdot n!}\frac{d^n}{dx^n}(x^2-1)^n \tag{2.21}$$

Depending on the combination of n and m, we distinguish between three harmonics: zonal $(m = 0)$, sectorial $(n = m)$ and tesseral $(n \neq m)$. The zonal harmonics depend only on latitude. The sectorial harmonics depend both on latitude and longitude, though their sign is only dependent on longitude. The tesseral harmonics take values and signs that change regularly with respect to latitude and longitude, forming a chessboard-style pattern. Its graphical interpretation is illustrated in Figure 2.8.

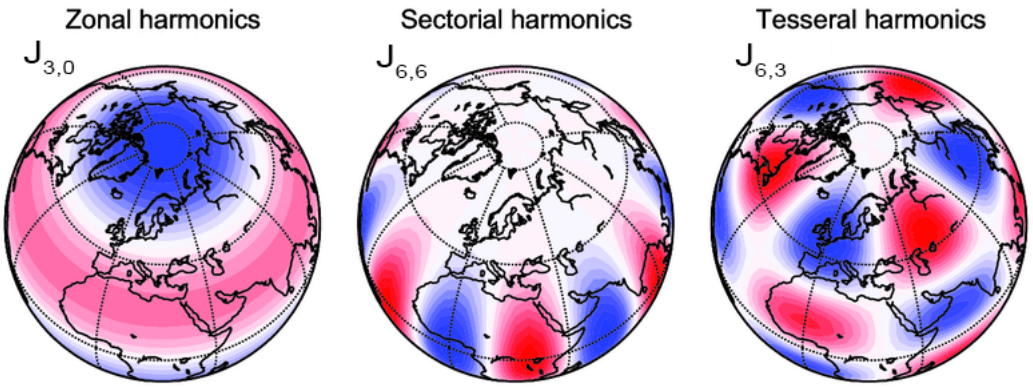

Figure 2.8 Graphical representation of zonal, sectorial and tesseral harmonics of the Earth (edited from [3]).

2.2.1 Earth's zonal harmonics

The effect of the zonal harmonics will be studied, which involves the idea of the symmetry of revolution of the Earth. Then, making $m = 0$, equation (2.19) reduces to:

$$U = \frac{\mu}{r}\left[1 - \sum_{n=2}^{\infty} J_n\left(\frac{R_{\oplus}}{r}\right)^{n} p_n\left(sin(\phi)\right)\right] \tag{2.22}$$

The coefficients J_n are the zonal harmonics (also named as $J_{n,0}$). The first harmonics are the most important. In the case of the Earth, its values are:

$$\begin{aligned} J_2 &= 1{,}083 \cdot 10^{-3} \\ J_3 &= -2{,}534 \cdot 10^{-6} \\ J_4 &= -1{,}620 \cdot 10^{-6} \\ J_5 &= -2{,}273 \cdot 10^{-7} \\ &\dots \end{aligned}$$

Due to the decrease in order of magnitude, a frequently used model is to neglect all harmonics except the second one (J_2), which is equivalent to consider the Earth as an ellipsoid of revolution (sphere flattened by the poles). This is what is called the J_2 model.

J_2 model

Therefore, the gravitational potential considering exclusively the J_2 turns out to be:

$$U = \frac{\mu}{r}\left[1 + \frac{J_2}{2}\left(\frac{R_\oplus}{r}\right)^2 (1 - 3sin^2(\phi))\right] \tag{2.23}$$

$$U_{J_2} = \frac{\mu}{r} \cdot \frac{J_2}{2}\left(\frac{R_\oplus}{r}\right)^2 (1 - 3sin^2(\phi)) \tag{2.24}$$

Taking into account the following geometric relationships between the latitude ϕ and the different coordinates r_x, r_y, r_z of the inertial geocentric reference system:

$$\begin{aligned} r &= \sqrt{r_x^2 + r_y^2 + r_z^2} \\ sin(\phi) &= \frac{r_z}{r} \\ cos(\phi) &= \frac{\sqrt{r_x^2 + r_y^2}}{r} \end{aligned}$$

We can calculate the partial derivatives of the gravitational potential in each direction and thus compute the acceleration due to J_2:

$$a_x = \frac{\partial U_{J_2}}{\partial r_x} = -\frac{3J_2\mu R_\oplus^2 r_x}{2r^5}\left(1 - \frac{5r_z^2}{r^2}\right) \tag{2.25}$$

$$a_y = \frac{\partial U_{J_2}}{\partial r_y} = -\frac{3J_2\mu R_\oplus^2 r_y}{2r^5}\left(1 - \frac{5r_z^2}{r^2}\right) \tag{2.26}$$

$$a_z = \frac{\partial U_{J_2}}{\partial r_z} = -\frac{3J_2\mu R_\oplus^2 r_z}{2r^5}\left(1 - \frac{5r_z^2}{r^2}\right) \tag{2.27}$$

Once the effect of J_2 is obtained, we can add said acceleration term to the differential equation of motion to compute the real trajectory.

$$\ddot{\vec{r}} = -\mu\frac{\vec{r}}{r^3} + \vec{a}_{J_2} \tag{2.28}$$

In the same way that the acceleration due to J_2 has been obtained, the acceleration due to the other harmonics should be obtained. The same applies to the rest of the perturbations.

Thus, once each and every one of the accelerations has been modeled, all that has to be done is to introduce them into the differential equation of motion. Thanks to the computational power of our days, its resolution is very fast and efficient, which is why Encke's method is the most used nowadays.

2.3 Hill-Clohessy-Wiltshire (HCW) equations

The Hill-Clohessy-Wiltshire (HCW) equations of motion are a simplified model for the orbital relative motion of a secondary spacecraft with respect to a primary one. The HCW equations of motion assume that the primary spacecraft is in a circular orbit around a massive central body and the secondary spacecraft is orbiting at a close distance to the target.

When only the movement of a second body with respect to a first one is studied, the first body is usually named "target" and the second body is named "chaser".

The HCW equations of motion were originally stated in a nonlinear form in G.W. Hill's seminal work on the motion of relative objects in orbit [13] and later linearized by W.H. Clohessy and R.S Wiltshire [14].

These equations do not account for any additional forces, such as non-point-mass gravitational perturbations, other massive bodies, or environmental forces (atmospheric drag and solar radiation pressure). They are obtained by introducing the relative position of the two bodies into the equation of motion (2.7).

The relative position is centered in the target by using the LVLH reference frame, which is a non-inertial rotating frame really useful to study the position of other bodies that orbit close to a primary one.

Once the position of the target is known in the Geocentric Equatorial Frame, this local frame can be defined as:

- X-Axis: It is defined along the position vector $\vec{r}$ of the target. It gives the distance of other bodies to the center of the orbit from the target's point of view.
- Z-Axis: It is normal to the orbit plane. It gives the upwards distance from other bodies that have a different orbital plane.
- Y-Axis: It is normal to the XZ plane completing a right-handed reference frame. If the orbit of the target is circular (eccentricity equals zero), then it points toward the direction of its velocity. It gives information about the front distance from the target.

$$\vec{i}_{\mathrm{LVLH}} = \frac{\vec{r}}{\|\vec{r}\|} \tag{2.29}$$

$$\vec{k}_{\mathrm{LVLH}} = \frac{\vec{r} \times \vec{v}}{\|\vec{r} \times \vec{v}\|} \tag{2.30}$$

$$\vec{j}_{\mathrm{LVLH}} = \vec{k}_{\mathrm{LVLH}} \times \vec{i}_{\mathrm{LVLH}} \tag{2.31}$$

The HCW equations of motion are only applicable when two general conditions are met:

- The distance between the target and the chaser is small when compared to the distance between the target and both spacecraft's shared central body.
- The target's orbit is circular.

The following equations are the linearized differential equations of the motion of the chaser body with respect to the target in the LVLH reference frame (HCW equations):

$$\ddot{x} = 3n^2 \cdot x + 2n \cdot \dot{y} \tag{2.32}$$

$$\ddot{y} = -2n \cdot \dot{x} \tag{2.33}$$

$$\ddot{z} = -n^2 \cdot z \tag{2.34}$$

Where n is the orbital rate of the target body $n = \sqrt{\frac{\mu}{a^3}}$.

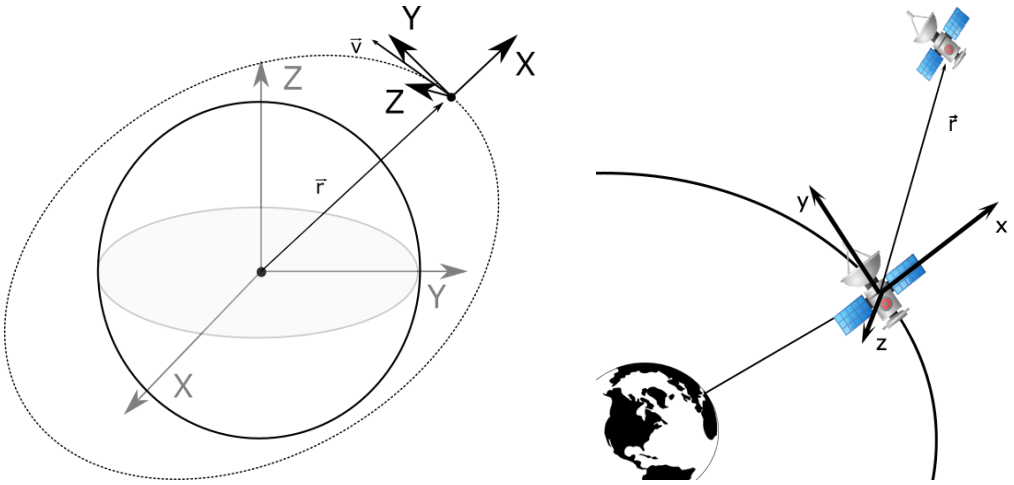

Figure 2.9 LVLH Frame.

As the equations are linear, they can be solved algebraically; first, by posing them as a first-order system:

$$\frac{d}{dt}\begin{bmatrix} x \\ y \\ z \\ \dot{x} \\ \dot{y} \\ \dot{z} \end{bmatrix} = \begin{bmatrix} 0 & 0 & 0 & 1 & 0 & 0 \\ 0 & 0 & 0 & 0 & 1 & 0 \\ 0 & 0 & 0 & 0 & 0 & 1 \\ 3n^2 & 0 & 0 & 0 & 2n & 0 \\ 0 & 0 & 0 & -2n & 0 & 0 \\ 0 & 0 & -n^2 & 0 & 0 & 0 \end{bmatrix} \cdot \begin{bmatrix} x \\ y \\ z \\ \dot{x} \\ \dot{y} \\ \dot{z} \end{bmatrix} \tag{2.35}$$

Whose solution, being x_0,y_0,z_0,$\dot{x}_0$,$\dot{y}_0$,$\dot{z}_0$ the initial conditions, can be expressed as:

$$\begin{bmatrix} x \\ y \\ z \\ \dot{x} \\ \dot{y} \\ \dot{z} \end{bmatrix} = \begin{bmatrix} 4-3\cos(nt) & 0 & 0 & \frac{\sin(nt)}{n} & \frac{2(1-\cos(nt))}{n} & 0 \\ 6\sin(nt)-6nt & 1 & 0 & \frac{2\cos(nt)-2}{n} & \frac{4\sin(nt)-3nt}{n} & 0 \\ 0 & 0 & \cos(nt) & 0 & 0 & \frac{\sin(nt)}{n} \\ 3n\sin(nt) & 0 & 0 & \cos(nt) & 2\sin(nt) & 0 \\ 6n\cos(nt)-6n & 0 & 0 & -2\sin(nt) & 4\cos(nt)-3 & 0 \\ 0 & 0 & -n\sin(nt) & 0 & 0 & \cos(nt) \end{bmatrix} \cdot \begin{bmatrix} x_0 \\ y_0 \\ z_0 \\ \dot{x}_0 \\ \dot{y}_0 \\ \dot{z}_0 \end{bmatrix} \tag{2.36}$$

Note that $y(t)$ is the only term that grows linearly with respect to time whereas the other terms are periodic.

If the particular initial condition $x_0 = -\frac{\dot{y}_0}{2n}$ is met, there are only periodic terms, this is, the chaser "orbits" around the target.

Limits of HCW equations

In this subsection, the limit of validity of the HCW linearized equations will be analyzed, estimating up to what relative distance values these equations can be used without deviating too much from the real behaviour.

The relative position given by solving the equation of motion (2.7) for both target and chaser expressed in the LVLH system will be compared with that given directly by the solution of the HCW equations. Two satellites in LEO will be simulated starting at a small relative distance and moving apart.

Figures 2.10 and 2.11 graphically show the behavior of these equations and why, although at the beginning they adapt very well to reality, after a while they are completely distorted. A periodic variation is observed along the x and z axes while along the y axis the growth is unlimited.

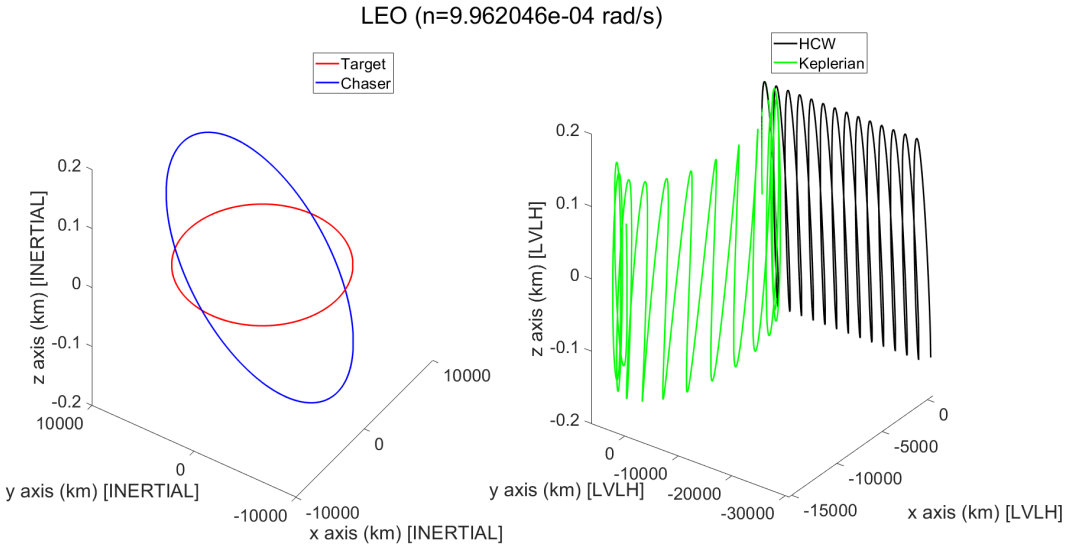

Figure 2.10 Comparison between the real solution and the one obtained using the HCW equations for two satellites in LEO whose orbits are shown in the left figure.

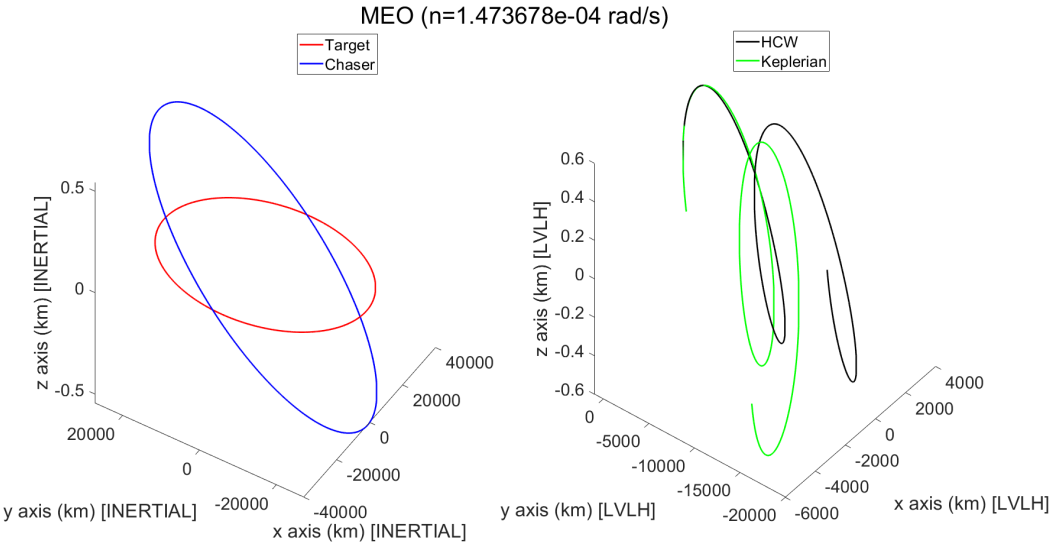

Figure 2.11 Comparison between the real solution and the one obtained using the HCW equations for two satellites in MEO whose orbits are shown in the left figure.

The simulation time was the same for both segments: 24 hours. However, as the average orbital speed n of the satellites in LEO is much higher, they separate much faster and this causes the equations to lose their validity more quickly, being a factor that must be taken into account.

Figure 2.12 shows the difference between the real orbit propagated with the nonlinear differential equation of motion (2.7) and the one propagated with HCW model (2.35) for an object that starts at 600 meters from the target propagated up to 15 kilometers. After approximately 150 seconds the discrepancy in position is only on the order of centimeters (Figure 2.13). It is rather small in comparison with the relative distances considered (kilometers).

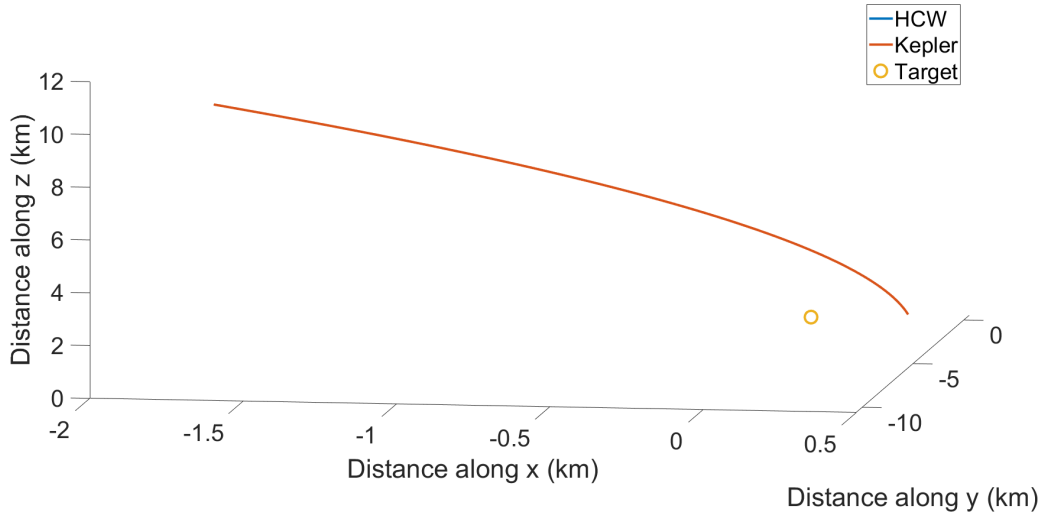

Figure 2.12 Orbital path of a near object propagated up to 15km of distance from the target.

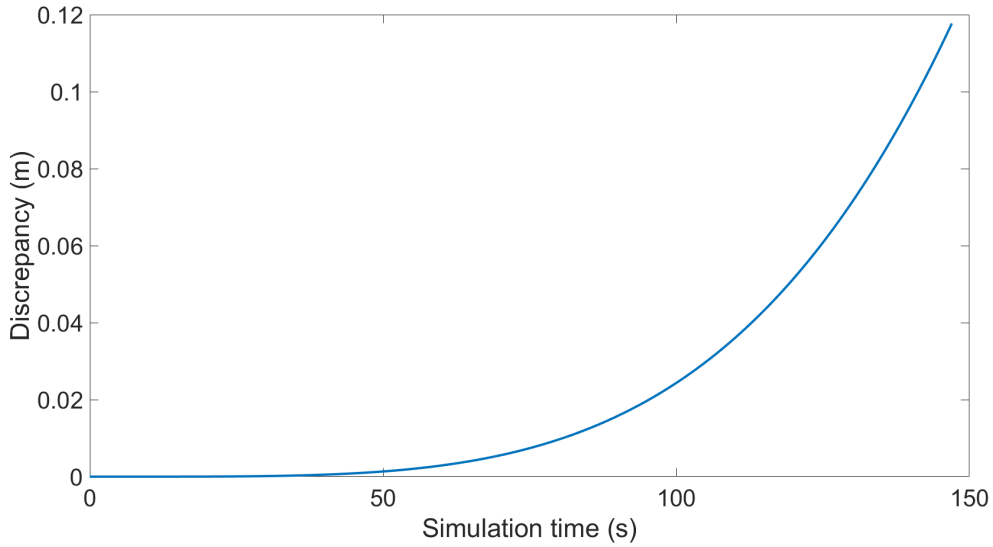

Figure 2.13 Error in distance between the propagated orbits up to 15km of distance from the target.

Subsequently, the orbit was propagated 9 times more, allowing the near object to reach a distance of 150km from the chaser (extremely big compared to the type of problem we will work with). Figure 2.14 shows the propagated orbit comparison and Figure 2.15 the discrepancy in position. Now we can clearly appreciate the discrepancy between the propagation using the nonlinear differential equation of motion and the HCW model. In this case, the error reaches high values of the order of hundreds of meters and therefore the use of HCW equations is not advisable to study the position of an object that gets too far away from a close initial position.

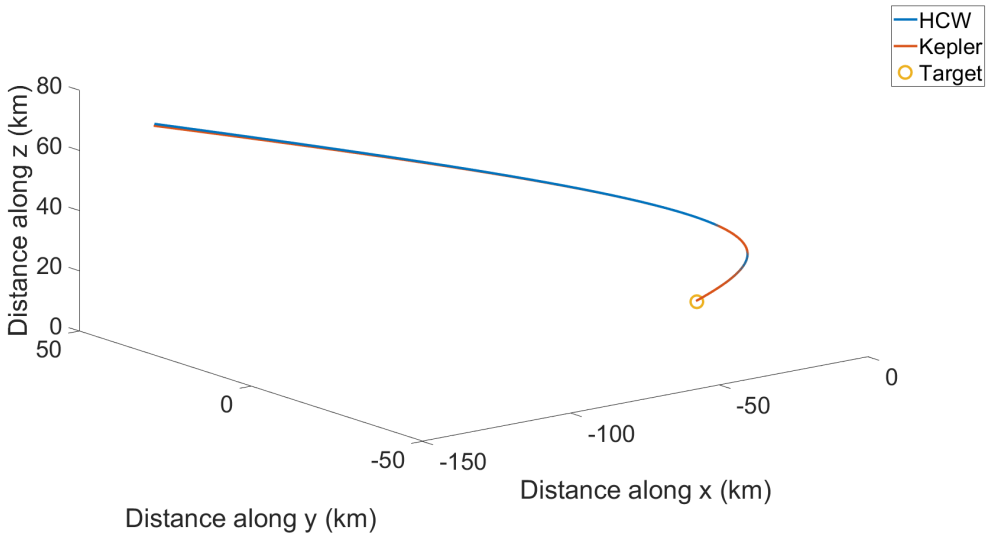

Figure 2.14 Orbital path of a near object propagated up to 150km of distance from the target.

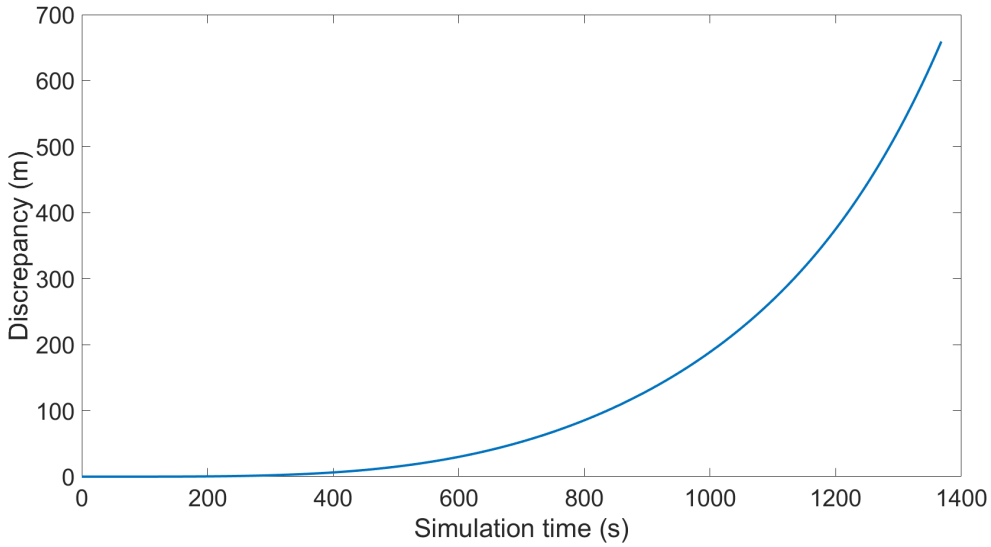

Figure 2.15 Error in distance between the propagated orbits up to 150km of distance from the target.

However, the position error could be mitigated if we consider resetting the initial conditions in the HCW equations as the objects move. Figure 2.16 shows the propagated orbit in the same conditions as the previous case but with a correction in position every 60 seconds.

This procedure does not preclude the increase of errors (especially when the objects get too far away), but we can mitigate them. The evolution of these errors is shown in Figure 2.17.

This last study, despite not being necessary at all for the problem that we are going to consider (objects starting very close), guarantees greater fidelity in the solution that we will obtain because we might apply this same concept (update the relative position of the object as it moves) at smaller distances and therefore reduce the error in distance. However, in practice, the relative state is often unknown, and therefore this idea is not useful in real applications.

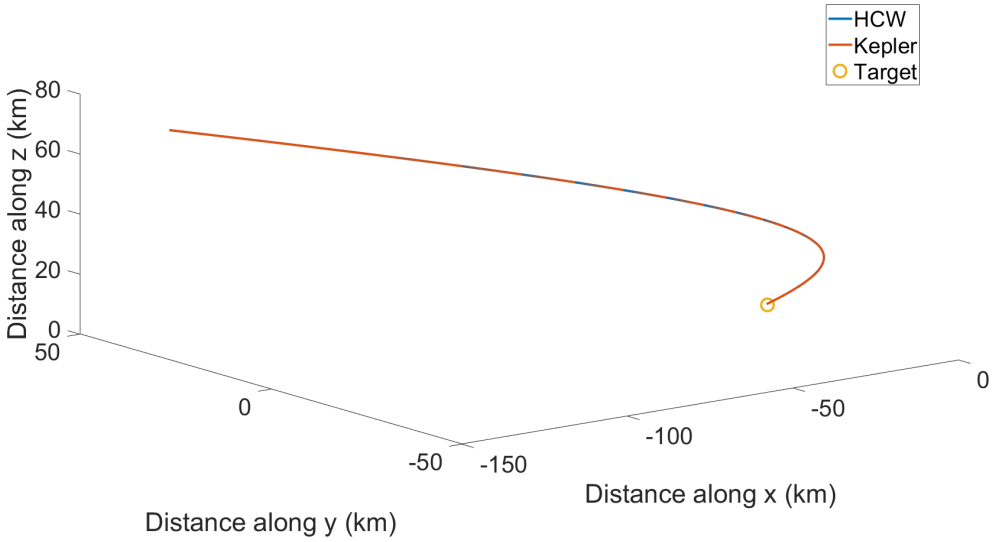

Figure 2.16 Orbital path of a near object propagated up to 150km of distance from the target with corrections each 60 seconds.

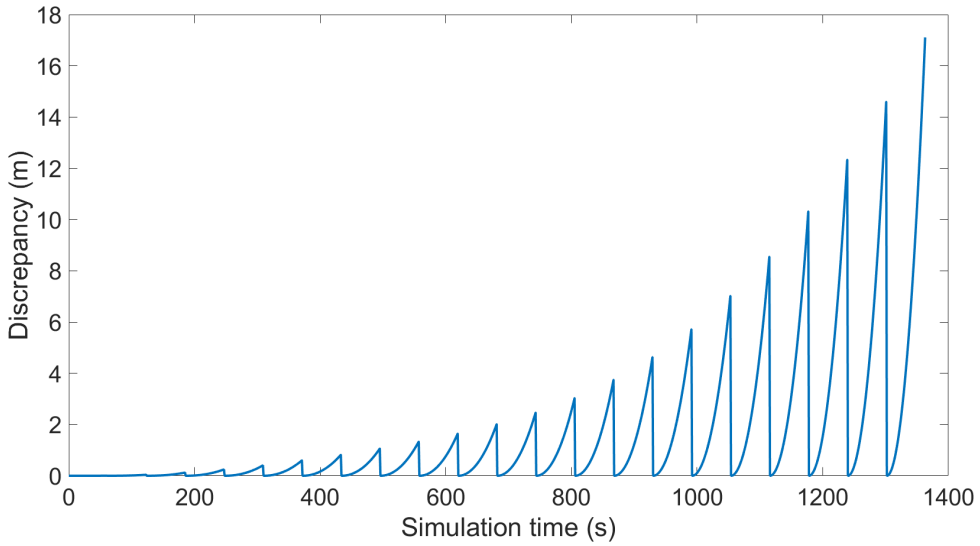

Figure 2.17 Error in distance between the propagated orbits up to 150km of distance from the target with corrections in position each 60 seconds.

Despite the apparent drawback of using the HCW equations, there are numerous reasons to consider their use:

- They have an analytic solution.
- They take smaller computation times (table 2.2).
- Linear dynamics allow the use of simpler techniques for instance for uncertainty propagation (see next chapter).
- They provide an accurate solution for small distances.

Table 2.2 Comparison of the times required to propagate the relative movement using the Keplerian propagation against HCW equations for different propagation times.

	5 minutes	10 minutes	30 minutes	60 minutes	90 minutes
Keplerian	0.0043 s	0.0064 s	0.0148 s	0.0278 s	0.0412 s
HCW	0.0035 s	0.0052 s	0.0139 s	0.0267 s	0.0391 s

3 Background material on statistics and random processes

3.1 Basics of statistics

In this section, the basic concepts of statistics that are used in this project are defined. The family of distributions used to model the errors as well as numerous properties that are used to simplify subsequent calculations will be introduced next.

3.1.1 Random Variables

A random variable is a function that converts values from the sample space S into values in the set $\mathbb{R}$ of all real numbers [15].

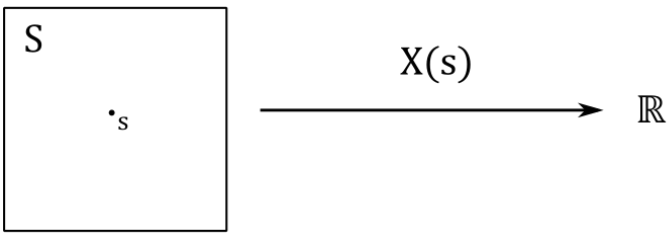

Figure 3.1 The random variable X as a function of the sample space S taking values in $\mathbb{R}$.

A random variable X is discrete if there is a finite or countable sequence $x_1, x_2, ...$ of distinct real numbers, and a corresponding sequence $p_1, p_2, ...$ of nonnegative real numbers, such that $P(X = x_i) = p_i$ for all i, and $\sum_i p_i = 1$. We name $P(X = x)$ as the probability mass function (pmf).

A random variable X is continuous if $P(X = x) = 0$ for all $x \in \mathbb{R}$. We define the probability density funtion (pdf) f so that $P(a \leq X \leq b) = \int_a^b f(x)\,dx$, whenever $a \leq b$. f is a valid density function if $f(x) \geq 0$ for all $x \in \mathbb{R}$, and $\int_{-\infty}^{\infty} f(x)\,dx = 1$. Hence, for a continuous distribution, we can say that $P(X = a) = 0$ for every a.

Given a random variable X, its cumulative distribution function (cdf) is the function $F_X : R^1 \rightarrow [0,1]$ defined by $F_X(x) = P(X \leq x)$

Let X be a discrete random variable with probability function p_X.
Then, its cumulative distribution function F_X satisfies:

$$F_X(x) = \sum_{x' \leq x} p_X(x')$$

Let X be an absolutely continuous random variable with density function f_X. Then, the cumulative distribution function F_X of X satisfies:

$$F_X(x) = \int_{-\infty}^{x} f_X(x')\,dx'$$

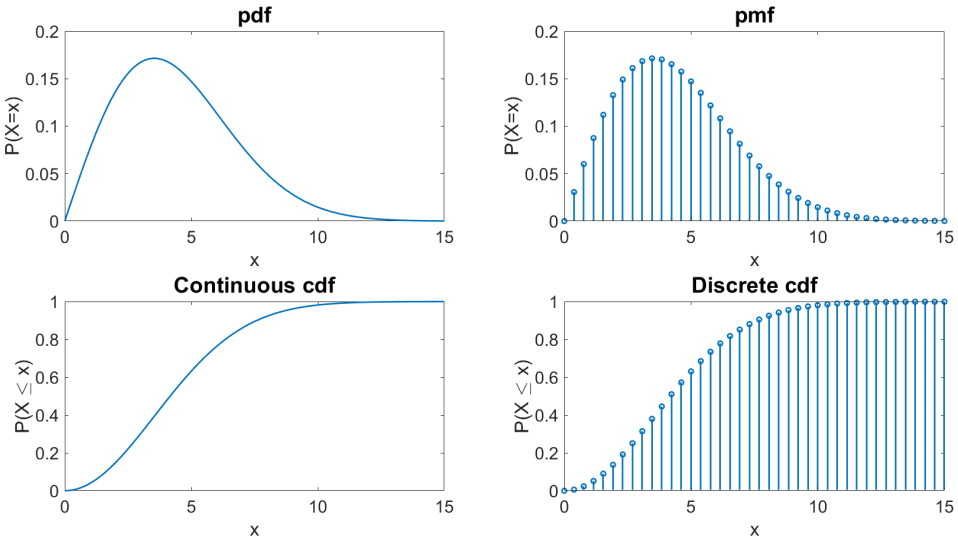

Figure 3.2 Representation of the probability density/mass function (pdf/pmf) and cumulative distribution function (cdf) for a discrete and a continuous random variable.

Two random variables X and Y are said to be independent if

$$P(X = x, Y = y) = P(X = x) \cdot P(Y = y), \qquad for\ all\ x,y \tag{3.1}$$

3.1.2 Expectation and variance

The expected value of a random variable X, denoted $E[X]$, is a weighted mean and is intuitively the arithmetic mean of a large number of independent realizations of X. The expected value is also known as the expectation, mean or first moment and denoted by μ_X

Let X be a discrete random variable, taking on distinct values $x_1, x_2 \ldots$ with $p_i = P(X = x_i)$. Then, the expected value of X is defined by

$$E[X] = \sum_i x_i \cdot p_i \tag{3.2}$$

Let X be an absolutely continuous random variable, with density function f_X. Then, the expected value of X is given by

$$E[X] = \int_{-\infty}^{\infty} x \cdot f_X(x)\,dx \tag{3.3}$$

The expectation has some properties:

- Let X and Y be random variables, and let a and b be real numbers. Then $E[a \cdot X + b \cdot Y] = a \cdot E[X] + b \cdot E[Y]$
- Let X and Y be random variables that are uncorrelated. Then $E[X \cdot Y] = E[X] \cdot E[Y]$

The expectation is a value that formalizes the idea of the mean value of a random phenomenon. However, this tells us nothing about the dispersion of its distribution. For that, we define the variance.

The variance of a random variable X is the average of the squared differences from the mean. It is defined by

$$\sigma_x^2 = Var(X) = E\left[(X - E[X])^2\right] = E\left[(X - \mu_X)^2\right] \tag{3.4}$$

The variance has some properties:

- If a and b are real numbers, then $Var(a \cdot X + b) = a^2 \cdot Var(X)$
- $Var(X) = E\left[X^2 - 2 \cdot X \cdot E[X] + E[X]^2\right] = E[X^2] - 2E[X]E[X] + E[X]^2 = E[X^2] - E[X]^2$

Note that the square in (3.4) implies that the "scale" of $Var(X)$ is the square of the scale of X. To correct this "scale" problem, we can simply take the square root. The standard deviation of a random variable X is the quantity

$$\sigma_x = Sd(X) = \sqrt{Var(X)} = \sqrt{E\left[(X - \mu_X)^2\right]} \tag{3.5}$$

Let X be any random variable, with standard deviation $Sd(X)$, and let a be any real number. Then $Sd(a \cdot X) = |a| \cdot Sd(X)$

Intuitively, the standard deviation σ is a measure of how spread out the distribution of X is, or how random X is, or how much X varies. This is clearly shown in Figure 3.3.

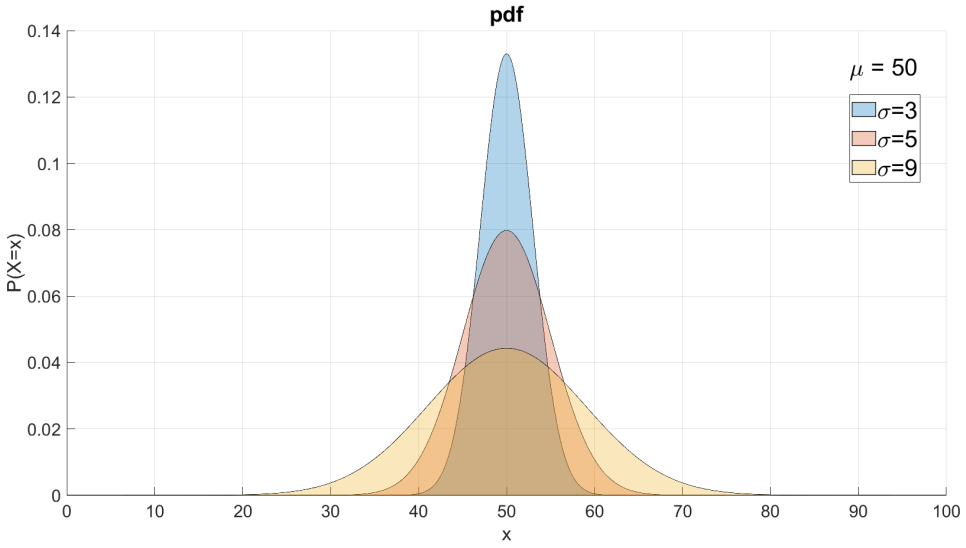

Figure 3.3 Different probability density functions with the same mean but with different standard deviations.

3.1.3 Covariance

The covariance indicates how the mean values of two variables move together. If the value of a random variable X increases whenever the variable Y does and the same relationship is found when each variable decreases, then the variables are said to have positive covariance.

The covariance of two random variables X and Y is given by

$$Cov(X,Y) = E\left[(X - E[X]) \cdot (Y - E[Y])\right] = E\left[(X - \mu_X) \cdot (Y - \mu_Y)\right] = \sigma_{xy} \tag{3.6}$$

The covariance can also be expressed as

$$Cov(X,Y) = E[X \cdot Y] - E[X] \cdot E[Y] \tag{3.7}$$

Note that $Cov(X,X) = E\left[(X - \mu_X) \cdot (X - \mu_X)\right] = E\left[(X - \mu_X)^2\right] = Var(X)$
If X and Y are uncorrelated, then $Cov(X,Y) = 0$ because in that case $E[X \cdot Y] = E[X] \cdot E[Y]$.

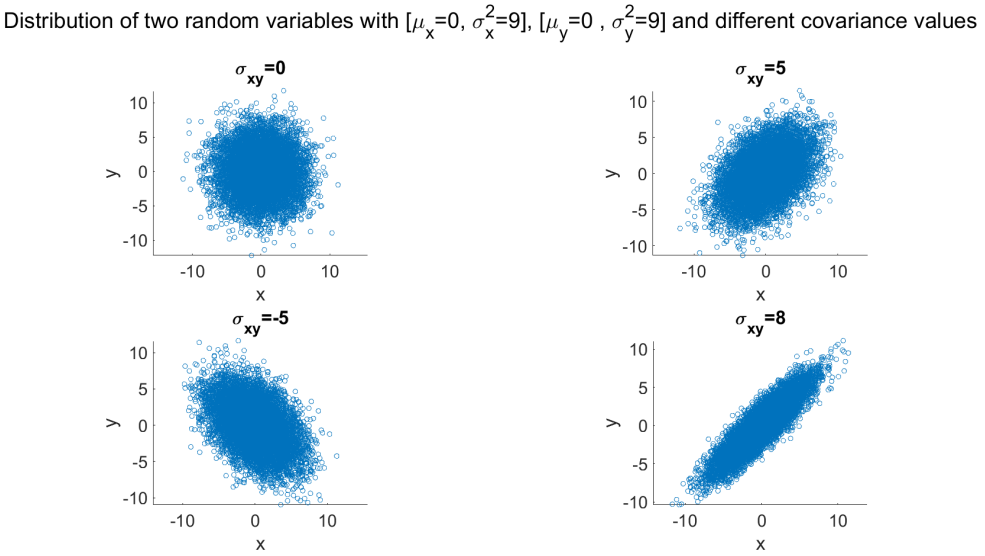

Figure 3.4 Distribution of two random variables around (0,0) with different covariance values.

To operate with the variance and covariance in an organized way, we define the covariance matrix for n random variables as a symmetric matrix of size $n \times n$ on whose diagonal there is the variance of each of the variables and outside the diagonal the covariance between the different variables.

For example, the covariance matrix of two random variables X and Y would be written as

$$\Sigma = \begin{bmatrix} Cov(X,X) & Cov(X,Y) \\ Cov(Y,X) & Cov(Y,Y) \end{bmatrix} = \begin{bmatrix} \sigma_x^2 & \sigma_{xy} \\ \sigma_{xy} & \sigma_y^2 \end{bmatrix} \tag{3.8}$$

3.1.4 Multivariate random variables

A multivariate random variable or random vector $\mathbf{X}$ is defined as a column vector $\mathbf{X} = (X_1,\ldots,X_n)^{\mathrm{T}}$ whose components are scalar-valued random variables of the same probability space.

The expected value or mean of a random vector $\mathbf{X}$ is a fixed vector $\mathrm{E}[\mathbf{X}]$ whose elements are the expected values of the respective random variables.

$$\mathrm{E}[\mathbf{X}] = (\mathrm{E}[X_1],\ldots,\mathrm{E}[X_n])^{\mathrm{T}} \tag{3.9}$$

The covariance matrix of an $n \times 1$ random vector is an $n \times n$ matrix whose $(i,j)^{th}$ element is the covariance between the i^{th} and the j^{th} random variables.

$$\Sigma_{\mathbf{X}} = \mathrm{Var}[\mathbf{X}] = \mathrm{E}[(\mathbf{X} - \mathrm{E}[\mathbf{X}])(\mathbf{X} - \mathrm{E}[\mathbf{X}])^T] = \mathrm{E}[\mathbf{X}\mathbf{X}^T] - \mathrm{E}[\mathbf{X}]\,\mathrm{E}[\mathbf{X}]^T \tag{3.10}$$

Two random vectors $\mathbf{X} = (X_1,\ldots,X_m)^T$ and $\mathbf{Y} = (Y_1,\ldots,Y_n)^T$ are called uncorrelated if

$$\mathrm{E}[\mathbf{X}\mathbf{Y}^T] = \mathrm{E}[\mathbf{X}]\,\mathrm{E}[\mathbf{Y}]^T \tag{3.11}$$

Let $\mathbf{X} = (X_1, \cdots, X_n)^T$ and $\mathbf{Y} = (Y_1, \cdots, Y_n)^T$ be two n-random vectors uncorrelated of the same probability space (representing the same magnitude each element). Each of the random vectors has an associated covariance matrix $\Sigma_{\mathbf{X}}$ and $\Sigma_{\mathbf{Y}}$.

Let $\mathbf{Z} = \mathbf{X} + \mathbf{Y} = (X_1 + Y_1, \cdots, X_n + Y_n)^T$ be a random vector that sums both magnitudes. Then, if we want to compute the covariance of the combination of both random vectors:

$$\Sigma_{\mathbf{Z}} = \begin{bmatrix} Cov(Z_1,Z_1) & Cov(Z_1,Z_2) & \dots & Cov(Z_1,Z_n) \\ Cov(Z_2,Z_1) & Cov(Z_2,Z_2) & & \\ \vdots & & \ddots & \\ Cov(Z_n,Z_1) & & & Cov(Z_n,Z_n) \end{bmatrix} \tag{3.12}$$

Where, if $\mathbf{X}$ and $\mathbf{Y}$ are uncorrelated:

$$\begin{aligned} Cov(Z_k,Z_k) = Cov(X_k + Y_k, X_k + Y_k) &= Cov(X_k,X_k) + Cov(Y_k,Y_k) + Cov(X_k,Y_k) + Cov(Y_k,X_k) = \\ &= Cov(X_k,X_k) + Cov(Y_k,Y_k) = \Sigma_{X_k} + \Sigma_{Y_k} \end{aligned} \tag{3.13}$$

$$\begin{aligned} Cov(Z_i,Z_j) = Cov(X_i + Y_i, X_j + Y_j) &= Cov(X_i,X_j) + Cov(Y_i,Y_j) + Cov(X_j,Y_i) + Cov(Y_j,X_i) = \\ &= Cov(X_i,X_j) + Cov(Y_i,Y_j) = \Sigma_{X_{ij}} + \Sigma_{Y_{ij}} \end{aligned} \tag{3.14}$$

Which leads to the result:

$$\Sigma_{\mathbf{Z}} = \Sigma_{\mathbf{X}} + \Sigma_{\mathbf{Y}} \tag{3.15}$$

Note that (3.15) is valid only if $\mathbf{X}$ and $\mathbf{Y}$, besides being uncorrelated, are expressed in the same frame and units.

3.2 Gaussian or Normal distribution

The Gaussian or normal distribution is a type of continuous probability distribution fully characterized by its mean and standard deviation. This makes the distribution symmetric and it is depicted as a bell-shaped curve when plotted.

The probability density function of a random variable X of mean μ and variance σ^2 that follows a normal distribution $X \sim N\left(\mu, \sigma^2\right)$ is given by:

$$f(x) = \frac{1}{\sigma \cdot \sqrt{2\pi}} \exp\left[-\frac{(x-\mu)^2}{2 * \sigma^2}\right] \tag{3.16}$$

Note that changes in μ simply shift the density without changing its shape whereas the value of σ^2 controls the amount of spread.

The confidence interval of a given statistical distribution is defined as the range of values, bounded above and below the expected value, that likely would contain an unknown sample. Confidence level refers to the percentage of probability, or certainty, that the confidence interval would contain the true sample when a random sample is drawn many times.

In a normal distribution, approximately 68% of the data collected will fall within +/- one standard deviation of the mean; approximately 95% within +/- two standard deviations; and 99.7% within three standard deviations (Figure 3.5).

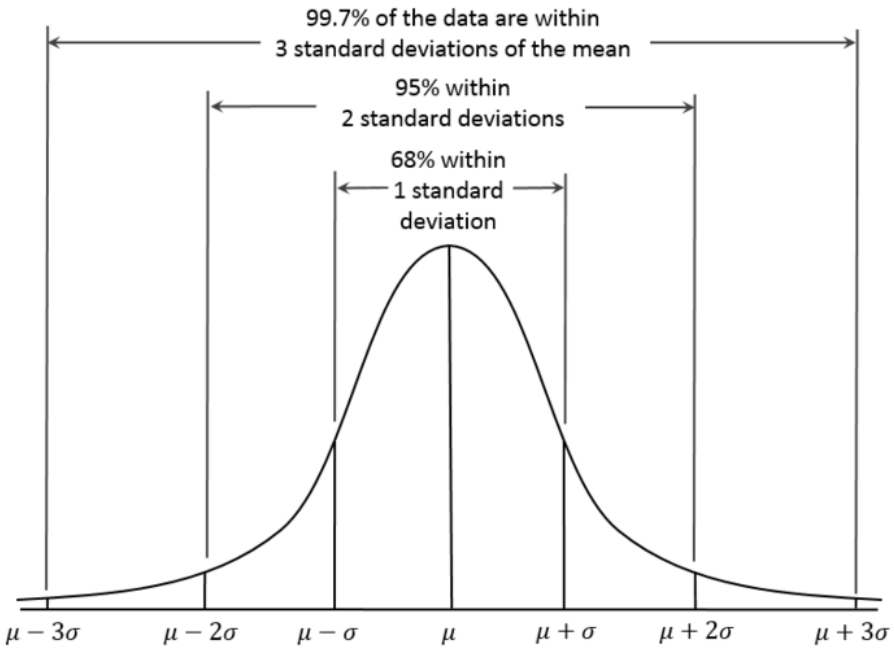

Figure 3.5 Confidence intervals of a normal distribution.

Multivariate normal distribution

A multivariate normal distribution, also called a multivariate Gaussian distribution, is a generalization of the one-dimensional normal distribution to higher dimensions.

The multivariate normal distribution of a n-dimensional random vector $\mathbf{X} = (X_1, \cdots, X_n)^T$ can be written in the following notation:

$$\mathbf{X} \sim \mathcal{N}(\boldsymbol{\mu}, \Sigma)$$

Where $\boldsymbol{\mu}$ is its mean vector $\boldsymbol{\mu} \in \mathbb{R}^n$ and Σ its covariance matrix $\Sigma \in \mathbb{R}^{n \times n}$.

Its density function is given by

$$f(\mathbf{x}) = \frac{1}{\sqrt{(2\pi)^n |\Sigma|}} \exp\left(-\frac{1}{2}(\mathbf{x} - \boldsymbol{\mu})^T \Sigma^{-1} (\mathbf{x} - \boldsymbol{\mu})\right) \tag{3.17}$$

Equation (3.17) can only be used if the multivariate normal distribution is said to be "non-degenerate", that is, when the symmetric covariance matrix Σ is positive definite.

Note that for $n = 1$ the equation reduces to that of the univariate normal distribution (3.16).

The confidence region is the multi-dimensional generalization of the confidence interval. For the three-dimensional multivariate normal distribution, this region is an ellipsoid centered on the mean. The equation of the ellipsoid is given by

$$(\mathbf{x} - \boldsymbol{\mu})^T \cdot \Sigma^{-1} \cdot (\mathbf{x} - \boldsymbol{\mu}) = d^2 \tag{3.18}$$

Where d is a parameter called *Mahalanobis distance* and it depends on the dimension of the distribution. The greater the Mahalanobis distance is taken, the greater the confidence ellipsoid and the greater the certainty that the sample is within the confidence region. The relation between the Mahalanobis distance, the dimension, and the certainty can be obtained from the *Generalized regularized incomplete gamma function* [16] and can be seen in Figure 3.6.

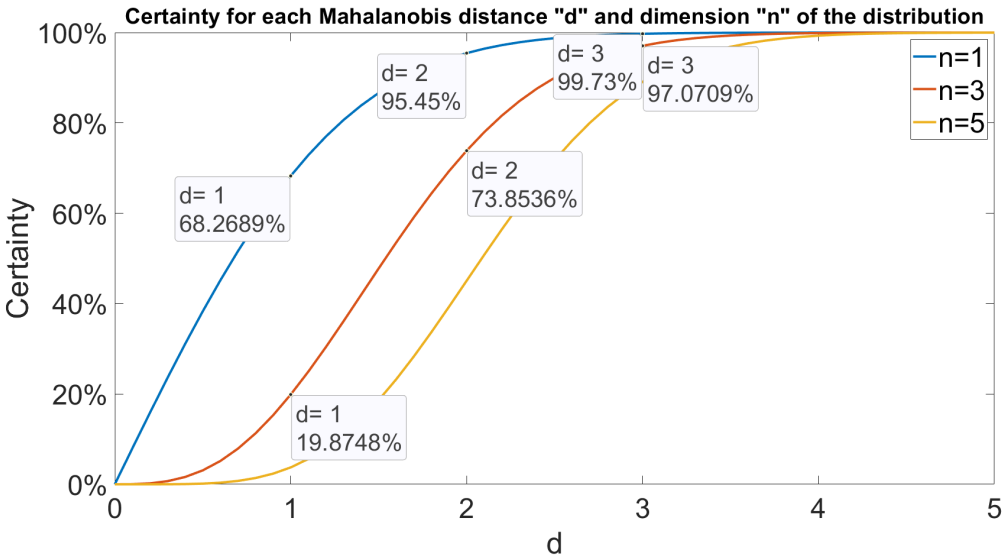

Figure 3.6 Certainty of the confidence region for each Mahalanobis distance "d" taken and for each dimension "n" of the distribution.

Note that the relationship is perfectly fulfilled for the one-dimensional case (Figure 3.5) and that for the three-dimensional case, $d = 3$ guarantees us the certainty of 97,07%.

The directions of the principal axes of the ellipsoid are given by the eigenvectors of the covariance matrix Σ. The semiaxis lengths are given by $d \cdot \sqrt{\lambda_i}$, where λ_i is the eigenvalue associated to the eigenvector e_i.

If the covariance matrix is not diagonal, the ellipsoid's eigenvectors are not aligned with the axes of the frame as can be seen in Figure 3.7

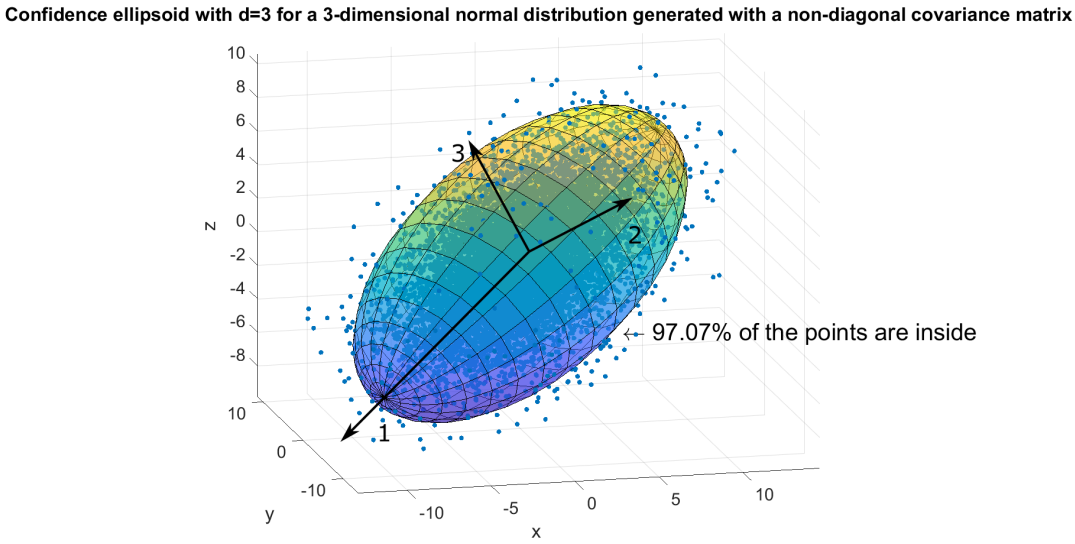

Figure 3.7 Confidence region for a multivariate distribution generated with a non-diagonal covariance matrix.

3.2.1 The Central Limit Theorem

In probability theory, the central limit theorem establishes that, in many situations, when independent and identically distributed (i.i.d.) random variables are added, their properly normalized

sum tends toward a normal distribution even if the original variables themselves are not normally distributed [17].

The theorem is a key concept in probability theory because it implies that probabilistic and statistical methods that work for normal distributions can be applied to many problems involving other types of distributions.

Thereafter, if one assumes that the noise of a measure is the result of several independent causes which randomly affect the observations, the Central Limit Theorem states that the distribution of these error causes, if they are numerous enough, will tend to be normal.

In our case study, we want to know the position of a satellite subject to measurement errors due to the noise previously mentioned. If we apply the Central Limit Theorem, we can assume that the position of the satellite, determined in 3D, can be estimated with a normal distribution function in each of the main axes of the satellite, which as a whole gives us a multivariate distribution that geometrically provides us with a confidence ellipsoid centered on the main axes considered.

3.3 Monte Carlo method

The Monte Carlo method is a sample-based procedure to obtain solutions of stochastic problems. It consists in generating a large number of points that follow a certain statistical distribution to obtain an approximate solution to a problem that could not be easily solved analytically. It allows turning an abstract idea into something manageable such as random points. It can be used for example to obtain the value of the number pi [18] (Figure 3.8) or to solve a stochastic differential equation.

The reliability of this method lies in the *Law of Large Numbers*. According to the law, the average of the results obtained from a large number of trials should be close to the expected value and will tend to become closer to the expected value as more trials are performed.

To guarantee that the solution to the statistical methods that we are going to develop is correct, we are going to use a Monte Carlo simulation to verify the result. The power of this method is that no assumptions or mathematical transformations/simplification must be done to get a solution because the points are simply counted by brute force. Thus, as far as the inputs are precise and the algorithm is correct, the Monte Carlo simulation should yield the "true" result if the number of points generated is large enough.

However, using this method is a double-edged sword: To obtain the most accurate result possible, it is necessary to generate as many points as possible. This has a direct impact on computing time, multiplying several orders of magnitude the time it would take to solve the same problem directly.

In addition to the calculation time, there is the inaccuracy of the solution. When a continuous function is integrated, all the domain of integration is taken into account and an exact result is obtained. However, if the domain is made of discrete points, the integration is not exact. If an infinite number of points were generated the error would be reduced to 0, but that is not physically possible and therefore a completely exact result can never be obtained.

For these reasons, this method is only used to validate a solution and not to obtain a result.

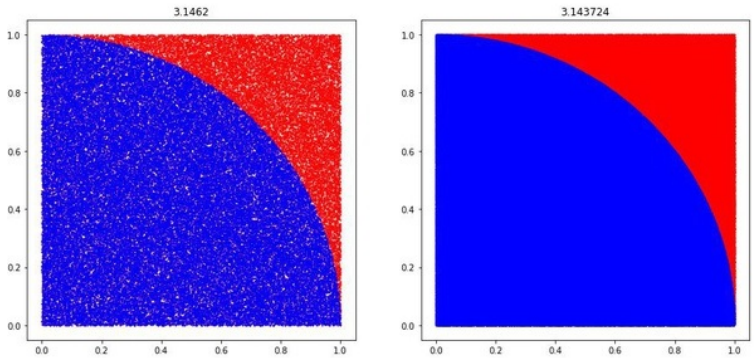

Figure 3.8 Estimation of π using Monte Carlo. As the number of points increase, the result becomes more accurate.

It is worth mentioning a technique called *importance sampling*. The idea behind importance sampling is that certain values of the input random variables in a simulation have more impact on the parameter being estimated than others. If these important values are emphasized by sampling them more frequently, the solution can be further refined without requiring much more computation. Hence, the basic methodology in importance sampling is to modify the distribution to encourage the important values. This use of biased distributions will result in a biased result if it is applied directly in the simulation. However, the simulation outputs are then weighted to correct for the biased distribution, which ensures that the new importance sampling result is unbiased [19].

3.4 Stochastic processes and differential equations

A **stochastic process** or stochastic variable is nothing but a random variable or vector $\mathbf{X}(t)$ that changes with time. Therefore, its mean and covariance also vary with time: $\mathbf{m}(t), \Sigma(t)$.

For a stochastic process, the autocorrelation is defined as $R(t,\tau) = E\left[\mathbf{X}(t)\cdot\mathbf{X}(\tau)^T\right]$. The autocorrelation allows to know to what extent the past history of $\mathbf{X}(t)$ influences its current value.

A *Gaussian process* is a stochastic process that verifies $\mathbf{X}(t) \sim \mathcal{N}\left(\mathbf{m}(t), \Sigma(t)\right)$, that is, it is distributed as a multivariate normal whose mean and covariance vary with time.

A *white noise* is a stochastic process characterized by the fact that its process values at two different times are not statistically correlated and its mean is zero. Hence, a white noise $\boldsymbol{\nu}$ verifies:

- $E\left[\boldsymbol{\nu}(t)\right] = 0$
- $E\left[\boldsymbol{\nu}(t)\cdot\boldsymbol{\nu}(\tau)^T\right] = \sigma_\nu^2$
- $R(t,\tau) = E\left[\boldsymbol{\nu}(t)\cdot\boldsymbol{\nu}(t)^T\right] = \delta(t-\tau)\sigma_\nu^2$

A *Gaussian white noise* is a Gaussian process that verifies the conditions of white noise [20].
The *bias* $\mathbf{b}$ of a measure is a constant offset from the true value that should be measured.

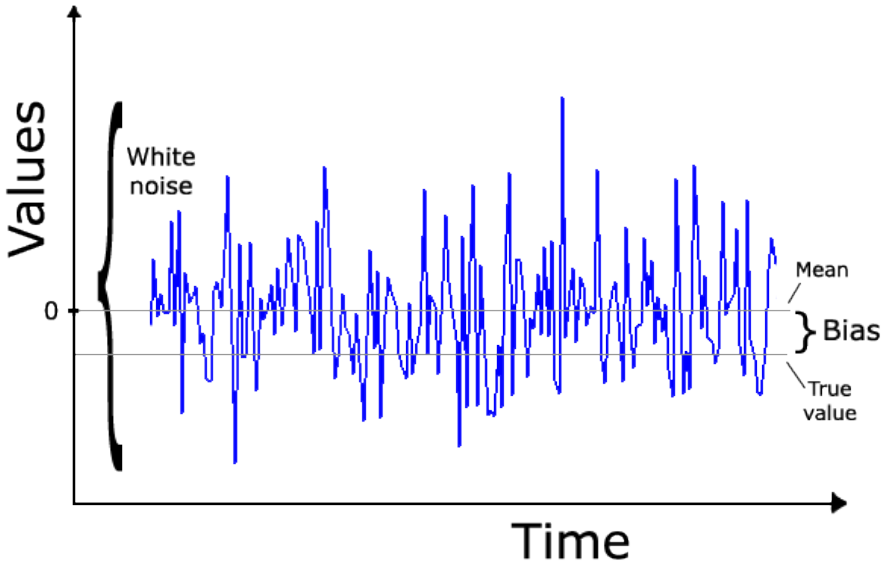

Figure 3.9 White noise and bias.

The time evolution of a stochastic variable $\mathbf{X}(t)$ in the presence of noise $\boldsymbol{\epsilon}(t)$ is given by the following stochastic differential equation:

$$\dot{\mathbf{x}}(t) = A(t)\mathbf{x}(t) + \boldsymbol{\epsilon}(t) \tag{3.19}$$

Where A is the matrix that contains the coefficients that build the differential equation for the propagation without noise (2.35).

A good model for sources of error (measurement errors, gravitational errors) is $\boldsymbol{\epsilon}(t) = \mathbf{b} + D\boldsymbol{\nu}$, where $\boldsymbol{\nu}$ is the Gaussian white noise and $\mathbf{b}$ the bias. The following hypotheses are made:

- $\boldsymbol{\nu}$ is the Gaussian white noise with variance σ_ν^2.
- Initially, $\mathbf{x}(t_0) \sim \mathcal{N}\left(\mathbf{m_0}, \Sigma_0\right)$. If the initial value was known without error, $\Sigma_0 = 0$.
- $\boldsymbol{\nu}$ and $\mathbf{x}(t_0)$ are independent.

Under these conditions, we have that $\mathbf{x}(\mathbf{t})$ is a Gaussian process, that is, $\mathbf{x}(t) \sim \mathcal{N}\left(\mathbf{m}(t), \mathbf{\Sigma}(t)\right)$, and its mean and covariance verify the following evolution:

$$\begin{cases} \dot{\mathbf{m}}(t) = A(t)\mathbf{m}(t) + \mathbf{b} \\ \mathbf{m}(0) = \mathbf{m}_0 \end{cases} \tag{3.20}$$

$$\begin{cases} \dot{\Sigma}(t) = A(t)\Sigma(t) + \Sigma(t)A^T(t) + \sigma_\nu^2 DD^T \\ \Sigma(0) = \Sigma_0 \end{cases} \tag{3.21}$$

4 Selection, implementation and validation of a collision risk assessment method

4.1 Introduction

Estimating the risk of collision between two orbiting bodies has been an important problem for many years already. In the last three decades numerous authors have developed their own methodology to compute the probability of collision for a given data set.

The early ideas of spacecraft collision were based on a *Poisson distribution* and tried to emulate the problem by applying concepts of the *kinetic theory of gases* in which the molecules were statistically uniformly distributed and moved in straight lines [21].

Current formulations are more realistic but still based on that concept. Space object collision probability analysis is typically conducted with the objects modeled as spheres to eliminate the need for attitude information. In addition, due to the relative velocity of the objects, their relative motion is often considered nearly linear during the encounter.

Starting from the *Central Limit Theorem* already introduced previously, the positional errors are assumed to be zero-mean, Gaussian, uncorrelated, and constant during the encounter due to its short duration.

As the covariance matrices associated to the error in position for both target and chaser are expected to be uncorrelated, they are simply summed to form one large combined confidence ellipsoid that is centered at the primary object (target) (3.15). In addition, both volumes are added forming what is called the *combined hardbody*, and it is placed in the position of the secondary object (chaser). The secondary object then passes quickly through this combined ellipsoid creating a tube-shaped path that is commonly called a *collision tube*. The probability of collision is obtained by evaluating the integral of the three-dimensional pdf (3.17) within the collision tube (Figure 4.1)

$$PR_T = \iiint_V \frac{1}{\sqrt{(2\pi)^n |\Sigma|}} \exp\left(-\frac{1}{2}(\mathbf{x}-\boldsymbol{\mu})^T \Sigma^{-1} (\mathbf{x}-\boldsymbol{\mu})\right) dx\, dy\, dz \tag{4.1}$$

The encounter region is defined when the second object is within d standard deviations $(d-\sigma)$ of the confidence ellipsoid. The Mahalanobis distance d is typically in the range of 3 to 8 to accommodate conjunction possibilities ranging from 97.070911% to 99.999999% (see Figure 3.6).

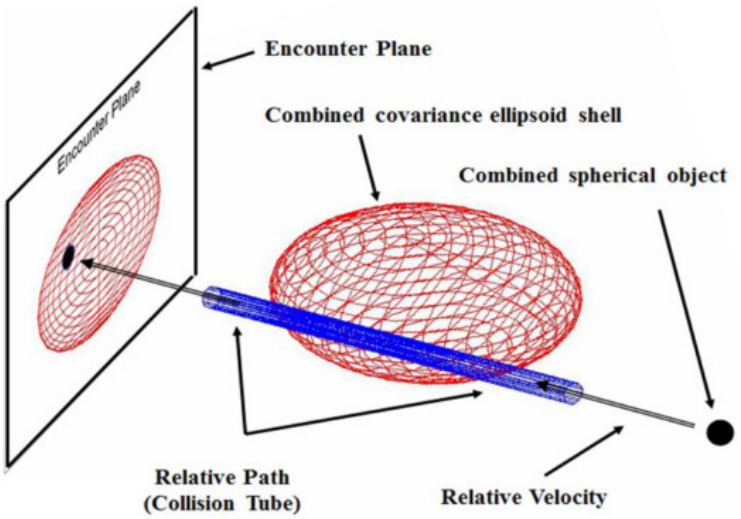

Figure 4.1 Collision probability computed as the integral of the three-dimensional pdf within the collision tube (taken from [4]).

Those are the basis of the modern collision formulations. However, each method takes a different way to compute the integral and that has a direct impact on the solution. The two most important factors are the veracity of said solution and its computation time. Those factors, along with the others less obvious, constitute the advantages and disadvantages of using one method or another.

There are four main categories in broad general terms and in chronological order to classify the current models. These are the Foster (1992), Chan (1997), Patera (2001 & 2005), and Alfano (2005) models.

It is also possible to use a Monte Carlo method, sampling random points of the error ellipsoid and computing the corresponding collision probability by counting the points withing the collision tube.

Foster's method

The method developed by Foster for NASA evaluates the collision probability numerically by examining the plane perpendicular to relative motion and dividing the combined object's circular cross-section into concentric circles and radial straight lines.

Chan's method

The model developed by Chan is analytical, being based on transforming the two-dimensional Gaussian probability density function (pdf) to a one-dimensional *Rician* pdf and using the concept of equivalent areas. This model involves the evaluation of an analytical expression containing two exponential terms.

Patera's method

Patera's model is based on a transformation of the formulation into a one-dimensional pdf and is formulated in the form of a "line-integral." Its evaluation is performed numerically by taking short line segments around a closed contour.

Alfano's method

Alfano's model is also based on a one-dimensional pdf expressed as two error functions and one exponential term. It is numerically evaluated using well-known software already developed for error functions.

Alfano performed a comparison between these four methods in 2007 [22]. Based on the number of function evaluations, which is a good indicator of computing efficiency, the Foster model is approximately ten or twenty times slower than either the Alfano or Patera model, which in turn are orders of magnitude slower than the Chan model. Chan's method is by far the fastest but is also the most restrictive due to relative object size limitations.

Because Patera's and Alfano's methods are sufficiently efficient and do not present restrictions regarding the shape and size of the bodies, they are the methods considered to deepen and study the probability of collision. However, Patera's method was the method of choice to develop and base the rest of the project around because it is more intuitive than Alfano's method and performs the integration continuously whereas Alfano performs it by a n-series expansion.

4.1.1 Short-term and Long-term encounters

We have just defined what is called an encounter. However, the encounter between two objects can be of two types.

First, think about a satellite that has an encounter with another one that follows a more eccentric orbit. They will pass close to each other but with a large difference in velocity. Then, we say that they will have a *short-term encounter* because the time in which the risk of collision is high enough to be considered is extremely tiny compared to the satellite's period. As a consequence, the chaser satellite will be a small fraction of time inside the combined ellipsoid centered at the target satellite.

It is clear that if the encounter is short enough, velocity and position error ellipsoids can be considered constant throughout it. Then, a very powerful and successful simplification can be made which greatly reduces computational time: the error ellipsoid volume swept by the hardbody is nothing but a straight tube with cross-section the shape of the combined hardbody projected in a plane perpendicular to the relative velocity direction (defined as encounter plane).

This type of encounter is also called to be in linear motion because the chaser is supposed to move along a straight line.

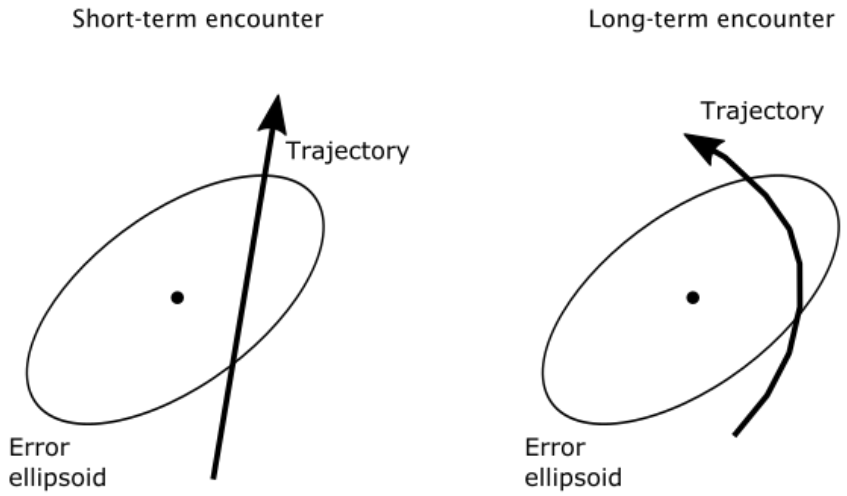

(a) Short-term encounter (Linear). **(b)** Long-term encounter (Non-linear).

Figure 4.2 Different encounters.

Unlike what happens in the linear motion case, there is the case of two satellites orbiting in similar orbital planes with a similar eccentricity.

In that case, we can no longer apply the assumption of linear movement, and therefore we must consider the evolution of the combined error ellipsoid and a certain curvature of the chaser's path relative to the target since the time in which there is risk is large enough.

This situation is the most frequent between GEO satellites and its study encompasses the linear motion because it is a particular case of non-linear motion considering null curvature. However, despite its apparent difficulty, the study of this case is not more complicated than the linear case. It is simply necessary to spend more time on the evolution of the parameters and assume that the solution will not be as accurate as in the linear case.

4.2 Patera's Method

Patera's method is an optimal method that allows us to study the probability of collision in a long-term encounter. Hence, it can be used too in the short-term encounter case.

4.2.1 Preliminary considerations

First of all, we must define the problem, make assumptions, and state which values are required.

Obviously, the main information that we need to know is the dynamics of the bodies. Different models of dynamics will be used: classical Keplerian propagation & HCW model. The propagation model to choose depends on the problem statement and, as demonstrated in the previous chapter, using one propagator or another does not affect the result as the considered distances are relatively small.

Once we have chosen the propagation model, another important piece of information is the uncertainty of the position of the satellites. As mentioned before, this uncertainty is modeled with the position error covariance matrix given by a multivariate Gaussian distribution with a mean equal to zero at each object's position. The correlation between both uncertainty matrix is assumed to be zero as the satellites are not supposed to affect each other during the encounter.

In addition, another assumption of these uncertainty matrices is that they will evolve and rotate as the satellite travels on its orbit but they will always keep a diagonal form in the body-fixed reference frame. It should be noted that this is not an essential requirement to develop the method since it is possible to work with time-varying covariance matrices (as will be discussed in the next chapter), but it is an essential simplification to obtain a simple analytical solution.

The last required information is the shape of the satellites. This method is powerful enough to be able to compute the probability of collision between satellites taking into account their shape [23]. However, as this is not an essential requirement for us and it will depend on each particular problem, the bodies will be assumed spherical with a radius equal to the largest distance possible from the center of mass to a point of its surface. In addition, thanks to this assumption, no attitude information is required and the computational effort is reduced.

As a result, the previously called combined hardbody is nothing but a sphere with a radius equal to the sum of both satellites' radii.

4.2.2 The Method: Transformations

The first step to reach an analytical solution is to put the problem in a suitable form that reduces the complexity of the integral [24].

The first task is to define the confidence ellipsoid given by the positional covariance matrix for each satellite. As we said, the covariance matrix of each satellite is assumed to be in a diagonal form at its local frame of reference (LVLH):

$$\Sigma_1 = \begin{bmatrix} \sigma_{11}^2 & 0 & 0 \\ 0 & \sigma_{12}^2 & 0 \\ 0 & 0 & \sigma_{13}^2 \end{bmatrix} \tag{4.2}$$

$$\Sigma_2 = \begin{bmatrix} \sigma_{21}^2 & 0 & 0 \\ 0 & \sigma_{22}^2 & 0 \\ 0 & 0 & \sigma_{23}^2 \end{bmatrix} \tag{4.3}$$

Where (5.1) and (5.2) are the covariance matrix of the target and chaser respectively.

We start by putting the matrices in the same reference frame: the inertial frame.

$$\Sigma_{1I} = R_1 \Sigma_1 R_1^T \tag{4.4}$$

$$\Sigma_{2I} = R_2 \Sigma_2 R_2^T \tag{4.5}$$

Where R is the matrix that performs the rotation from the local frame to the inertial frame defined as

$$R = \left[\begin{array}{c:c:c} \vec{i} & \vec{j} & \vec{k} \end{array} \right] \tag{4.6}$$

With $\vec{i}$, $\vec{j}$ and $\vec{k}$ being the column vectors defined by (2.29), (2.31) and (2.30) respectively.

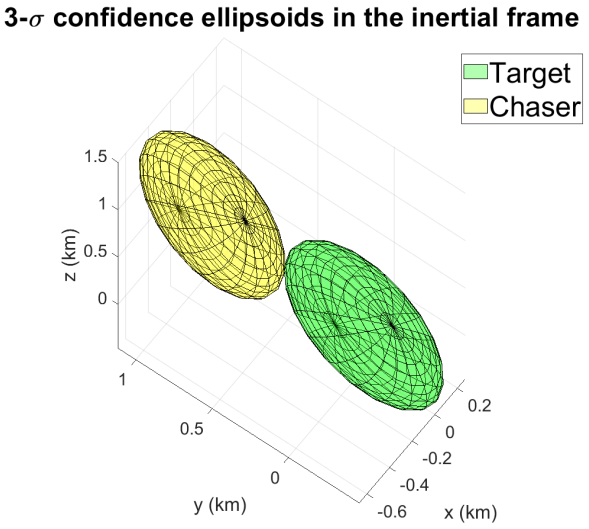

Figure 4.3 Confidence ellipsoid of each satellite in the inertial frame.

Next, as the covariance matrices are in the same reference frame and are uncorrelated, they can be summed (3.15):

$$\Sigma_T = \Sigma_{1I} + \Sigma_{2I} \tag{4.7}$$

Geometrically it would be as if instead of having two error ellipsoids centered on two different objects (Figure 4.3) we had a larger one, with greater uncertainty, centered at the target while the chaser could be considered without uncertainty.

Now, we are interested in doing the same with the spheres of each satellite. As they are spheres they can be easily summed into a big one with a radius equal to the sum of the radii. That combined body will be named the combined hardbody, and it is placed at the chaser (Figure 4.4).

A first step to get rid of the non-diagonal covariance matrix is to align our reference frame with the new combined confidence ellipsoid. In order to do that, we diagonalize the covariance matrix:

$$\Sigma_{T_d} = P\Sigma_T P^T = \begin{bmatrix} \sigma_1^2 & 0 & 0 \\ 0 & \sigma_2^2 & 0 \\ 0 & 0 & \sigma_3^2 \end{bmatrix} \tag{4.8}$$

Where P^T is the matrix that contains the eigenvectors of Σ_T. This frame in which the ellipsoid is aligned with the axis is called the **principal frame**.

The relative distance and velocity are rotated to this frame:

$$X = r_2 - r_1 \tag{4.9}$$
$$V = v_2 - v_1 \tag{4.10}$$

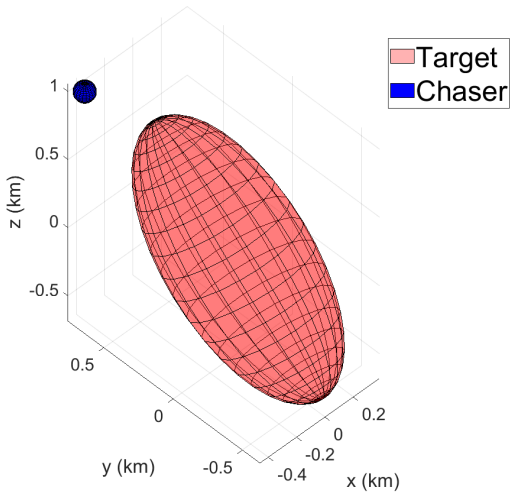

Figure 4.4 Combined ellipsoid placed at the target and combined hardbody placed at the chaser.

$$X_P = PX \tag{4.11}$$
$$V_P = PV \tag{4.12}$$

And in this way, we obtain a diagonal covariance matrix in the new reference frame (Figure 4.5).

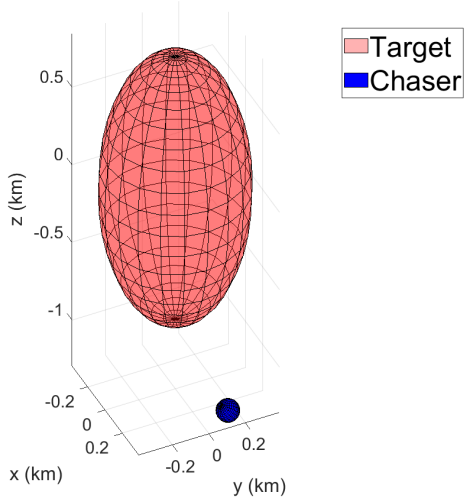

Figure 4.5 Geometries in the principal frame.

Then, another step is to transform the error ellipsoid into a sphere. This means a deformation of the principal frame and the whole space (Figure 4.6), but it will greatly improve the computational time as we will be able to reduce the covariance matrix into a *one-dimensional* variance.

$$\Sigma_{T_S} = S\Sigma_{T_d}S^T = \begin{bmatrix} \sigma_1^2 & 0 & 0 \\ 0 & \sigma_1^2 & 0 \\ 0 & 0 & \sigma_1^2 \end{bmatrix} \tag{4.13}$$

With S defined as

$$S = \begin{bmatrix} 1 & 0 & 0 \\ 0 & \frac{\sigma_1}{\sigma 2} & 0 \\ 0 & 0 & \frac{\sigma_1}{\sigma 3} \end{bmatrix} \tag{4.14}$$

This new frame is called the **scaled frame** and the new relative distance and velocity is

$$X_S = SPX \tag{4.15}$$
$$V_S = SPV \tag{4.16}$$

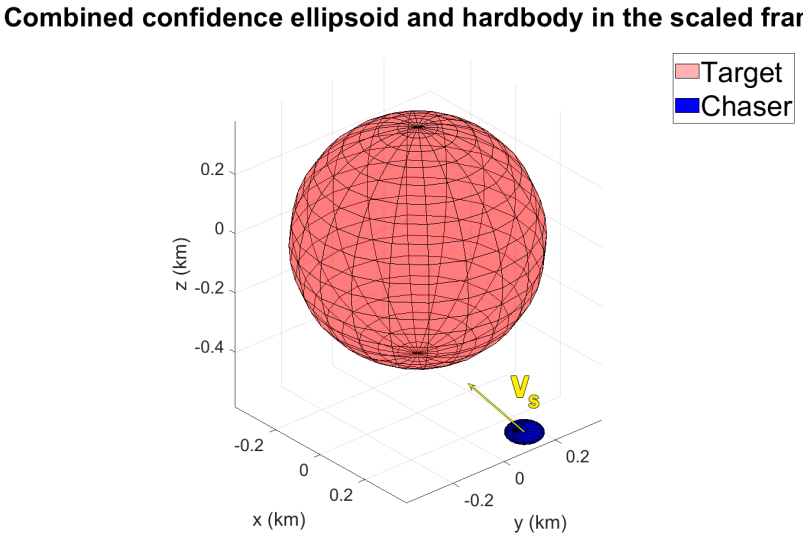

Figure 4.6 Geometries in the scaled frame.

Finally, we put the bodies into the **encounter** frame, a frame defined as:

- z-axis: Parallel to the relative velocity of the chaser from the target in the scaled frame.
- y-axis: Perpendicular to the plane of motion.
- x-axis: Completes the right-hand rule system (aligned with the relative position Xs)

$$\vec{k} = \frac{V_S}{\|V_S\|} \tag{4.17}$$
$$\vec{j} = \frac{X_S \times V_S}{\|X_S \times V_S\|} \tag{4.18}$$
$$\vec{i} = \vec{j} \times \vec{k} \tag{4.19}$$

Then, we define this last transformation of the covariance matrix as:

$$\Sigma_{T_e} = W \Sigma_{T_S} W^T \tag{4.20}$$

Where W is the matrix that performs the rotation made up by

$$W = \left[\begin{array}{c:c:c} \vec{i} & \vec{j} & \vec{k} \end{array} \right]^T \tag{4.21}$$

With $\vec{i}$, $\vec{j}$ and $\vec{k}$ being the column vectors defined by (4.19), (4.18) and (4.17) respectively. As W is orthogonal and Σ_{T_S} is symmetric, it is shown that $\Sigma_{T_e} = \Sigma_{T_S}$.

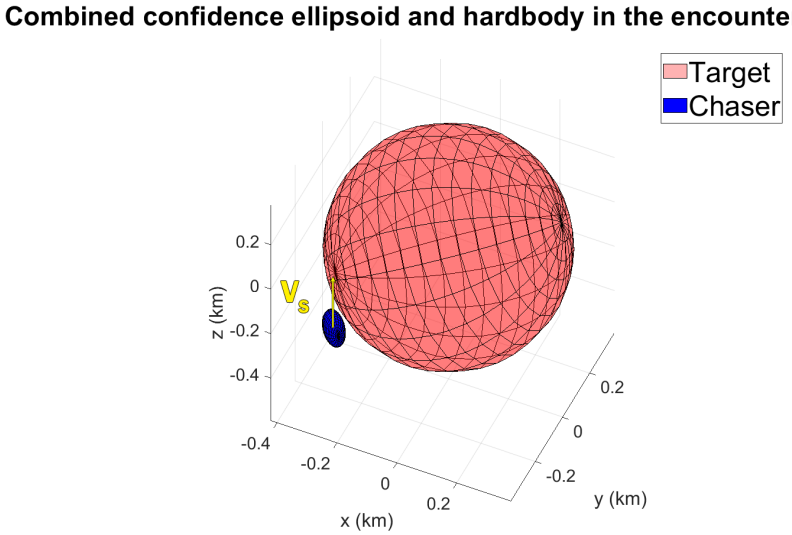

Figure 4.7 Geometries in the encounter frame.

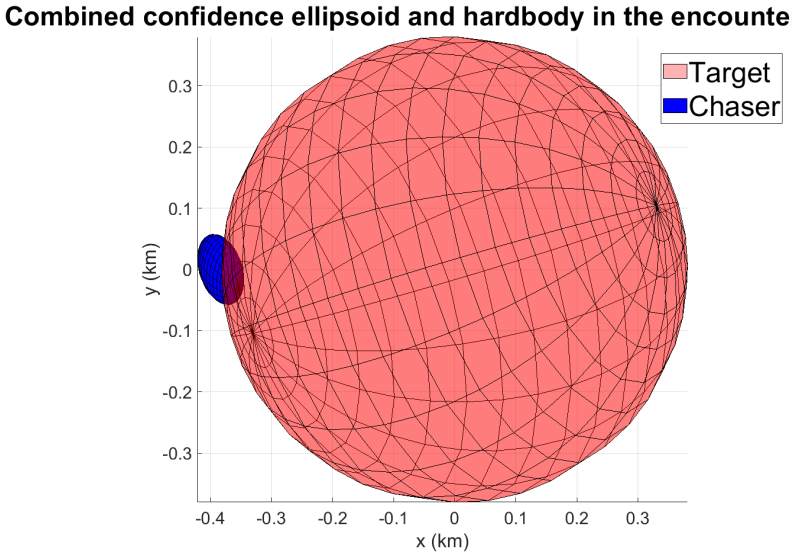

Figure 4.8 Projection of the geometries in the encounter plane (xy plane).

Before we start to compute the probability of collision, a brief explanation of how to transform the geometry of the combined hardbody from the inertial frame to the encounter frame is provided. Once we have placed the combined hardbody at the chaser, we must rotate and scale it into the final encounter frame.

Being f_i a $3 \times n$ matrix that contains the n points of the combined hardbody in the inertial frame at the chaser, we can transform the points into the encounter frame by:

$$f_{i_e} = WSPf_i = Uf_i \tag{4.22}$$

Note that this expression is equally valid when the combined body is not a sphere but any other geometry defined by points in space. The same thing happens with confidence ellipsoids. The method is originally defined assuming that the confidence intervals extend along the three local axes of the satellite, but any other initial error distribution is admissible under the same transformations.

4.2.3 The Method: Probability computation

At this point, we have reduced the two non-diagonal covariance matrices (in the inertial frame) to a single diagonal *spherical* covariance matrix, that is, a diagonal matrix in which all the elements of the diagonal are the same. In addition, the mean is centered on the origin of the coordinate system (target).

The last step in computing the collision probability is to integrate the Gaussian probability density function over the volume swept by the hardbody during the encounter. It should be noted that the initial and final points taken as integration limits are chosen based on a previous study of the problem conditions. Under the hypotheses established in Patera's method and as will be analyzed in depth at the end of this chapter, these initial and final points are usually taken when the chaser is at a $3-5\sigma$ distance from the target.

Hence, by introducing our values into equation (4.1), the integration can be written as:

$$PR_T = \frac{1}{(2\pi)^{3/2}\sigma_1^3} \iiint_V \exp\left[-\frac{x^2+y^2+z^2}{2\sigma_1^2}\right] dx\,dy\,dz \tag{4.23}$$

Note that the probability density along each axis is decoupled from the others so the integral is much easier to divide and solve. The volume of integration will be the entire trail that the combined body will travel in the chaser position passing through the confidence sphere.

In order to solve the integral, firstly we put it in cylindrical coordinates around z, the axis that points towards the velocity direction in the encounter frame:

$$PR_T = \frac{1}{(2\pi)^{3/2}\sigma_1^3} \iiint_V \exp\left[\frac{-z^2}{2\sigma_1^2}\right] \exp\left[\frac{-r^2}{2\sigma_1^2}\right] r\ dr\,d\theta\,dz \tag{4.24}$$

The integration along the z axis is made in incremental steps assuming that probability density, hardbody area, and relative velocity are nearly constant over each time step. We define PR_I as the *differential probability per unit of length in the velocity direction*:

$$PR_I = \left\{ \frac{1}{\sqrt{2\pi}\sigma_1^3} \int_{-\triangle}^{\triangle} \exp\left[\frac{-z^2}{2\sigma_1^2}\right]\ dz \right\} \cdot \left\{ \left(\frac{1}{2\pi}\right) \cdot \iint_S \exp\left[\frac{-r^2}{2\sigma_1^2}\right] r\ dr\,d\theta \right\} \tag{4.25}$$

If the origin of coordinates is included inside the hardbody surface (the other case is developed later), we can easily integrate from 0 to r equation (4.25):

$$PR_I = \left\{ \frac{1}{\sqrt{2\pi}\sigma_1} \int_{-\triangle}^{\triangle} \exp\left[\frac{-z^2}{2\sigma_1^2}\right]\ dz \right\} \cdot \left\{ \left(\frac{1}{2\pi}\right) \cdot \oint_{perimeter} \left(1 - \exp\left[\frac{-r^2}{2\sigma_1^2}\right]\right) d\theta \right\} \tag{4.26}$$

In order not to extend too much the development of the integral, we define

$$PR_C = \left(\frac{1}{2\pi}\right) \oint_{perimeter} \left(1 - \exp\left[\frac{-r^2}{2\sigma_1^2}\right]\right) d\theta \tag{4.27}$$

As the *contour integral of the hardbody*, which will be developed later.

Then, the integral that remains to be analyzed is:

$$PR_I = \frac{1}{\sqrt{2\pi}\sigma_1} \cdot PR_C \int_{-\triangle}^{\triangle} \exp\left[\frac{-z^2}{2\sigma_1^2}\right] dz \tag{4.28}$$

Note that e^{-z^2} is the Gaussian function from which it is impossible to obtain an analytical formula of its integration in a non-infinite enclosure. However, since we are integrating into very thin

sections of z, we can apply the *trapezoid rule* to obtain an analytical formula without misleading [25]:

$$PR_I = \frac{\triangle z}{\sqrt{2\pi}\sigma_1} \exp\left[\frac{-z^2}{2\sigma_1^2}\right] PR_C \tag{4.29}$$

Now, if this expression is divided by the increment of time during which the distance $\triangle z$ is traveled, one gets the *collision probability rate* PR_R:

$$PR_R(t) = \left(\frac{\triangle z(t)}{\triangle t}\right)\left(\frac{1}{\sqrt{2\pi}\sigma_1}\right) \exp\left[\frac{-z^2(t)}{2\sigma_1^2}\right] PR_C \tag{4.30}$$

Assuming that the velocity is constant during the differential time:

$$PR_R(t) = \left(\frac{V_z(t)}{\sqrt{2\pi}\sigma_1}\right) \exp\left[\frac{-z^2(t)}{2\sigma_1^2}\right] PR_C \tag{4.31}$$

The collision probability rate or point probability of collision for a given $z(t)$ is then evaluated for a set of times spanning the encounter. The collision probability rates are integrated over the time of interest to obtain the total collision probability associated with the time interval from t_1 to t_2

$$PR = \int_{t_1}^{t_2} PR_R(t)\ dt \tag{4.32}$$

The time duration associated with the change from equation (4.30) to (4.31) depends on the dynamics of each particular encounter. The number of steps required is found in the usual manner by simply increasing the number of steps until the resulting probability does not vary appreciably by increasing the number of steps. The more curved the trajectory is, the smaller should be the time step. In general, several hundred time steps per encounter is enough.

Let us, before continuing with the methodology, highlight a geometrical consideration of the method which is the consequence of the step taken between equation (4.28) and equation (4.29): the infinitesimal length dz turns into a non-infinitely small length named $\triangle z$. Thus, the geometrical consideration is nothing but pointing that the volume swept by the combined hardbody in the error ellipsoid is composed of small adjacent tubes, whose combination will leave gaps and overlaps.

These gaps and overlaps, represented in Figure 4.9, seem to clearly worsen the quality of this method. However, Patera states that given that the gaps and overlaps represent very closed probability volumetric regions in the confidence region, the effect of one counteracts the contribution of the other [26]. This assertion implies that one does not need to excessively decrease the size of the tubes to avoid them.

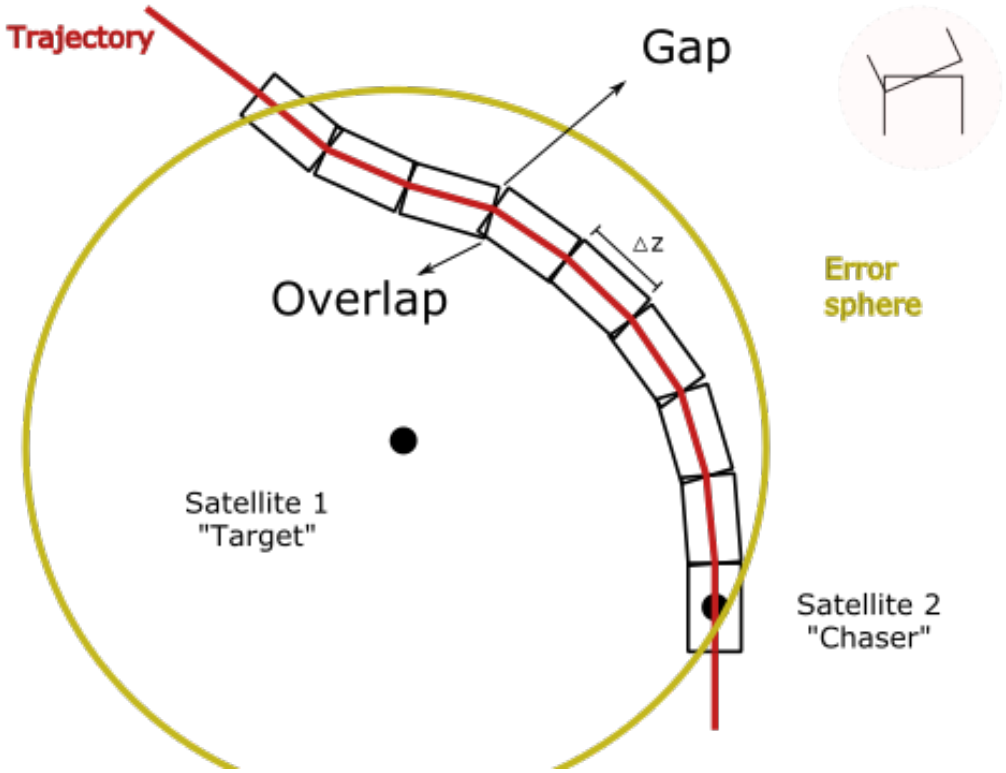

Figure 4.9 Pieces of the tube, showing the appearance of gaps and overlaps.

Numerical Integration About Contour

The cross-track contour integration over the hardbody region is performed for each incremental time step. The shape of the contour and the value of the integral can change for each increment because of changes in relative velocity, probability density, etc.

The points defining the shape of the hardbody volume f_i were transformed to the encounter frame f_{ie} (4.22) and projected to the encounter plane (Figure 4.8). By means of a *convex hull* [27] the points that define the outer perimeter are obtained (Figure 4.10). These points are used in the evaluation of the contour integral and are enumerated sequentially in a counterclockwise direction along the perimeter.

The angle between two position vectors that define two consecutive points $\mathbf{X_i}$ and $\mathbf{X_{i+1}}$ is given by $d\theta_i$. By noting its relationship to the cross product between two vectors of the same plane, $d\theta_i$ can be obtained from

$$\mathbf{X_i} \times \mathbf{X_{i+1}} = \|\mathbf{X_i}\|\|\mathbf{X_{i+1}}\| \sin(d\theta_i) \tag{4.33}$$

And rearranging the equation:

$$d\theta_i = \sin^{-1}\left(\frac{\mathbf{X_i} \times \mathbf{X_{i+1}}}{\|\mathbf{X_i}\|\|\mathbf{X_{i+1}}\|}\right) \tag{4.34}$$

In relation with the last increment, remind that if the total number of points used in completing one circuit about the contour is n, then $\mathbf{X_{n+1}}$ is $\mathbf{X_1}$.

The exponential term in the i^{th} exponential integrand of (4.27) is evaluated as

$$integrand_i = \exp\left[-\frac{\left(\|\mathbf{X_i}\|^2 + \|\mathbf{X_{i+1}}\|^2\right)}{4\sigma_1^2}\right] \tag{4.35}$$

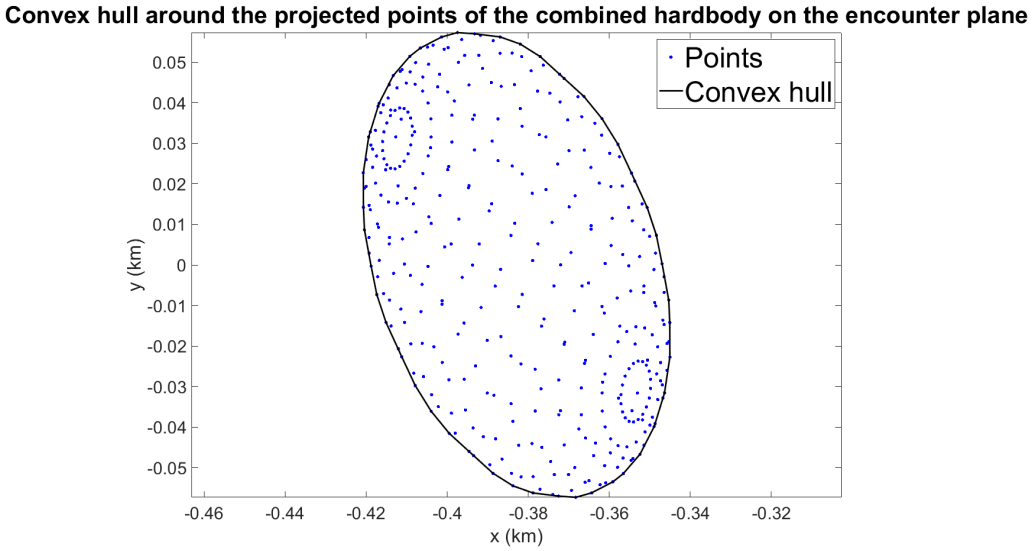

Figure 4.10 Convex hull around the points.

Then, the integral is evaluated by summing the values of $integrand_i$ times $d\theta_i$ for each pair of points around the contour:

$$sum = \sum_{i=1}^{n} integrand_i \cdot d\theta_i \tag{4.36}$$

And the value of PR_C (4.27) is

$$PR_C = 1 - \frac{sum}{2\pi} \tag{4.37}$$

Note that if the origin of coordinates is not inside the hardbody, the integration of equation (4.25) couldn't be made from 0 to r. In that case, we should integrate from r_1 to r_2 sweeping θ as shows Figure 4.11 and the integral would be of the form

$$PR_C = \left(\frac{1}{2\pi}\right) \oint_{perimeter} - \left(\exp\left[\frac{-r_2^2}{2\sigma_1^2}\right] - \exp\left[\frac{-r_1^2}{2\sigma_1^2}\right]\right) d\theta \tag{4.38}$$

Take into account the sign of $d\theta$: Always positive (counterclockwise) when the origin is included but changing its sign when sweeping the points in the external case (Figure 4.11). In that case, the farther points are integrated as positive since they are swept counterclockwise, whereas the closer points are integrated as subtractions because they are swept clockwise. In this way, the integrand of (4.38) can be reduced to $integrand_i$ times $d\theta_i$ and therefore the cumulative probability is given by

$$PR_C = -\frac{sum}{2\pi} \tag{4.39}$$

With equation (4.37) the one applied when the origin of coordinates is within the contour and equation (4.39) the one applied when it is not within the contour.

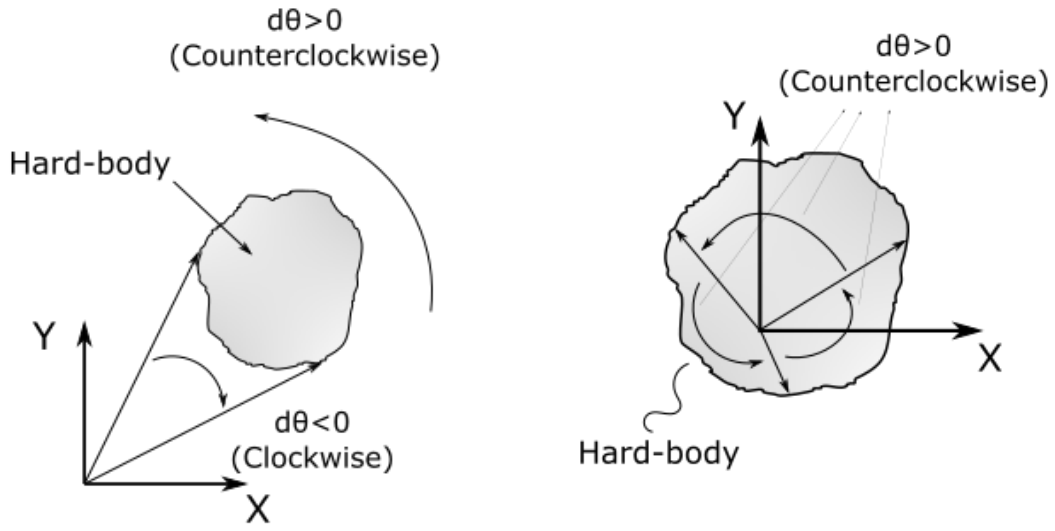

(a) The hard-body does not contain the origin.

(b) The hard-body contains the origin.

Figure 4.11 Integration difference.

In addition, Patera defined an alternative way to calculate this integral in which it is not necessary to know if the center is contained in the enclosure because an additional change of coordinates is made that transfers the section to the origin of coordinates [28]. By doing that, the computation time is reduced even more. However, it is an unnecessary development that falls outside the scope of this project.

4.3 Method validity

Once the method has been completely defined and correctly implemented in a script, it is convenient to carry out a simulation to check its validity and to what extent it adjusts to reality. First, a simple linear simulation with an analytical solution will be done.

Furthermore, to verify the veracity of this method not only in the linear case but also in the non-linear case, in parallel, a script that allows computing the probability of collision by means of a Monte Carlo generation was developed.

This alternative method consists of applying what is stated in Figure 4.9 and under the same starting conditions as Patera's method: The covariance matrices are generated in each of the bodies and subsequently they are rotated and added together in the inertial frame.

Then, the points are generated by Monte Carlo following the combined covariance matrix and placed at the target. Next, and after placing the combined hardbody at the chaser, the space is rotated to access the encounter frame (the scaled system is skipped). For each time increment, the geometry of a fragment of the tube is defined and the points contained within it are counted.

Finally, and after generating the pmf (dividing the counted points in each increment by the total number of points generated) and cdf function, the result is compared with the one obtained with Patera's analytical method.

It should be noted that an absolute propagator (Keplerian) has been used for the simulations.

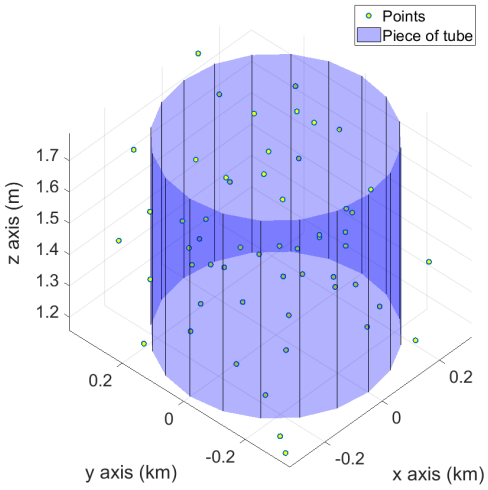

Figure 4.12 Points inside a piece of tube. For each time step, all the points that verify to be inside the area projection and within a $\triangle z$ region are counted.

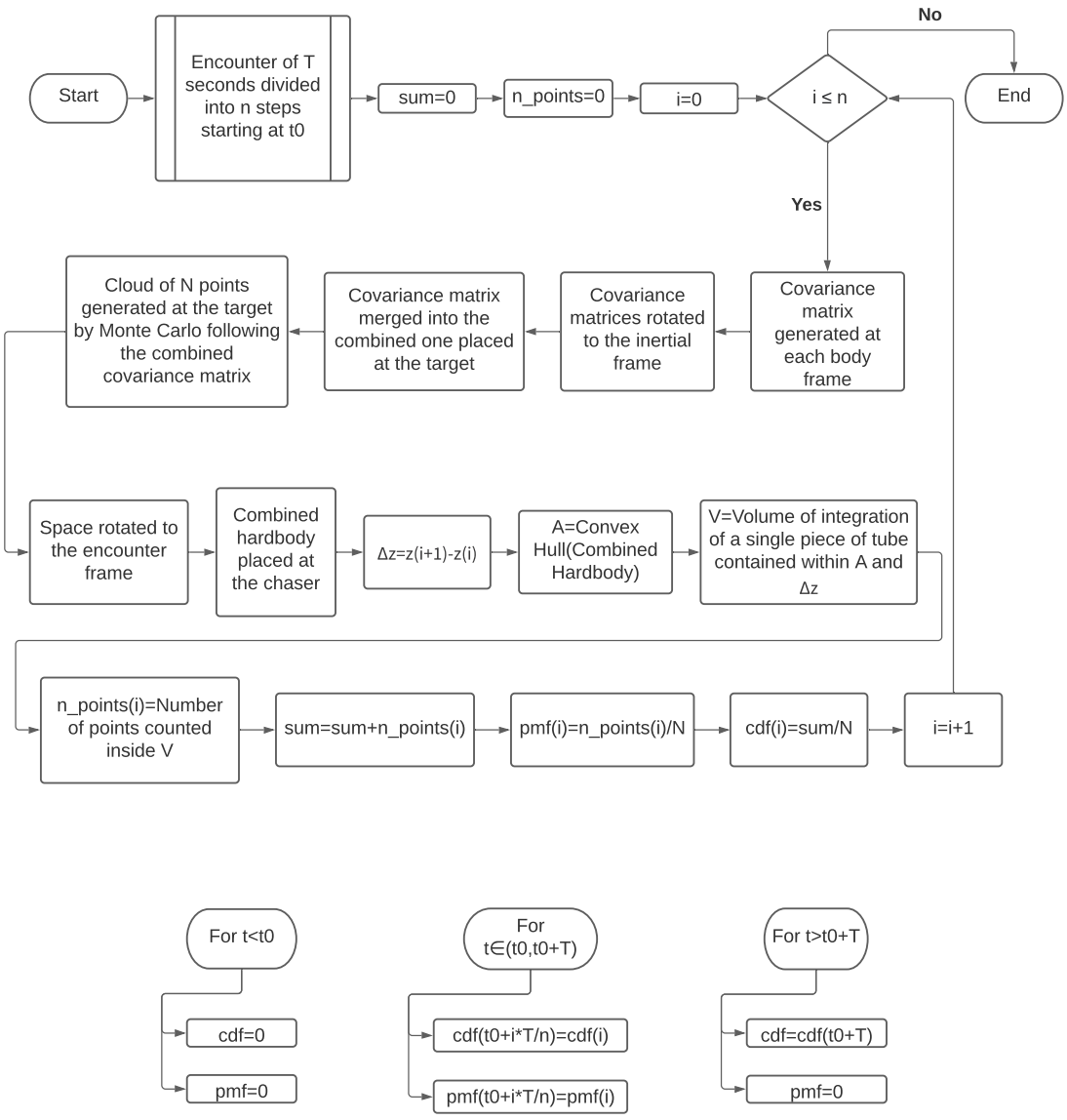

Figure 4.13 Steps followed to obtain the pmf and cdf functions using Monte Carlo.

4.3.1 Linear case

In order to know exactly the deviation with respect to the exact real probability, a simple linear problem has been simulated with a spherical covariance matrix of standard deviation σ and a spherical combined hardbody of radius R that completely crosses the error cloud through the center.

Due to the simplicity of said geometry, an analytical solution can be obtained that gives us the exact probability of collision for these conditions. The result was compared with the one obtained by the calculation using Patera's method.

Introducing this concept illustrated in Figure 4.14 into (4.23), the probability of collision is given by:

$$\begin{aligned} PR_T &= \frac{1}{(2\pi)^{3/2}\sigma^3} \iiint_V \exp\left[-\frac{x^2+y^2+z^2}{2\sigma^2}\right] dx\,dy\,dz = \\ &= \frac{1}{(2\pi)^{3/2}\sigma^3} \int_0^{2\pi}\int_0^R e^{-\frac{r^2}{2\sigma^2}} \cdot r \; dr\,d\theta \cdot \int_{-\infty}^{\infty} e^{-\frac{z^2}{2\sigma^2}} \; dz = \\ &= \frac{1}{(2\pi)^{3/2}\sigma^3} \cdot 2\pi\sigma^2 \left(1 - e^{-\frac{R^2}{2\sigma^2}}\right) \cdot \sqrt{2\pi}\sigma = \\ &= 1 - e^{-\frac{R^2}{2\sigma^2}} \end{aligned} \tag{4.40}$$

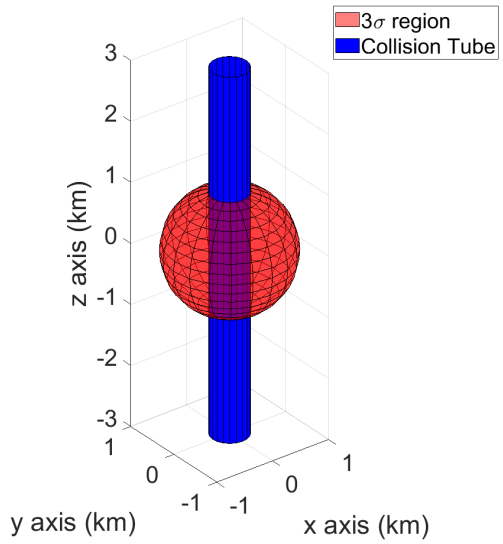

Figure 4.14 Simple linear problem with analytical solution.

The relative error of each method with respect to the analytical result as a function of the time step is presented in the following tables. As the encounter is completely rectilinear, it fits the definition of linear perfectly. In addition, regarding the Monte Carlo method, it was also studied how it affected the number of points generated.

Table 4.1 Deviation of the solution with respect to the analytical solution using Patera's method for different time steps for a linear encounter.

Step size(s)	Rel. error
0,01	5e-09
0,005	6e-09
0,0025	1e-08
0,001	9e-10
0,0005	3e-09

Table 4.2 Deviation of the solution with respect to the analytical solution using a Monte Carlo based method for different time steps and number of points for a linear encounter.

Rel. error	Number of points generated					
Step size(s)	1.000	5.000	10.000	50.000	100.000	500.000
0,01	2e-03	2e-03	2e-02	3e-03	2e-02	1e-03
0,005	8e-03	6e-03	2e-03	1e-03	1e-03	9e-05
0,0025	3e-02	3e-03	1e-02	1e-03	1e-03	6e-04
0,001	6e-03	7e-03	7e-03	5e-03	7e-05	1e-03
0,0005	4e-03	5e-03	3e-03	1e-03	1e-03	7e-04

It is observed that the relative error using Patera's method is extremely small and therefore its use is validated for the linear case. By decreasing the integration step, no improvement of the solution is observed; this is because the result is by nature exact and the errors are due to tolerances in the calculation of the integral or propagation.

In turn, the Monte Carlo based method also provides a valid solution (presented error of 0.01-1%, being the mean 0.1%). Despite being a much larger error than the one obtained with Patera, it is low enough to assume that the method has been implemented correctly, which is what we are really interested in.

4.3.2 Non-linear case

After studying the linear case and observing that Patera's method could be reliable enough to be able to apply it to the non-linear case, the same comparison was made for a non-linear problem.

However, since there is no exact value on which to base ourselves, it is not possible a priori to know with certainty what error the calculation of the non-linear case is presenting.

Nevertheless, that does not say that we cannot get an idea of said error. After comparing both methods in the linear case and observing that both, with a different algorithm, give very similar results, it is a sufficiently solid reason to be able to suppose that the solution of the non-linear case will be approximately correct if both methods converge again in a similar way they did with the linear case.

In this case, the solution provided by Patera (being, in theory, the closest to reality), is taken as a reference, and compared with the one provided by Monte Carlo under the same initial conditions.

Table 4.3 Relative error between the solution provided by Patera's method and Monte Carlo simulation for different time steps and different number of points for a non-linear encounter.

Rel. error	Number of points generated					
Step size (s)	1.000	5.000	10.000	50.000	100.000	500.000
0,01	6e-02	4e-03	9e-04	6e-03	6e-03	2e-03
0,005	1e-02	1e-02	9e-03	2e-03	2e-03	1e-03
0,0025	5e-02	1e-03	1e-02	3e-02	5e-03	1e-03
0,001	1e-02	7e-03	1e-02	4e-03	1e-03	7e-05
0,0005	5e-02	4e-02	5e-03	1e-04	1e-03	5e-04

Table 4.4 Time elapsed in each comparison.

Elapsed time (s)	Number of points generated					
Step size (s)	1.000	5.000	10.000	50.000	100.000	500.000
0,01	1,16	1,23	1,38	3,33	5,61	24,32
0,005	2,11	2,38	2,6	6,50	11,04	48,22
0,0025	4,03	4,48	4,96	12,78	21,90	96,83
0,001	9,69	10,93	11,99	31,54	54,18	241,13
0,0005	19,21	21,79	24,09	63,08	108,17	481,44

It can be seen that the error of the Monte Carlo method with respect to Patera's method is of the same order as in the linear case; this is the main reason that leads us to think that both methods are implemented correctly and equally valid for long-term encounters.

As in the linear case (Table 4.2), we observe a practically negligible evolution as the time steps/number of points generated vary (Table 4.3). The explanation for this behaviour is due to the way the algorithm is constructed.

As the satellites move, they change not only their relative position but also their relative orientation. This causes the point cloud oriented on the main axes of each satellite to constantly vary in the inertial system and therefore the shape of the point cloud between each step must be constantly regenerated.

To implement this behavior in the Monte Carlo method, a different point cloud is generated in each step, and therefore the variability of said points is greatly increased. This generates a completely heterogeneous solution even when using large steps / few points because statistically the points that are undercounted in one step will be counted over in successive steps until reaching equilibrium.

If we generate more points and take smaller intervals we can slightly reduce the error, but it does not compensate for the computation time it takes (Table 4.4).

This heterogeneity in the solution, however, has its obvious drawback: it will be very difficult to guarantee a very small error of the order of the one obtained with Patera's method if we generate a cloud of points in each interval because such variability will introduce points that should not have been counted and remove points that should have been counted.

To solve this problem, a variation should be implemented in the method that, at a certain $d\sigma$, fixes the dimensions of the combined confidence ellipsoid and calculates the collision probability by counting its points without generating another different one.

In fact, this study will be carried out in the next section and implemented in the method due to the real impossibility of knowing at every single step the shape of the confidence region.

Appropriate number of steps to apply Patera's method

After all the previous analysis that has served to guarantee the effectiveness of Patera's method, a more in-depth analysis of the time step size is performed. A 20 seconds encounter with a starting and finishing distance fixed to 6σ is analysed. It is therefore studied how the solution of Patera's method varies by varying the integration step.

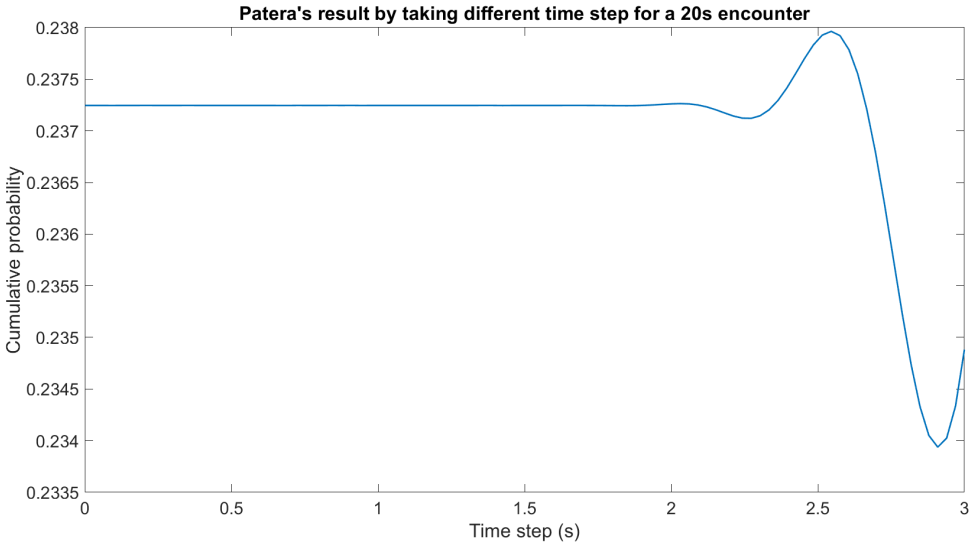

Figure 4.15 Patera's solution for different time steps from 0.1 to 3.

We can see in Figure 4.15 how for a time step lower than 2 the solution begins to converge. An in-depth analysis of the convergence zone is then carried out.

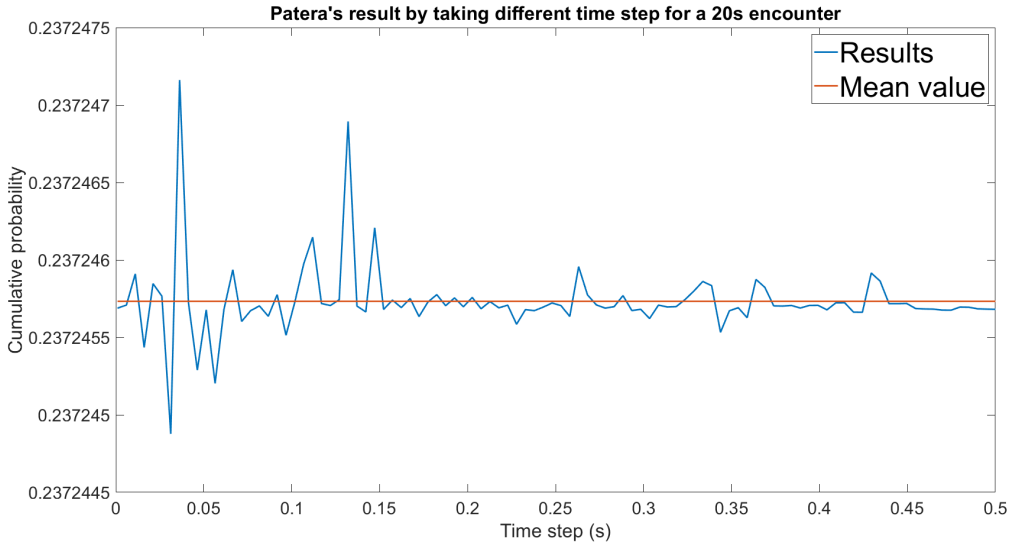

Figure 4.16 Patera's solution for different time steps from 0.01 to 0.05.

Figure 4.16 shows how from a certain time step the solution converges to a mean value and shows a noisy behavior around it. This is because there comes a time when the time interval is smaller than the tolerances of propagation, integration, etc., and decreasing it does not provide greater accuracy to the solution and, on top of that, means more computing time. It is observed that for a time step of around 0.2 seconds (100 divisions of the integration tube) a value around the mean value is obtained with a certain relative error of $2e-07$ and a computation time of only 0.101 seconds.

Table 4.5 shows the different errors with respect to the mean for different time intervals and the time spent. It should be noted that the more curved the trajectory, the greater number of pieces will be necessary. Note that although in Figure 4.16 the difference seems to be large, the relative errors keep low enough.

Table 4.5 Time elapsed and relative error for each decrease of the time step.

Time step (s)	Time elapsed (s)	Relative error	Number of pieces
0.5	0.075	2e-07	40
0.2	0.101	2e-07	100
0.1	0.1334	1e-07	200
0.05	0.248	5e-08	400
0.01	1.23	2e-07	2000

Therefore, and as the author mentions in his numerous publications, we conclude that dividing the encounter into hundreds of steps is enough to get an optimal result.

4.4 In-depth analysis of collision probability

The probability of collision during an encounter between two bodies depends on many factors. It is influenced mainly by the expected miss distance, namely, the minimum distance between the bodies. However, it is interesting to note what influences the collision probability for a fixed relative path between the bodies.

If Patera's method is analyzed, it is observed that given a fixed relative trajectory and under the previously assumed hypotheses, the collision probability depends exclusively on the size of the eigenvalues of the combined position covariance matrix (degree of uncertainty) and the cross-section of the combined hardbody.

4.4.1 Uncertainty in position: Dilution region

For a given trajectory and combined hardbody, Figure 4.17 shows the relation between the probability of collision and the uncertainty of the position. A reference combined positional covariance matrix is multiplied by a scalar factor and the probability is computed.

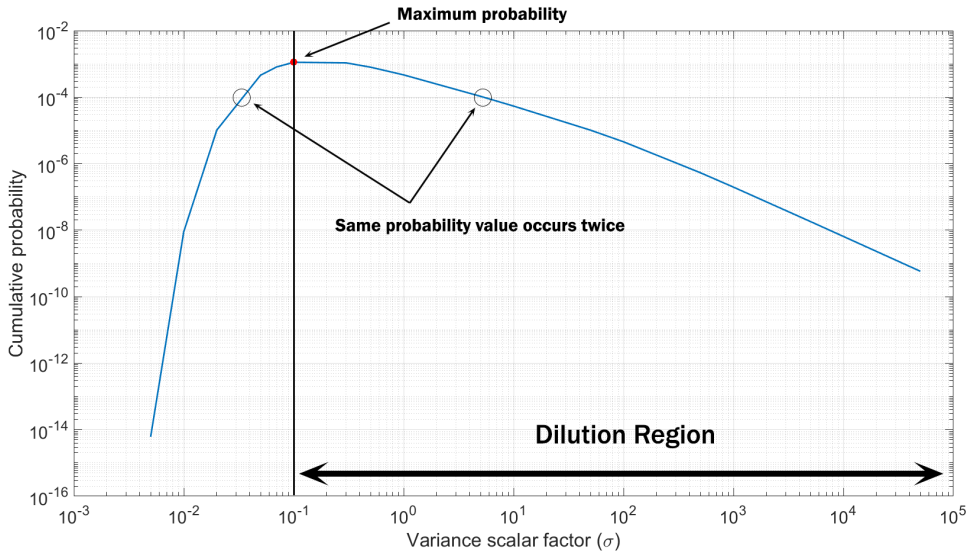

Figure 4.17 Relation between the probability of collision and the uncertainty of position.

The scaled, combined covariance that produces the maximum probability defines the dilution region boundary [4]. To the left of this boundary, lesser positional uncertainty (smaller σ) decreases collision probability. To the right of the boundary, larger positional uncertainty (greater σ) also decreases collision probability. As shown, both small and large uncertainties can produce the same mathematically correct probability.

A very large uncertainty indicates little confidence in the predicted miss distance and thus will result in a low probability of collision, **deceptively implying that satellite safety increases as data quality decreases.**

Faced with a low probability of collision below an actionable threshold, one could use the dilution region boundary as a discriminator. If outside the dilution region, then no remedial action is warranted. If inside the dilution region, rather than dismiss the conjunction as non-threatening, one should consider getting better (more current) data and reevaluating the probability of collision. This will help to ensure that a decision-maker is not lulled into a false sense of security by a low probability calculation that may be specious.

There is currently a large list of approaches to deal with epistemic uncertainty [29]. An epistemic uncertainty is uncertainty due to imperfect knowledge about the quantity or event being analysed. One of the many ways in which epistemic uncertainty can arise in a fixed quantity is if the data used to measure or infer it are subject to random errors.

These approaches include subjective Bayesian probability, classical fuzzy theory, confidence distributions, fiducial distributions and Dempster-Shafer theory. However, no approach has yet emerged as the dominant. Therefore, when dealing with the problem of probability dilution, the user has a wide range of tools to employ. Nevertheless, exclusively from a theoretical point of view, since the problem has not yet been solved.

The current approach to not incur probability dilution is to insist on data that is accurate enough. However, better data is not always available. The accuracy of satellite position and velocity measurement is limited by the available hardware. And even if the hardware is improved, the best available tracking data may not be accurate enough to eliminate probability dilution.

4.4.2 Uncertainty in size of the combined hardbody

The size and form of a space object also play an essential role in the estimation of the probability of collision. In an ideal model, that information would be given by satellite operators as a function of the bodies' orientation. However, in practice, such information is unavailable for operating spacecraft, and for debris, it is almost always unknown.

The size of the orbiting objects is in general estimated from *Radar Cross Section* measurements using the appropriate model.

At this point, one wonders how the uncertainty in the size estimation affects the estimation of the probability of collision. Figure 4.18 shows the collision probability result obtained considering the radius of a reference spherical body multiplied by a certain scalar factor.

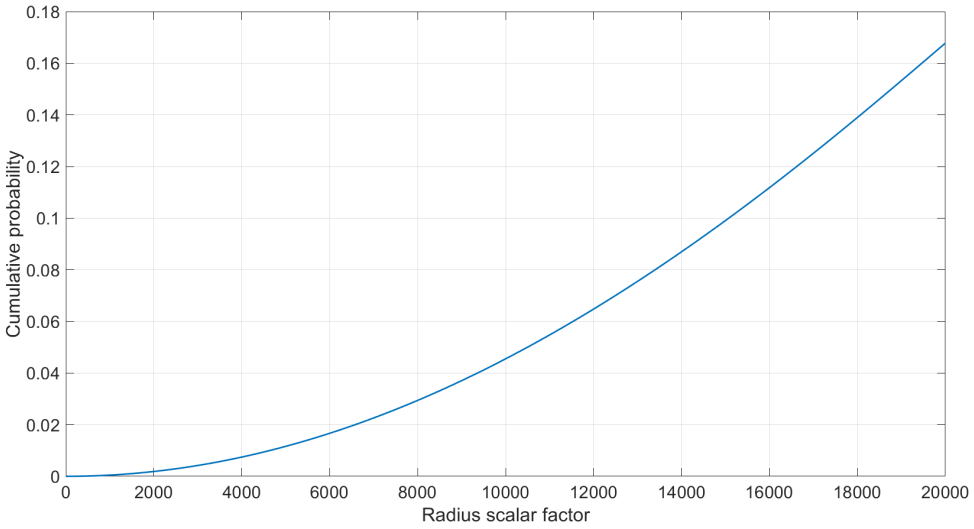

Figure 4.18 Relation between the probability of collision and the size of the object.

It is observed that the increase in the probability of collision grows at a quadratic rate. This relationship is due to the fact that the combined object area in the encounter plane is proportional to πr^2. It is concluded that the larger the size, the greater the estimated probability, and the use of accurate object size information is critical to the accurate estimation of collision probability.

4.4.3 Dilution region and miss distance

It is also interesting the relation between the miss distance of an encounter, the size of the combined error ellipsoid (uncertainty during the encounter) and the size of the combined hardbody.

What intuition tells us, and which is validated by the simulations, is that given a certain encounter, the collision probability dilution region will be reached if the region predefined as 3σ is notably greater than the minimum distance during the encounter (miss distance) plus the radius of the combined hardbody.

What happens in reality is that, for a uncertainty region smaller than the miss distance, the probability of collision is nearly zero since not even in the worst case there could be a collision. This mathematically translates into the integral of the tube being zero (Figure 4.19).

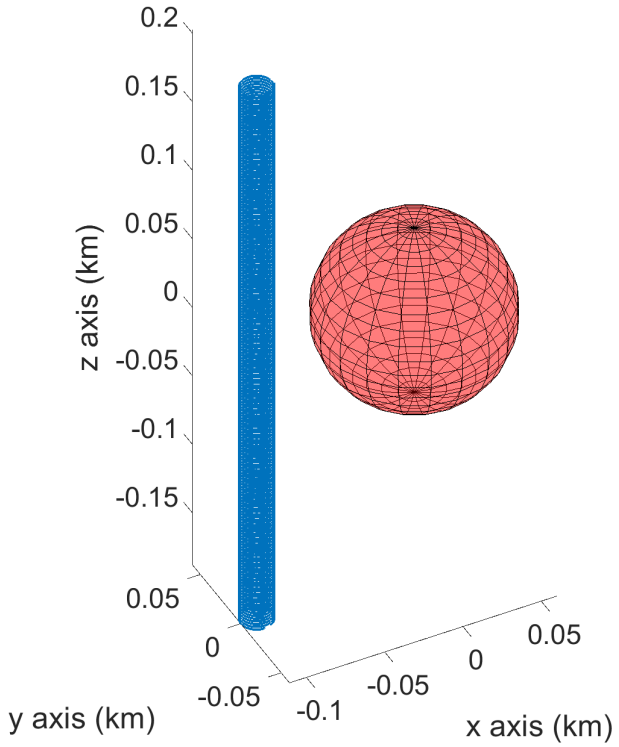

Figure 4.19 3σ uncertainty region smaller than the miss distance.

However, as uncertainty increases, risk begins to appear as it is increasingly possible that there could be an impact. This implies that as uncertainty increases, a greater amount of probability is integrated within the tube (Figure 4.20).

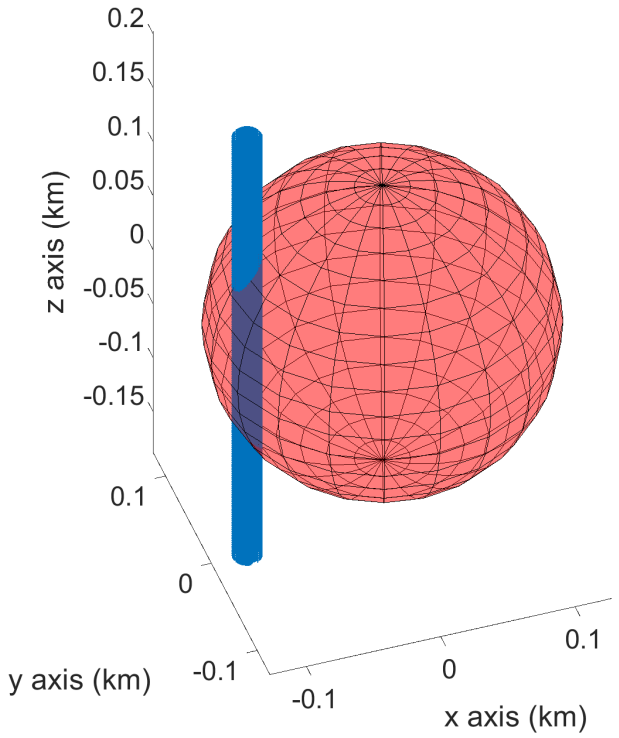

Figure 4.20 3σ uncertainty region including the miss distance.

Finally, there comes a time when the uncertainty is so large that there is even the probability that one of the bodies is in a position considerably further away than that predicted by the miss distance, diluting the risk of collision and providing a false idea of security (Figure 4.21).

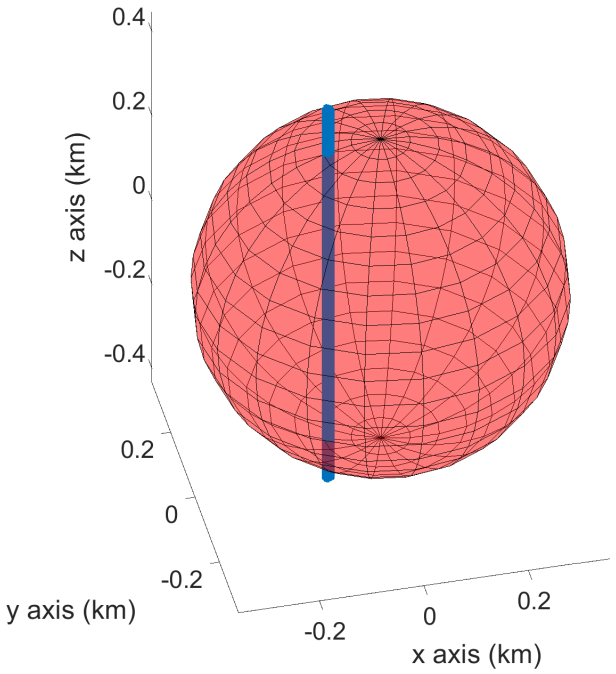

Figure 4.21 3σ uncertainty region much bigger than the miss distance.

At this point one wonders how the cumulative probability curves of a certain fixed encounter are related for different values of uncertainty and radius of the combined hardbody.

Figure 4.22 shows the relationship between the different variables and the accumulated probability during the encounter. Although it is observed that for different values of combined hardbody radius the maximum probability peak, that is, the one that marks the beginning of the dilution zone, is obtained for the same uncertainty value (Figure 4.23), the evolution of the curves is not the same.

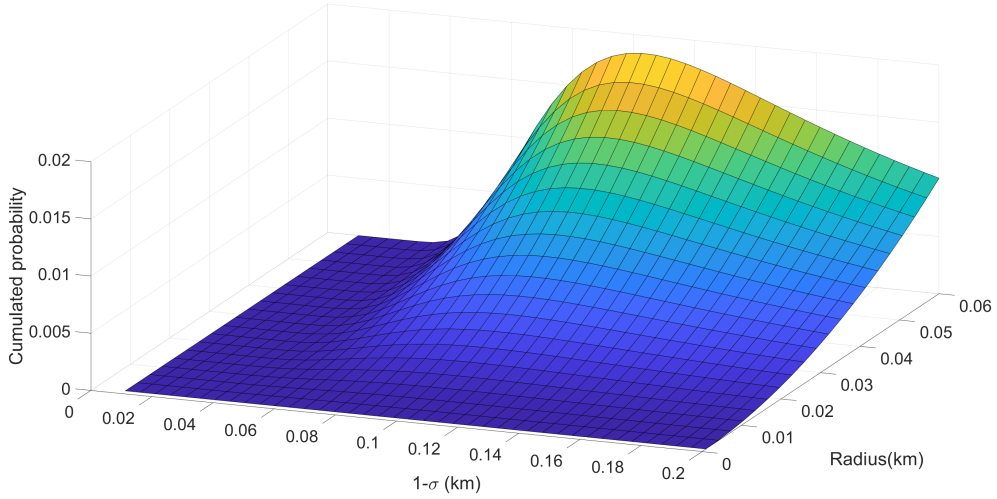

Figure 4.22 Relation between the probability of collision, the uncertainty and the radius of the combined hardbody for the same fixed encounter.

In Figure 4.24 it is observed how for higher values of the combined hardbody radius the accumulated probability is much more sensitive to changes of uncertainty.

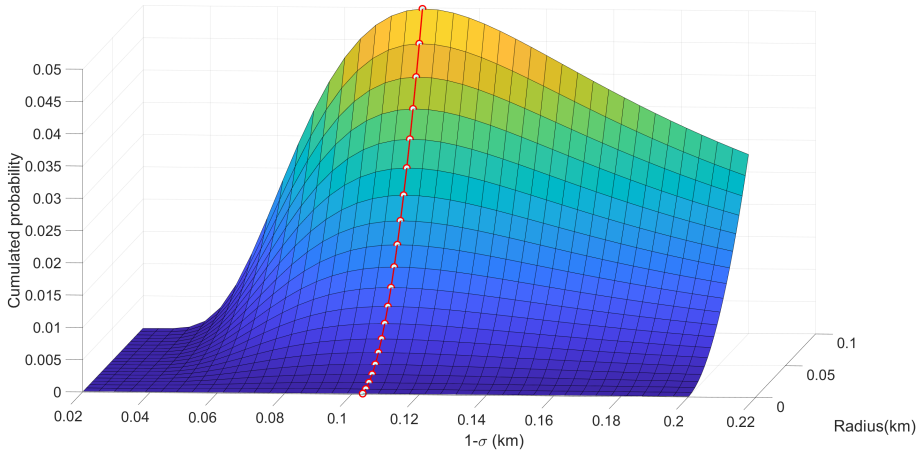

Figure 4.23 Points at which the maximum cumulative probability values are reached.

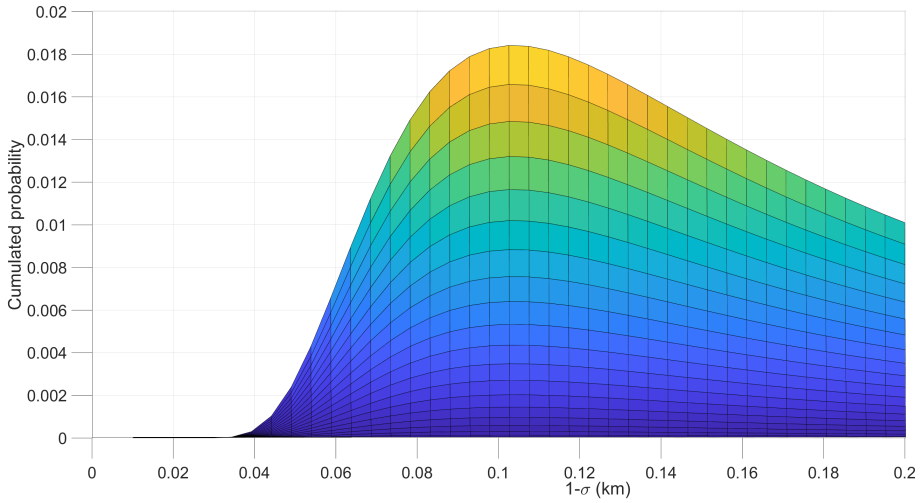

Figure 4.24 Evolution of the cumulative probability when varying the uncertainty for different values of combined hardbody radius.

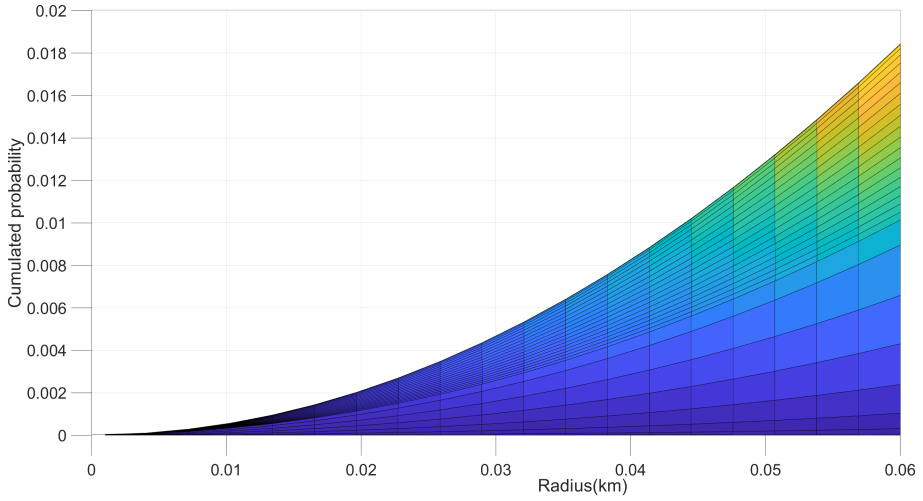

Figure 4.25 Evolution of the cumulative probability when varying the combined hardbody radius for different values of uncertainty.

4.4.4 Uncertainty during the encounter

As previously introduced, in reality, the positional error covariance matrix is not known at all times, nor does it remain constant. In fact, what occurs rather is that a certain covariance matrix is estimated at a certain instant and, until the next position estimate, said covariance matrix, in turn, becomes larger as the position errors increase stochastically.

In addition, for a large relative distance between the bodies, the uncertainty is huge. This leads us to estimate the probability of collision being within the dilution zone and therefore obtain an unrealistic result.

Limits of integration

The solution to this problem is to not start calculating the probability of collision until the bodies are at a certain distance. This distance will be given by the Mahalanobis distance, and it will be essential to choose a distance at which the bodies are close enough (the smallest possible distance) to have better estimates of size and position but without diminishing the result due to not integrating part of the enclosure with a relevant probability density value.

Figure 4.26 shows the evolution of the accumulated probability of collision during a 30-second encounter when starting to integrate at a certain Mahalanobis distance d. As the covariance matrix is diagonal and spherical, it is not necessary to take into account the orientation of the confidence ellipsoid (sphere) and therefore the region begins to be integrated within the tube when the combined hardbody is simply at $d-\sigma$ from the target.

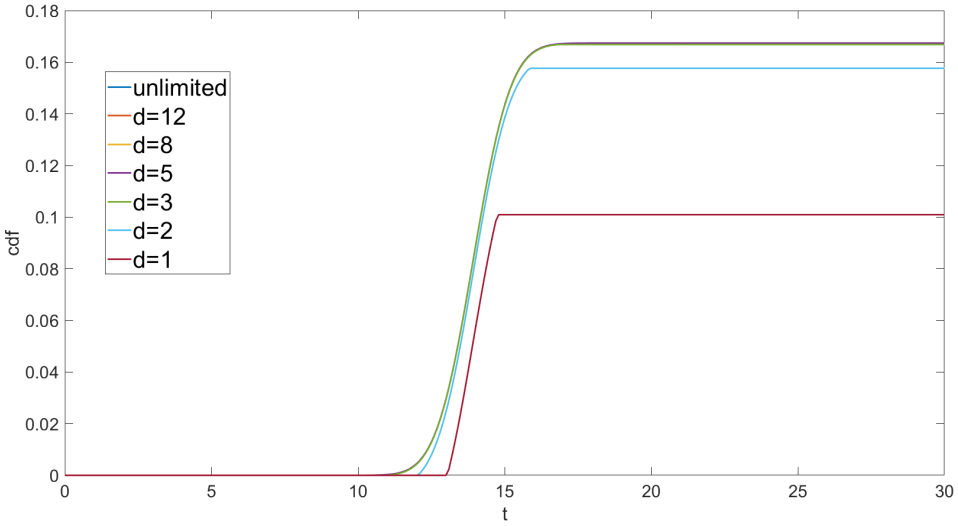

Figure 4.26 Accumulated probability of collision when starting to integrate at a certain Mahalanobis distance d.

Note how for $d=1$ the cdf abruptly variates at the points where the probability calculation starts/ends. This is because the probability density was already high enough at those points and therefore a sharp variation occurs. This entails a great loss of information and its result is therefore completely invalid.

Table 4.6 shows the relative error with respect to the value that would be obtained if the integration had started/ended from infinity as well as the reliability percentage for each distance.

It should be noted that the accuracy values obtained in the solution closely resemble the confidence of a one-dimensional Gaussian distribution for the different Mahalanobis distances (especially $d=1,2,3$). Its similarity is because thanks to the geometric transformation the combined ellipsoid becomes a sphere and therefore resembles the one-dimensional case. There is still a small discrepancy since not a point is integrated but a cross-section and therefore the effective distance $d-\sigma$ is diffuse.

Table 4.6 Relative error and accuracy for different integration limits $|d-\sigma|$.

d	Rel. error	Accuracy
12	5e-40	100%
8	2e-15	100%
5	3e-07	100%
3	3e-3	99.67%
2	3e-02	94.18%
1	4e-01	60.3%

Variation of the positional covariance matrix during the encounter

At this point, the concept of a constant positional covariance matrix during the encounter is developed. Due to the relatively short time in which the encounter occurs and that the bodies hardly vary their absolute orientation, for a not excessively long encounter it can be perfectly assumed that the covariance matrix does not vary. This implies that once a certain distance is reached, the confidence ellipsoid "freezes" and the integration within the tube begins until the integration region ends.

Table 4.7 shows the relative error and accuracy with respect to the value obtained for the integration within the $d-\sigma$ region without freezing the covariance matrix.

Table 4.7 Relative error and accuracy with respect to the value obtained for the integration within the $d-\sigma$ region without freezing the covariance matrix.

d	Rel. error	Accuracy
12	7e-03	99.23%
8	5e-03	99.47%
5	3e-03	99.66%
3	2e-3	99.8%
2	9e-04	99.91%
1	4e-05	99.99%

Obviously, the greater the distance at which we freeze the uncertainty ellipsoid, the greater the time that elapses and therefore the greater the variation of the covariance matrix during the encounter. However, the accuracy is still high even for the case of $d = 12$.

Integration region limited and constant

Table 4.8 shows the conclusion of this subsection: the accuracy in the result between the result without limits and varying the covariance matrix with respect to the case limited to the distance $d-\sigma$ with a frozen covariance matrix.

Table 4.8 Accuracy from freezing and starting to integrate at $d-\sigma$ with respect to the unlimited variable case.

d	Total accuracy
12	99.23%
8	99.47%
5	99.66%
3	99.47%
2	94.09%
1	60.29%

Therefore, it is observed that the gross weight of the error concerns especially the limits of integration, while the consideration of a constant covariance matrix slightly affects the accuracy of the result when taking limits of integration that are too large.

As a result, it will be assumed for the next chapter that limiting the integration to 5σ *or* 3σ while keeping the covariance matrix constant does not lead to a drastic decrease in the reliability of the result.

5 Extensions and validity of Patera's method under the HCW model

After completely defining the method using an inertial reference system and an absolute propagator (Keplerian) under a series of ideal hypotheses, in this chapter we proceed to apply slight modifications to the conditions under which the method was developed.

First, we will proceed to define the problem from a local point of view, and for this, we will use the HCW equations (2.35).

Subsequently, it will be analyzed how the unavoidable presence of uncertainty in the measurements of the velocity of both bodies influences the estimation of the risk of collision.

Finally, it is analyzed how the effect of the perturbations affects the uncertainty and worsens the estimate of collision probability. It will also be analyzed how the white Gaussian noise can be used to model uncertainty caused by unknown perturbations.

As it is a requirement to be able to use the HCW equations that the target is in a circular orbit, throughout this section simulations with zero eccentricity target orbits were performed. However, in practice, the orbits have a certain eccentricity. For this reason, in the same way, it has been analyzed to what extent the HCW equations can be used for targets in slightly eccentric orbits.

5.1 Analysis of the method using the HCW equations

To use Patera's method with a relative propagator such as the HCW equations, it is necessary to make a series of considerations.

First of all, it should be noted that the amount and type of information required, of course, is the same as in the general case. We, therefore, need the uncertainty information of both bodies, their size and shape, and their positions. The initial mean relative position and velocity of the chaser with respect to the LVLH non-inertial reference frame centered and oriented with the target are assumed to be known, as well as the mean absolute position and velocity of the target.

Given the initial conditions, the relative position between chaser and target is propagated with the HCW equations. Although the problem at this moment can indeed be posed as if we were already in the principal frame, there is the problem of the orientation of the bodies and with it the orientation of the different error ellipsoids. In the LVLH frame with respect to the target, the target's error ellipsoid is directly oriented with respect to the axes and it always remains that way since the basic idea that the ellipsoids are assumed to be aligned with the body axes is still maintained. However, orienting the error ellipsoid of the chaser is not an easy task. As the orientation of the ellipsoid depends directly on the absolute velocity and position of the body, it is not enough for us to know the relative velocity of the chaser with respect to the target. Therefore, it is necessary to obtain the absolute velocity of the chaser by adding to the relative velocity the absolute velocity of the target as well as the drag term due to the rotational frame. Once the orientation is known, the error ellipsoid can be generated and then rotated to the target's LVLH frame.

From this moment on, the ellipsoids can be added as well as the combined body is generated and the method begins to execute as always, starting first by generating the principal reference frame.

For the following comparison between the calculation provided using Keplerian propagation and propagation using the HCW equations, a target in a circular orbit with a radius of 30,000 km and a chaser with a semi-major axis of 29,390 km approximately and eccentricity of 0.03 was simulated. To simplify the encounter point, both orbits are in the same orbital plane. The properties of the target's orbit are very similar to those of a satellite of the European GALILEO positioning network. Likewise, a radius of the combined hardbody of 5m has been taken as a reference, which would correspond approximately to two GALILEO satellites without taking into account the solar panels.

The encounter occurs with a miss distance of approximately 100 meters and the initial measurement is taken approximately at a relative distance of 1000 meters. From that moment on, the bodies are propagated, simultaneously with the Keplerian model and the HCW equations, and the probability of collision is computed until the bodies are separated again 1000 meters. The encounter, under these conditions, lasts approximately 16 seconds.

A series of simulations were carried out for a range of uncertainties in position with a standard deviation σ of 5 to 60 meters. The results obtained with the HCW equations were compared with the ones obtained by the Keplerian propagation.

The standard deviation in each body axis has been considered different. Based on uncertainty data present in real cases [30], an uncertainty along each body axis has been simulated as follows in both bodies:

$$\Sigma = \begin{bmatrix} \sigma^2 & 0 & 0 \\ 0 & (1.4\cdot\sigma)^2 & 0 \\ 0 & 0 & (1.1\cdot\sigma)^2 \end{bmatrix} \tag{5.1}$$

Figure 5.1 shows the cumulative collision probability value through both propagations for different reference standard deviation values and Figure 5.2 shows the relative error. Said relative error values are also collected in Table 5.1.

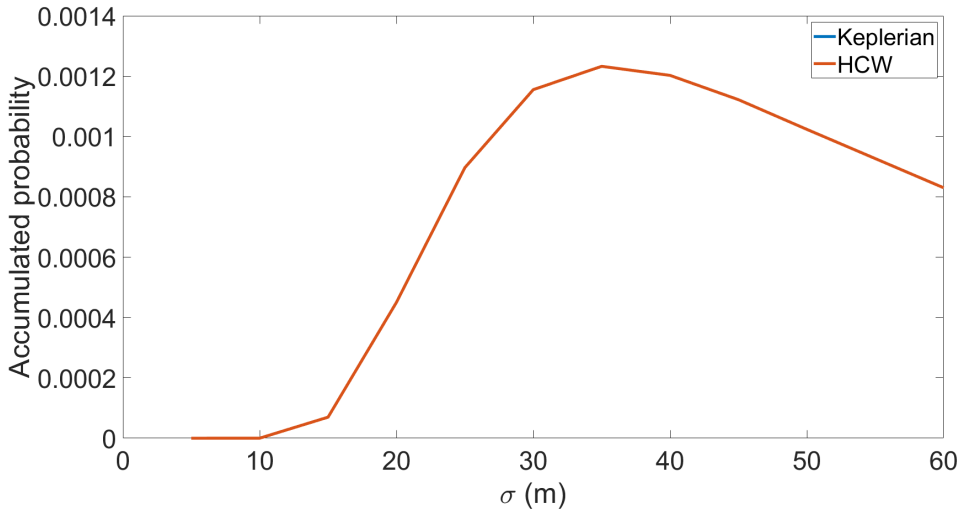

Figure 5.1 Accumulated probability for different values of the reference standard deviation.

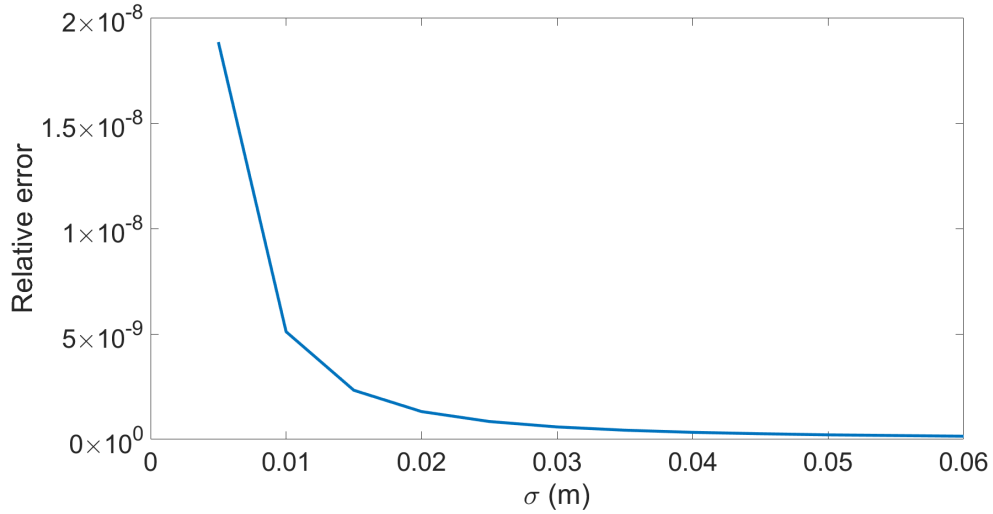

Figure 5.2 Relative error between Keplerian and HCW propagation for for different values of the reference standard deviation.

Table 5.1 Relative error between Keplerian and HCW propagation for for different values of the reference standard deviation.

Standard deviation (m)	Rel. error
5	1.88e-8
10	5.1e-9
20	1.31e-9
30	5.89e-10
40	3.32e-10
50	2.13e-10
60	1.49e-10

It is observed that, regardless of the standard deviation values considered, the HCW equations guarantee a very precise result. The decrease in relative error as the uncertainty increases is due to the fact that the probability of collision inside the uncertainty region is less concentrated and therefore the positional discrepancies between the different propagators are diluted.

5.2 Analysis of the effect of velocity uncertainty

Up to this point, we have analyzed an encounter between bodies whose mean position was known continuously over time but with a certain uncertainty in their position measurement. However, in reality, the measurements are not continuous but are carried out every certain time step. This implies that, in the period between measurements, the trajectory is not really known. This, however, can be estimated using a propagator, which takes as initial values the position and velocity values of the last measurement, that propagates until the next instant of update of values.

However, just as there is uncertainty in the measurement of position, there is of course also uncertainty in the measurement of velocity. This implies that the propagation of the mean position is not ideal, and therefore that this position probability cloud does not remain constant but grows over time. In this way, the greater the uncertainty in the velocity measurement, the more rapidly the position probability cloud will grow as the body propagates until a new position measurement is obtained and the original size is returned.

The covariance matrix, therefore, becomes a symmetric 6x6 matrix. However, an initial diagonal shape is still maintained in the body axes to standardize the calculation.

From real data, the conclusion was drawn that the uncertainties present in the velocity measurement are distributed in a similar way to those present in position in terms of magnitude in each axis. They are usually of an order proportional to 10^{-3} of the different standard deviations of each axis.

From the previous section the conclusion was drawn that, for this defined encounter, a standard deviation greater than $35 meters$ implies entering the dilution zone. Therefore, and since the uncertainty will grow under what has just been explained, in this section the same encounter will be studied, set at a standard deviation in position of 25 meters. The standard deviation in velocity along each axis will be proportional to it with 10^{-3} resulting in the following initial covariance matrix in body axes:

$$\Sigma = \begin{bmatrix} \sigma^2 & 0 & 0 & 0 & 0 & 0 \\ 0 & (1.4\cdot\sigma)^2 & 0 & 0 & 0 & 0 \\ 0 & 0 & (1.1\cdot\sigma)^2 & 0 & 0 & 0 \\ 0 & 0 & 0 & (10^{-3}\cdot\sigma)^2 & 0 & 0 \\ 0 & 0 & 0 & 0 & (1.4\cdot 10^{-3}\cdot\sigma)^2 & 0 \\ 0 & 0 & 0 & 0 & 0 & (1.1\cdot 10^{-3}\cdot\sigma)^2 \end{bmatrix} \tag{5.2}$$

Under the initial conditions of the covariance matrix just presented (5.2) and using equation (3.21), the covariance matrix was propagated (assuming zero noise) up to a series of minutes. This time is defined as uncertainty time because it refers to the time during which the covariance has been allowed to grow in the absence of an update. Figures 5.3 and 5.4 show the growth of the region of positional uncertainty graphically ($3\sigma region$).

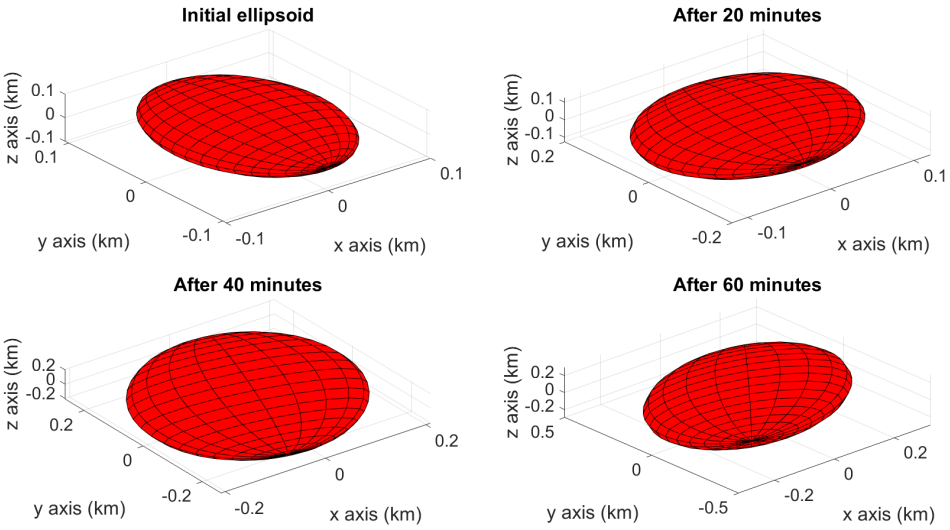

Figure 5.3 Growth of the 3σ region of positional uncertainty for several minutes (0 to 60 minutes).

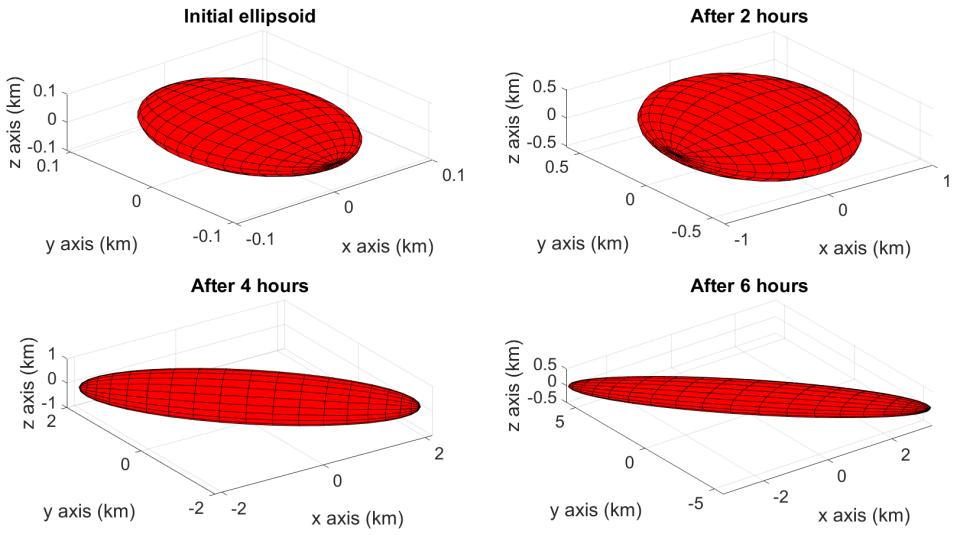

Figure 5.4 Growth of the 3σ region of positional uncertainty for several minutes (0 to 6 hours).

It is observed that, as time passes, the ellipsoid inevitably increases in size. Being related to the form of the solution of the HCW equations, the dimensions along the x and z axes increase but they do so periodically. What is unavoidable is the limitless growth along the y-axis. A change in orientation of the ellipsoid is also observed. It stops being oriented according to the body axes since extra diagonal covariance terms appear.

5.2.1 Updates during the encounter

Given the encounter under the same conditions as in the previous section, and for an initial covariance matrix on each body equal to (5.2) with a standard deviation of 25 meters, the collision probability values will be obtained for different **update steps**. That is, during the propagation time that is given by the time interval during which the combined body is within the 3σ region, the number of times the relative position has been updated and so the values of the covariance matrix are restored. The HCW equations will be used as a propagator.

It should be noted that in reality this idea would not make much sense. The satellite operator estimates the probability of collision hours / days before the possible encounter and decides whether to carry out an avoidance maneuver or not. Once it has been decided not to perform the maneuver, the recalculation of the probability of collision does not contribute anything since no action can be taken. However, such analysis has been carried out to observe how drastically decreasing uncertainty affects the pdf.

Figure 5.5 shows the collision probability density function for each instant of time. Although the encounter was said to last approximately 16 seconds (1000 meters), for these initial standard deviation conditions the relevant region has been limited to 6 seconds (400 meters).

The red dots represent the instants in time in which the size of the error positional ellipsoid is restored to its original size and orientation.

Figure 5.6 shows the relative error of the cumulative probability with respect to the ideal case. It is observed, obviously, that as the number of updates grows, the error tends to zero. These data are shown in more detail in Table 5.2.

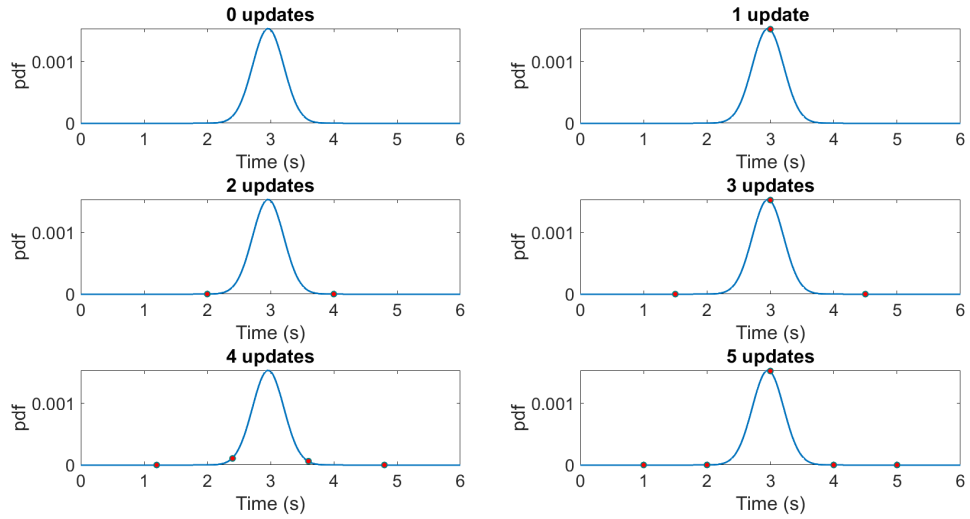

Figure 5.5 Evolution of the pdf when making updates in the middle of the encounter ($\sigma_{velocity} = 25\ mm/s$).

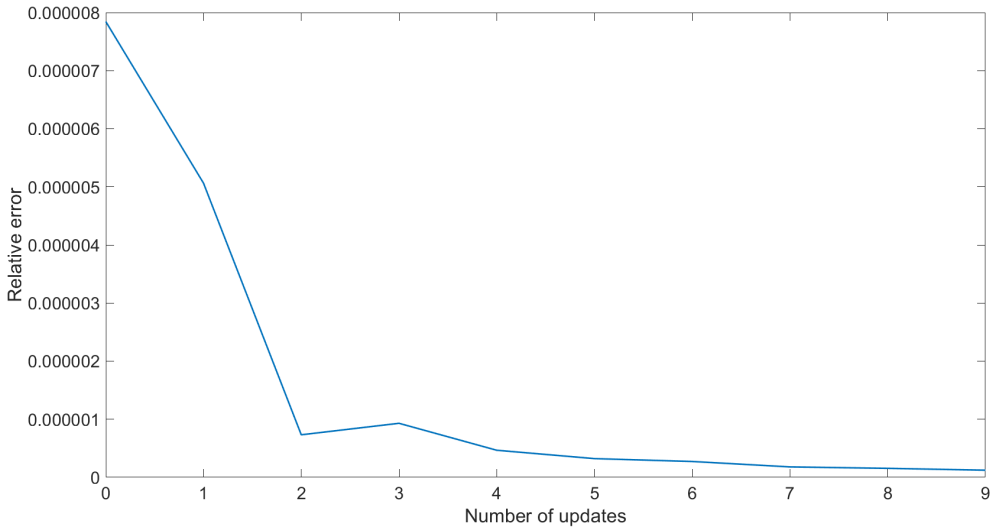

Figure 5.6 Relative error of the cumulative probability for different number of updates ($\sigma_{velocity} = 25\ mm/s$).

Table 5.2 Relative error of the cumulative probability for different number of updates ($\sigma_{velocity} = 25\ mm/s$).

Number of updates	Rel. error
0	7.84e-6
1	5.06e-6
2	7.32e-7
3	9.3e-7
4	4.66e-7
5	3.22e-7
6	2.72e-7
7	1.79e-7
8	1.54e-7
9	1.23e-7

Because the time considered is very small and the uncertainties in velocity are moderate, it is not possible to truly appreciate in Figure 5.5 what happens when the values are updated. That is why, for the same encounter, the same analysis was simulated but considering uncertainty in the velocity of the same order as the uncertainties in position. That is, a standard deviation in velocity of the order of 25 m/s (90 km/h). The result is shown in Figure 5.7.

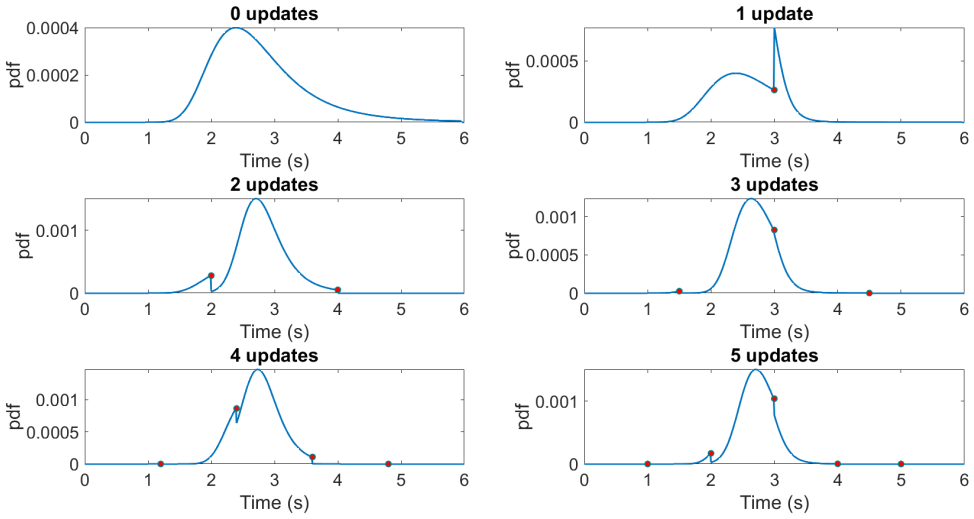

Figure 5.7 Evolution of the pdf when making updates in the middle of the encounter ($\sigma_{velocity} = 25\ m/s$).

It is observed how as the number of updates increases, the probability density function looks more and more like the one shown in Figure 5.5.

When no updates are made, the pdf does not reach the maximum values that it should reach. This is because the ellipsoid grows so large that the dilution region is quickly reached and the probability of collision tends to zero. In contrast, when performing an update just in the middle of the meeting, the correct values are restored and the pdf returns to provide high values.

A curious phenomenon can also be observed in the first and second update respectively of the cases with 2 and 5 updates: with the update the pdf decreases to zero. This is due to the fact that ideally for said relative distance and nominal size of the uncertainty region the probability is close to zero as shown in Figure 4.19. However, as the uncertainty region has been allowed to grow, it has been penetrated and therefore a non-zero probability appears that is reduced to zero when updated.

5.2.2 Propagation of uncertainty before the encounter

This previous analysis has been very useful to understand how the growth of the uncertainty region affects during the meeting. However, even without updates during the encounter, the result hardly varies for moderate values of standard deviation. This is due to the low time of encounter considered, and further reinforces the idea developed in Section 4.4.4 that the region of uncertainty can be "frozen" during the encounter without losing the quality of the results.

A final simulation is therefore carried out. At a certain number of minutes before the encounter, a last update of the values is received and from that moment the region of uncertainty starts to grow. Just when entering the region delimited by 3σ, the uncertainty region is frozen, and the collision probability is computed. The same initial conditions for position, orbit, and standard deviation taken up to now were considered.

Figure 5.8 shows the evolution of the accumulated probability values as the time without updates increases, as well as the relative error with respect to the ideal case (0 minutes of uncertainty).

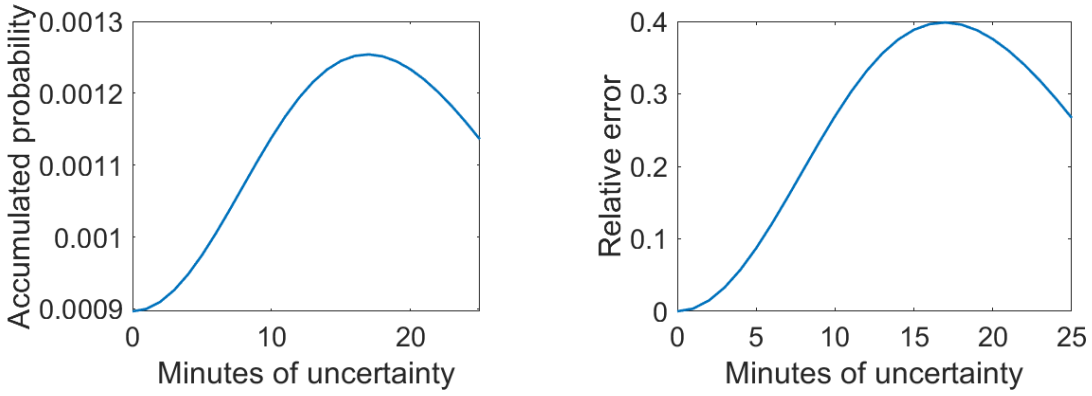

(a) Accumulated probability values.

(b) Relative error.

Figure 5.8 Evolution of the accumulated probability values as the time without updates increases and its relative error (0-25 minutes).

It is observed how without growth time the relative error is null but as the time without updates increases, the probability of collision begins to increase until reaching the maximum. This is because standard deviation values were conveniently chosen that would guarantee to be outside the dilution zone even if the uncertainty region grew slightly. In this way, the behavior is correct: as the quality of the data deteriorates (uncertainty is greater), the probability of collision increases. This is something that can perfectly happen in reality due to the presence of noise, lack of vision, or communication and the behavior must be like this. However, around 12 minutes without updating, the dilution zone is entered and the results lose meaning, not being useful anymore.

It is also interesting to know, given a maximum permissible relative error, what idle time values can be allowed. For this, a simulation was made taking into account inactivity periods of the order of seconds until approximately a relative error of 10% was exceeded. Figure 5.20 shows the results and the relative error is shown in Table 5.3.

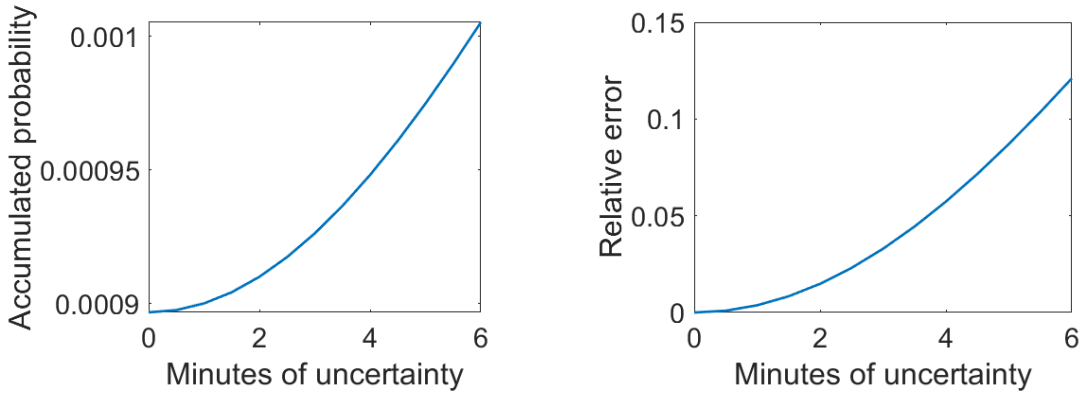

Figure 5.9 Evolution of the accumulated probability values as the time without updates increases and its relative error (0-6 minutes).

Hence, for our particular encounter, up to a couple of minutes without receiving updates can be tolerated guaranteeing 98-99% of accuracy. However, relative errors grow very rapidly at an exponential rate, so exceeding 5-6 minutes without updates generates an error of more than 10%.

Table 5.3 Relative error as the time without updates increases (0-6 minutes).

Minutes without updates	Rel. error	Accuracy
0	0	100%
1	3.73e-3	99.63%
2	1.48e-2	98.52%
3	3.29e-2	96.71%
4	5.73e-2	94.27%
5	8.71e-2	91.29%
6	1.21e-1	87.9%

5.3 Analysis of the effect of perturbations

Until this moment the trajectory of the bodies had been ideally propagated. However, in this section, we will consider the effect of perturbations.

Being the case that we are studying a satellite in a circular orbit with an orbit radius of 30,000km, it is possible to ignore some perturbations. From Figure 2.7, the conclusion drawn is that there is no atmospheric friction. In addition, it is observed that the perturbation of greater magnitude is the effect of the non-sphericity of the Earth. On the other hand, the rest of the perturbations have an effect that is not important but that should not be dismissed lightly.

However, as far as we are concerned, the propagation that we are going to carry out involve periods of the order of minutes. That is why, given the great leap in magnitude of the non-spherical effect with the rest of the perturbations, this will be the only perturbation that we will take into account. In addition, we will specifically study the effect of J_2. A more exhaustive study and with another type of orbit should include the rest of the perturbations.

First, we are going to propagate the orbit of our study target for a few minutes with the J_2 model and we are going to observe the discrepancy in position obtained with respect to the ideal case. The result is shown in Figure 5.10.

It is observed that, as time increases, the discrepancy in position with respect to the ideal case grows exponentially. Although a couple of minutes is not enough to noticeably disturb the orbit, after 20 minutes the position has been completely distorted. This highlights the need to model perturbations to correctly propagate the position of a body.

However, we are not interested in the absolute position of the bodies, but their relative position. It happens that, in the region close to the encounter, both bodies are in different orbits but at a very similar point in space. Therefore, practically the same effect that a perturbation has on the

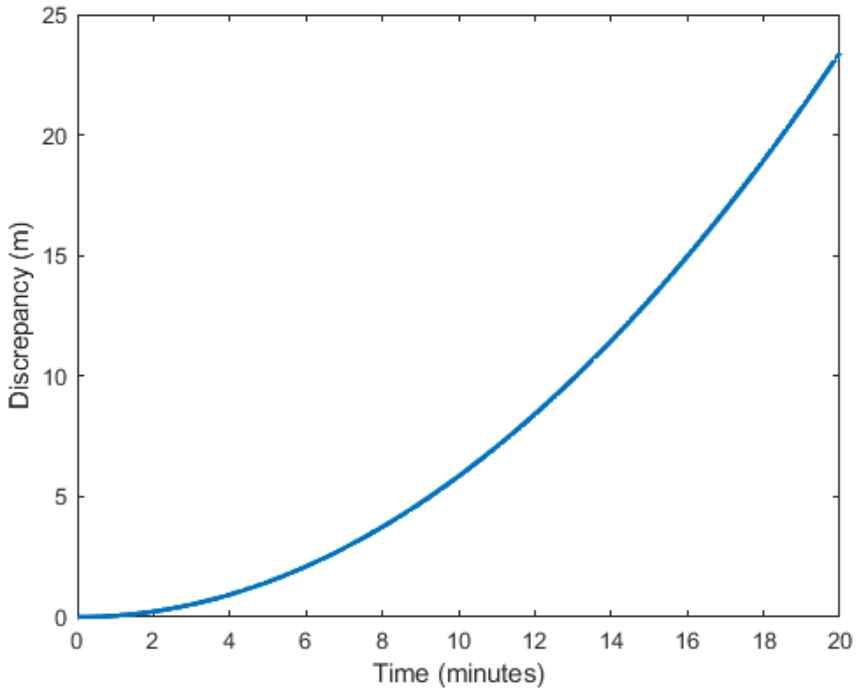

Figure 5.10 Discrepancy in the position of a body after propagating it in a Keplerian vs non-Keplerian orbit taking J_2 into account.

target is also carried out on the chaser, with the relative distance being practically unchanged as a result. Figure 5.11 shows the discrepancy in the relative distance under the same conditions of the previous propagation.

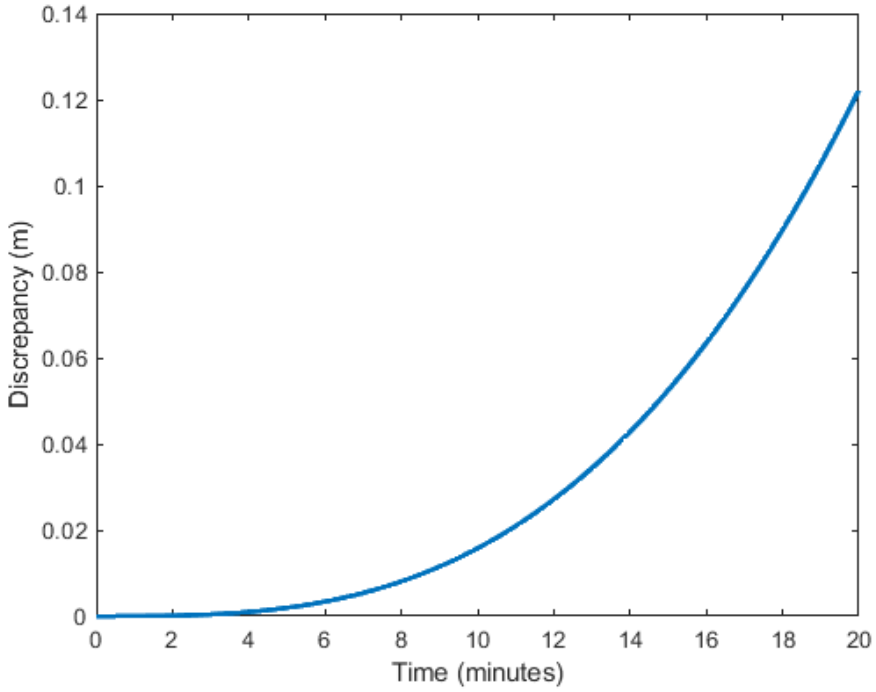

Figure 5.11 Discrepancy in the relative position of two close bodies after propagating them in a Keplerian vs non-Keplerian orbit taking J_2 into account.

Therefore, a comparison of the collision probability in the ideal case will be carried out together with the case with perturbations considering the uncertainty frozen within the interval 3σ but which has been evolving for a certain number of minutes.

Having defined the J_2 perturbation in the inertial geocentric system and introduced it directly into the non-linear equation of motion (2.28), it is not possible to propagate the covariance matrix linearly with the HCW equations directly as we did in the previous section. The solution to be able to study the perturbations with a linear propagator is to linearize these perturbations. However, it is a tedious and very mathematical process, and we can reuse the powerful tool of the Monte Carlo method to find a practical solution.

5.3.1 Monte Carlo propagation of the covariance matrix

The idea to propagate the covariance matrix using the Monte Carlo method and the non-linear propagator is as follows. A cloud of points will be generated and these will be propagated individually with the absolute propagator with perturbations (J_2 model). At each instant of time until the end of the propagation, the positional covariance matrix will be computed corresponding to the current positions of the different points. Thus, we can make the uncertainty region grow for a certain number of minutes taking into account the effect of the perturbations.

First of all, to verify this idea, the difference between linearly propagating the uncertainty region with HCW equations and doing it with a Monte Carlo simulation has been verified in the undisturbed case. Figure 5.12 shows geometrically the positional uncertainty ellipsoid after letting it grow/propagating the points for 60 minutes.

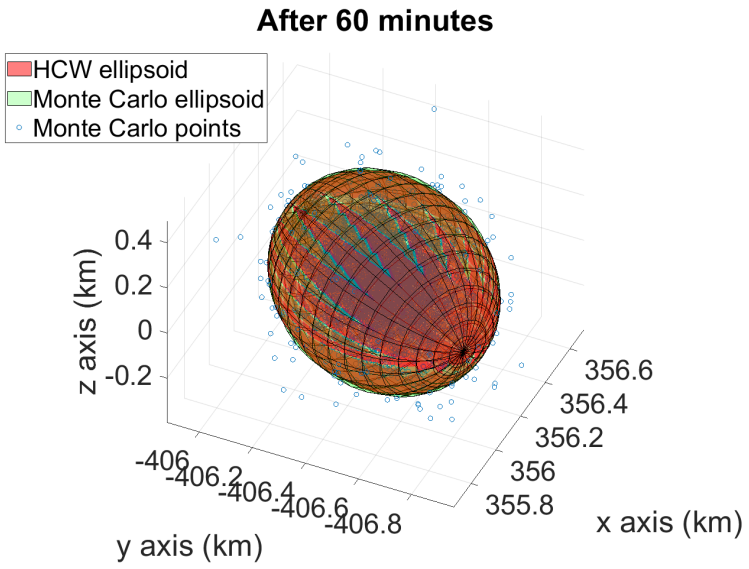

Figure 5.12 Comparison between the positional error ellipsoid obtained with the HCW equations and the Monte Carlo method (60 minutes).

We observe an overlap between the two ellipsoids. Similarly, a test was made by propagating the error ellipsoid for 6 hours. It does not make physical sense because in reality an uncertainty of so many hours completely loses its value and also it would not make sense to apply linear equations for so long, but it was done mainly to appreciate the precision of this idea and how the result is hardly distorted despite the enormous lengthening of the region. The result is shown in Figure 5.13.

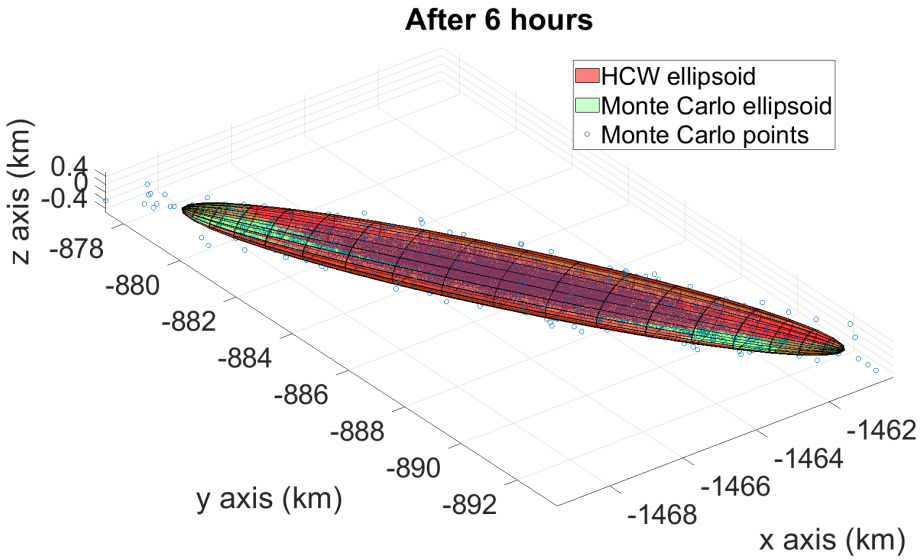

Figure 5.13 Comparison between the positional error ellipsoid obtained with the HCW equations and the Monte Carlo method (6 hours).

To generate the previous figures, a point cloud of around 10,000 points was used. Theoretically, with an infinite number of points, both regions should coincide. Similarly, the fewer points we generate, the discrepancy between the regions grows. The number of points to be generated depends on the physical limitation of the computation.

Taking this into account, the cumulative collision probability was computed for different values of uncertainty propagation time. The result obtained by linearly propagating the covariance matrix was compared with the one obtained by propagating the covariance matrix with the Monte Carlo method for different number of points generated. In Figures 5.14, 5.15, 5.16 and 5.17 it can be observed, respectively, the comparison of the results when generating 1.000, 2.500, 5.000 and 10.000 points.

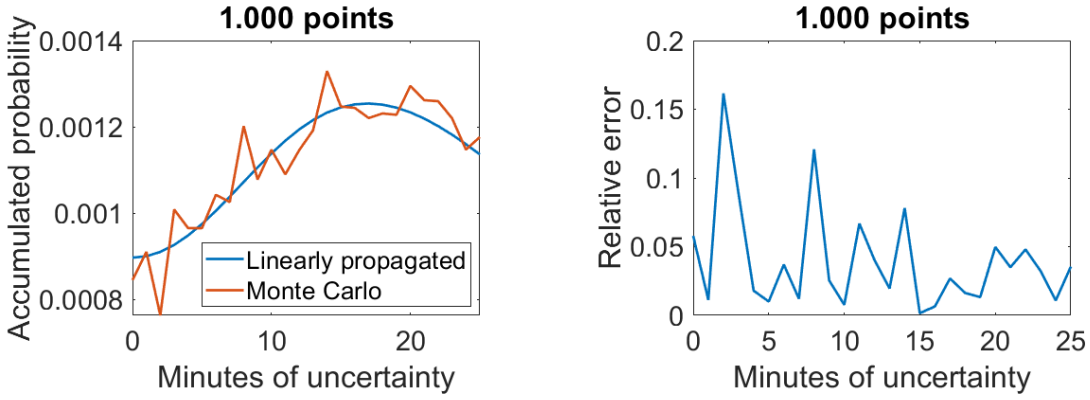

Figure 5.14 Cumulative probability as a function of the uncertainty time obtained by linearly propagating the covariance matrix vs using the Monte Carlo method (1.000 points).

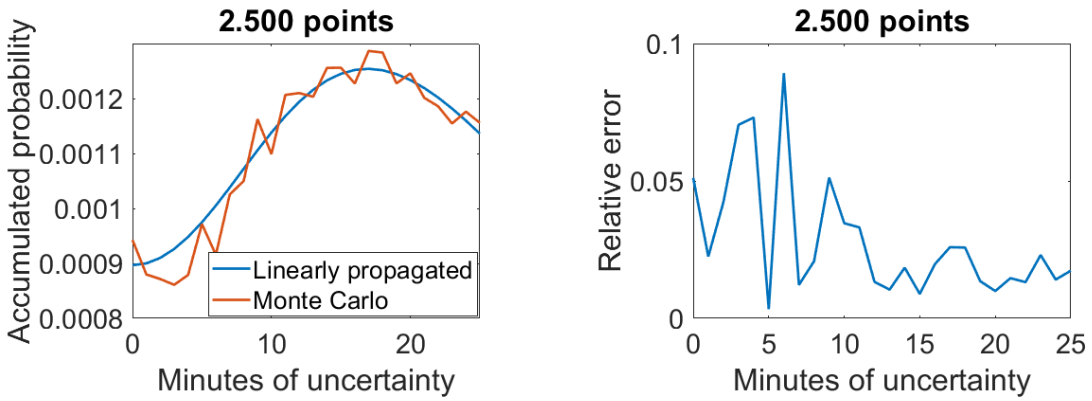

Figure 5.15 Cumulative probability as a function of the uncertainty time obtained by linearly propagating the covariance matrix vs using the Monte Carlo method (2.500 points).

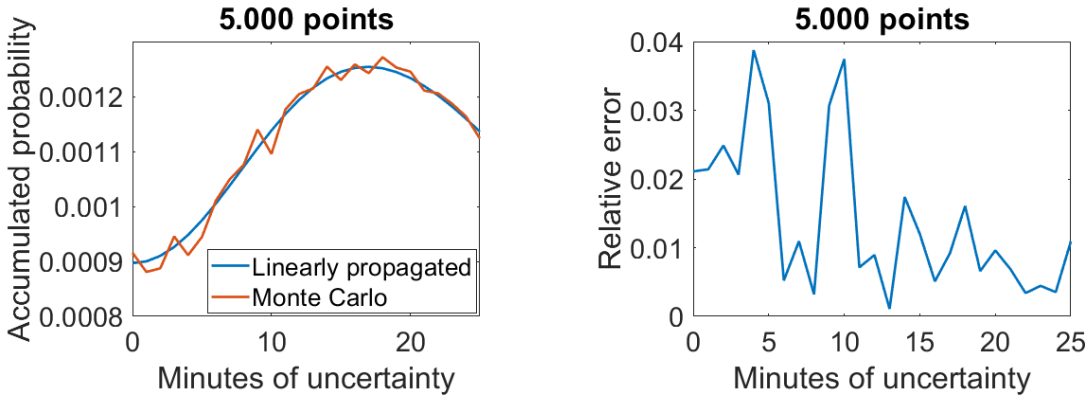

Figure 5.16 Cumulative probability as a function of the uncertainty time obtained by linearly propagating the covariance matrix vs using the Monte Carlo method (5.000 points).

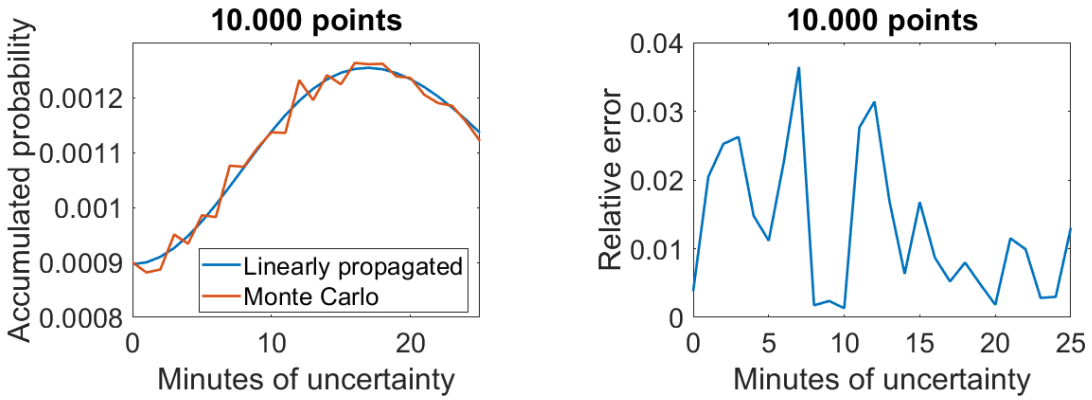

Figure 5.17 Cumulative probability as a function of the uncertainty time obtained by linearly propagating the covariance matrix vs using the Monte Carlo method (10.000 points).

It is observed how, as the number of points increases, the solution obtained by the Monte Carlo method approaches the real solution. Although with 1.000 points average errors of 5-10 % are reached with respect to the exact solution, with 10,000 points the errors drop to 1-2 %.

Likewise, it is worth noting how the accuracy grows logarithmically. From 1.000 to 2.500 points the errors fall almost in half. However, from 5.000 to 10.000 points the errors remain practically

constant. As happened when analyzing in Section 4.3 the experimental method by Monte Carlo with the analytic one, despite excessively increasing the number of points, the errors were never zero and ended up stagnating.

This last paragraph along with the conclusion drawn from these simulations is essential to understanding what will be done next. First, it is clear that in the absence of linearization of the perturbed equations to analytically propagate the covariance matrix, a Monte Carlo simulation with a large number of points can be used without incurring much error. On the other hand, this error is due to the randomness of the point cloud. In the previous figures it is observed that despite the increase in the propagation time of the uncertainty, the Monte Carlo method oscillates around the analytical result. This is due to the fact that a different point cloud is generated at each instant of time that tends to generate a probability of impact slightly higher or lower than the exact one. Thus, the error is not made when propagating the points but when generating the cloud of points.

Therefore, to compare the relative error made by not considering the perturbations, the same cloud of points will be used that is propagated well ideally well considering the J_2, to which its uncertainty region will be calculated. In this way, we, therefore, isolate the dependence on the number of points and focus exclusively on the error made by considering the J_2 or not. Figures 1, 2 and 3 show the results, respectively, generating 1,000, 2,000 and 5.000 points.

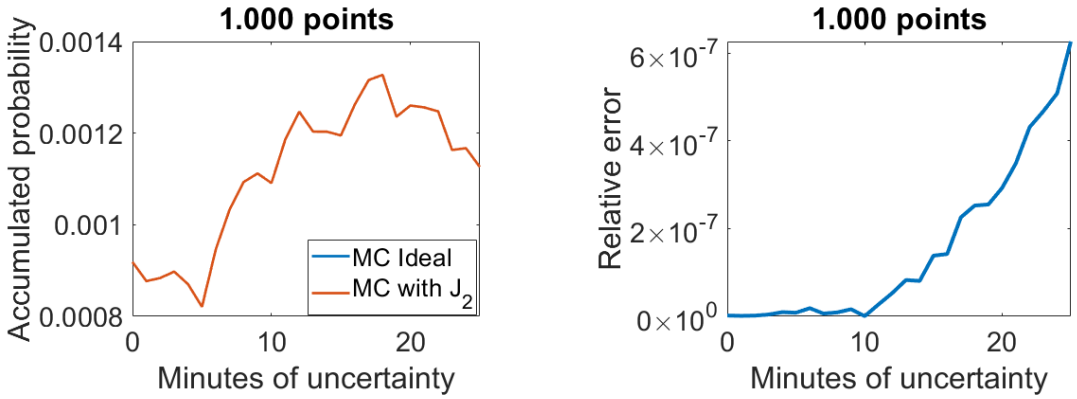

Figure 5.18 Cumulative probability as a function of the uncertainty time obtained by ideally propagating the cloud of points vs considering the J_2 (1.000 points).

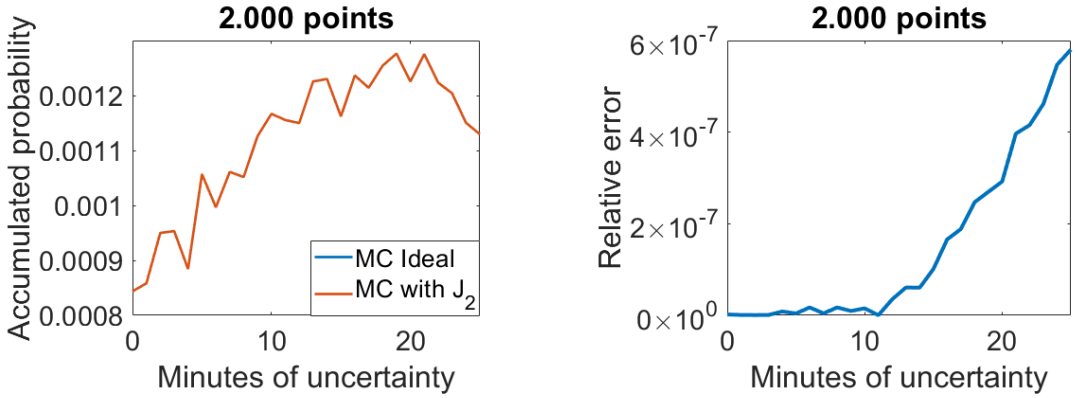

Figure 5.19 Cumulative probability as a function of the uncertainty time obtained by ideally propagating the cloud of points vs considering the J_2 (2.000 points).

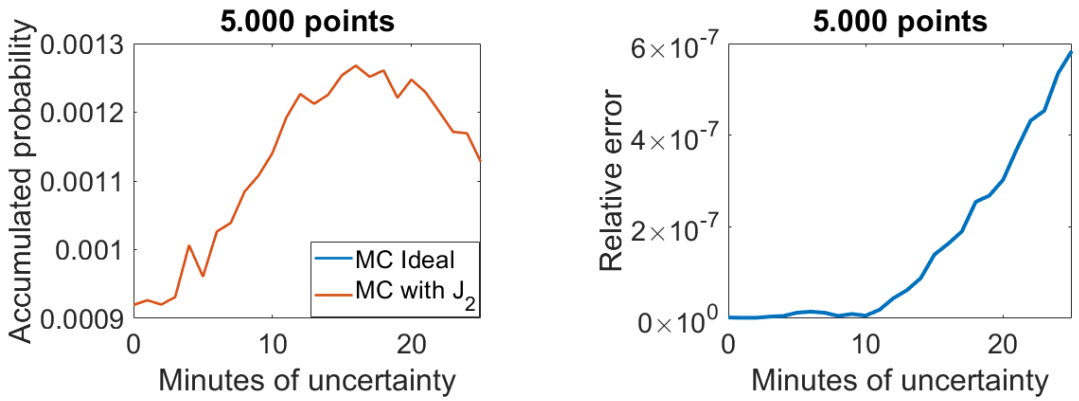

Figure 5.20 Cumulative probability as a function of the uncertainty time obtained by ideally propagating the cloud of points vs considering the J_2 (5.000 points).

It is clearly observed how varying the number of points hardly affects the result and also, what is more surprising, how little relevance it has to consider the effect of J_2. This agrees with what was previously analyzed and how, although the absolute positions in a few minutes take a discrepancy of the order of meters, in the case of the relative position the discrepancy is of the order of centimeters.

To observe the growth of the errors, the same simulation was carried out up to 150 minutes. Figure 5.21 shows the result.

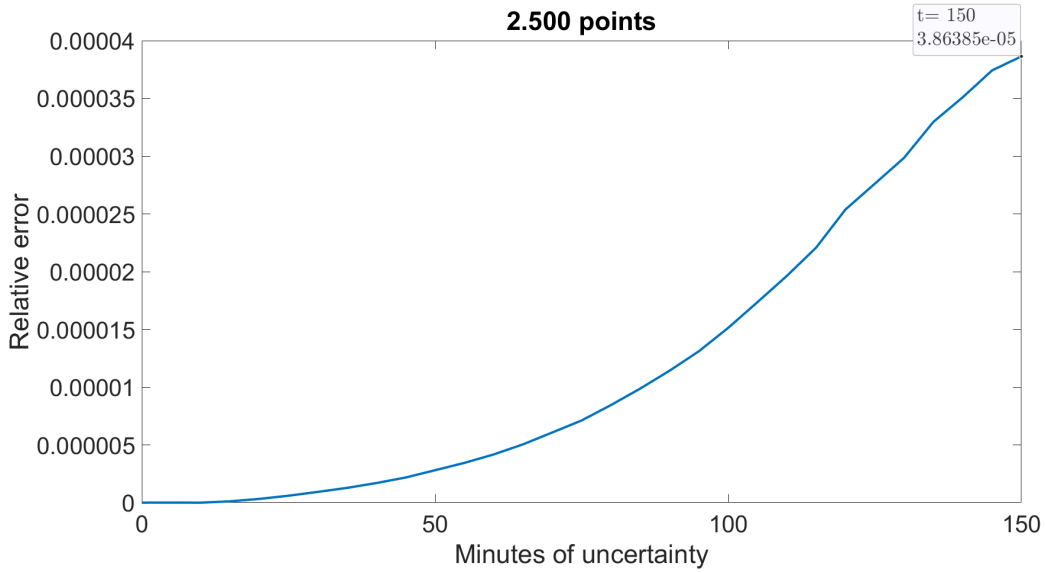

Figure 5.21 Relative error in cumulative probability for different uncertainty times when propagating the cloud of points ideally vs considering the J_2.

We have not studied the effect of other minor perturbations such as the rest of harmonics due to the non-sphericity of the Earth or luni-solar perturbations, and its justification is clear. J_2 is the most powerful perturbation under our conditions and only produces an error of the order of 10e-7. Then, the effect of the rest of the perturbations with a much smaller order of magnitude would produce an even smaller discrepancy in result. Therefore, we can ensure that for our specific case, the perturbations, including the J_2, can be neglected without committing a relevant mistake.

It would not be the same, however, if we had studied a low orbit. In these conditions, the effect of the atmospheric drag is very powerful and also depends on the absolute speed of each body and not on the region of space as happened with the J_2. Therefore, its effect should be taken into account.

In any case, one way of being able to take into account the effect of a perturbation without explicitly modeling it is by introducing a Gaussian white noise in the velocity measurement. In this way, one does not know exactly the region of uncertainty and what is done is to increase its

size due to the lack of data. An example of the increase in positional uncertainty that could be generated by not taking drag into account is shown in Figure 5.22 and the effect in the uncertainty of velocity is shown in Figure 5.23.

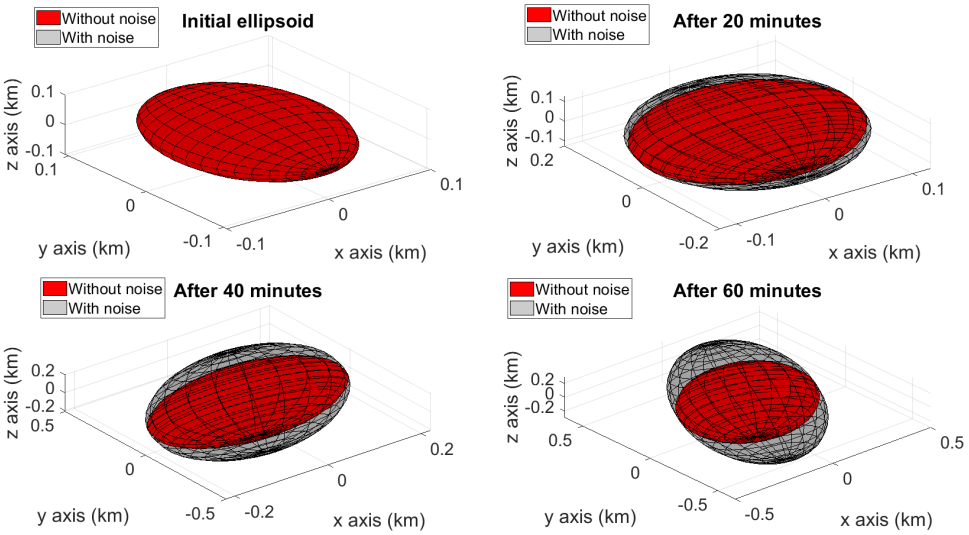

Figure 5.22 Additional growth of the region of position uncertainty due to the consideration of Gaussian white noise in the measurement of the velocity.

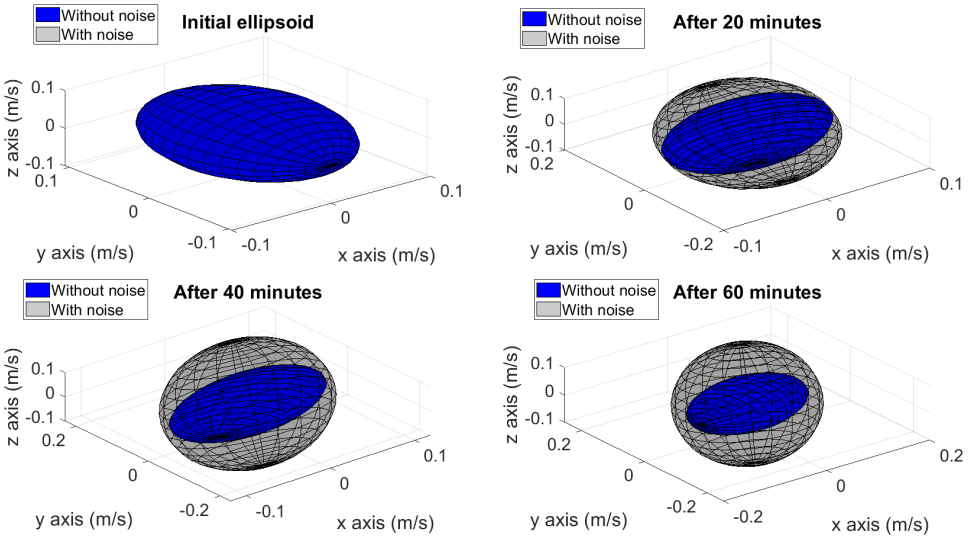

Figure 5.23 Additional growth of the region of velocity uncertainty due to the consideration of Gaussian white noise in the measurement of the velocity.

As drag is a predominant effect in the direction of movement, and not considering it should lead to an increase in uncertainty mainly along the said axis (y-axis according to body axes). In this way, we are taking into account that the position may be more or less ahead of the account and is penalized with an increase in the probability of collision (as long as we do not enter the dilution region). An accurate study of the perturbation would be rewarded by a decrease in the probability of collision.

5.4 Analysis of the limits of the HCW equations with non-circular targets

The HCW equations are restricted to targets in circular orbit. However, they may be used for targets in low eccentricity orbits without incurring major errors. In this way, in this section we will analyze the eccentricity limits for which the HCW equations can be used and how the error made affects the estimated collision probability.

First, the error made when using the HCW equations for different eccentricity values of the target is analyzed. As the analysis is quite complex since the precision of these equations not only depends on the eccentricity but also on the orbital radius, the initial relative distance and the average orbital speed of the bodies, a standard case will be analyzed.

Both cases have the following details in common: The chaser's eccentricity will be fixed to $e_c = 0.15$ and its semi-major axis a will be the same than the one of the target. At the initial instant the bodies start from the same point, that is, what would correspond to the point of intersection of the orbits. The bodies will be propagated for 5 minutes (300 seconds) and discrepancy values will be obtained between the real relative position (obtained by propagating the bodies with the Keplerian propagator) and the one estimated using the HCW equations.

Two satellites in MEO orbit with a semi-major axis of $a = 30.000$ kilometers are studied firstly under the above conditions. The results are shown in Figure 5.24.

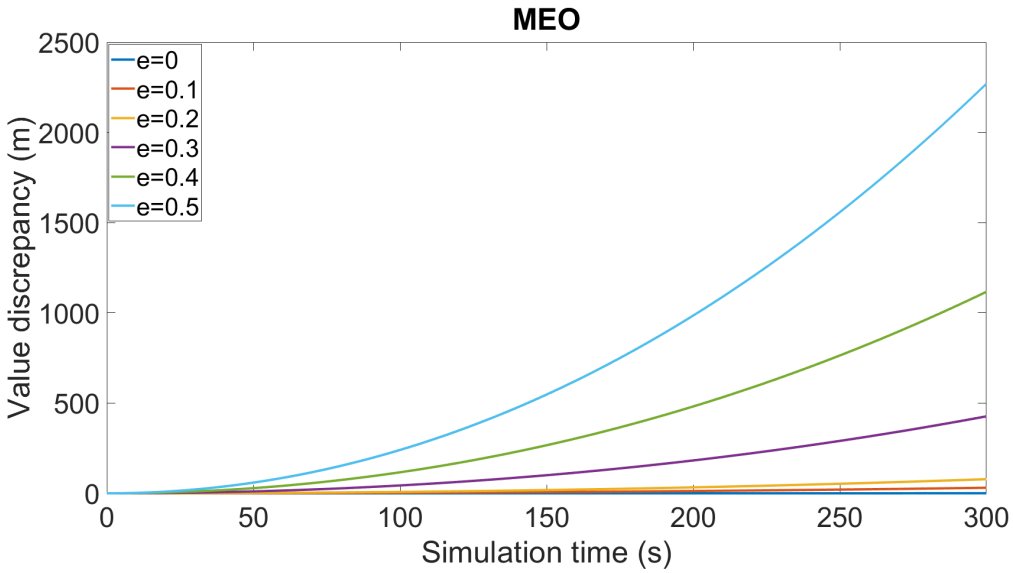

Figure 5.24 Discrepancy in position for different eccentricity values between 0 and 0.5 for two satellites in MEO.

For eccentricity values between 0 and 0.2, an acceptable accuracy is maintained. Furthermore, as the eccentricity increases, the discrepancy is greater. In Figure 5.25 target eccentricities lower than 0.2 are analyzed in greater detail.

For the case of eccentricity equal to zero, the HCW equations show high accuracy with a discrepancy of only 29 centimeters. However, as the eccentricity increases, the discrepancy increases until with $e = 0.2$ a discrepancy of 78 meters is committed. Taking into account the conditions of standard deviation of 25 meters and the combined hardbody radius of 5 meters, an inaccuracy of such a gauge completely invalidates its use.

It is worth highlighting the fact that with $e = 0.16$ there is less error than with $e = 0.04$. And that is due to the conditions of the chaser ($e_c = 0.15$) and the condition of starting at the point of intersection with the same semi-major axis. If the eccentricity of the target were $e = 0.15$, the initial conditions of position and velocity would be equal to zero since both orbits would be the same. In that case the discrepancy would always be null since all the values would be 0. In the cases where the eccentricity is not the same, but very similar, and their semi-major axis is the same, it happens that the orbits are alike. Therefore, they will present low initial relative velocity values,

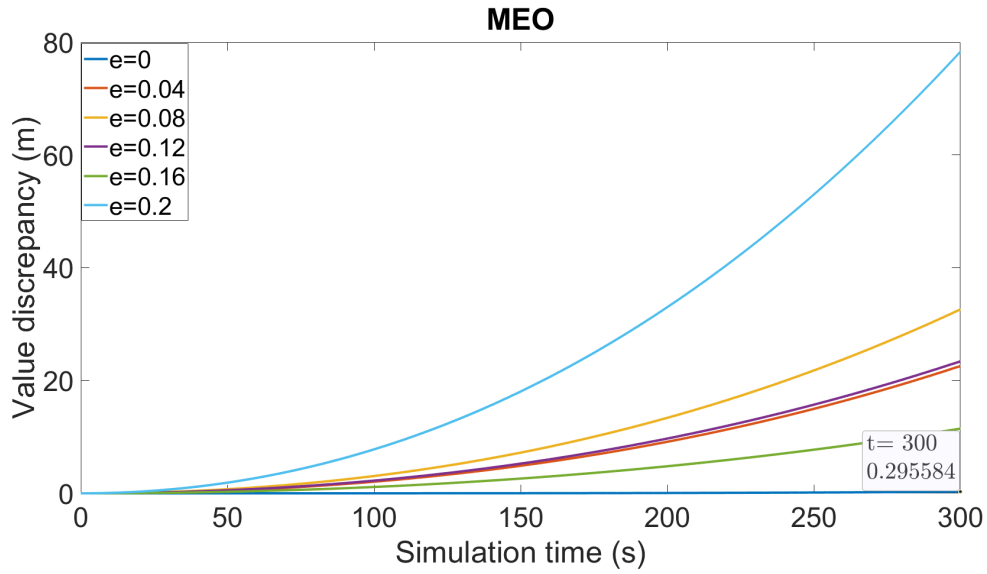

Figure 5.25 Discrepancy in position for different eccentricity values between 0 and 0.2 for two satellites in MEO.

which according to the linear solution (2.36) is translated into a slower evolution and consequently a discrepancy that grows at a slower rate.

To complete the analysis, the same study was carried out under the same conditions but for two satellites in LEO, that is, with a semi-major axis of $a = 8.000$ kilometers. As already shown in Figures 2.10 and 2.11, for low orbits the average orbital speed n is higher and therefore the bodies separate faster. For this reason, under the same interval, the discrepancy in LEO will be higher than the one estimated in MEO. Figure 5.26 shows the results.

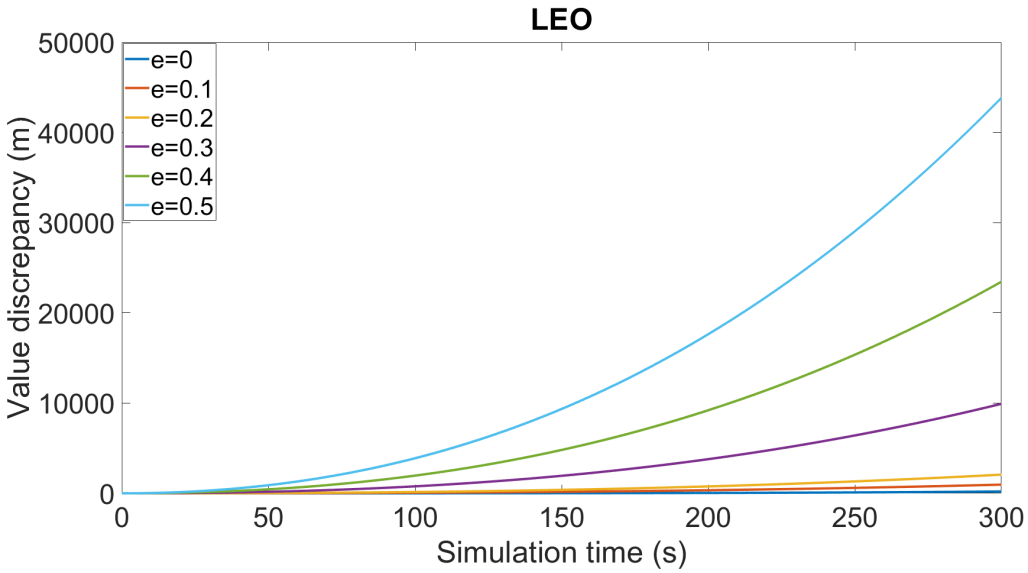

Figure 5.26 Discrepancy in position for different eccentricity values between 0 and 0.5 for two satellites in LEO.

Despite the fact that the discrepancy is much greater, its evolution as a function of propagation time and eccentricity is identical to that shown in Figure 5.24. Figure 5.27 shows the detailed results for eccentricity values lower than $e = 0.2$.

An almost identical order to that of Figure 5.25 is presented and the explanation is the same. It is surprising how, in the case of zero eccentricity and the same propagation time, the error made

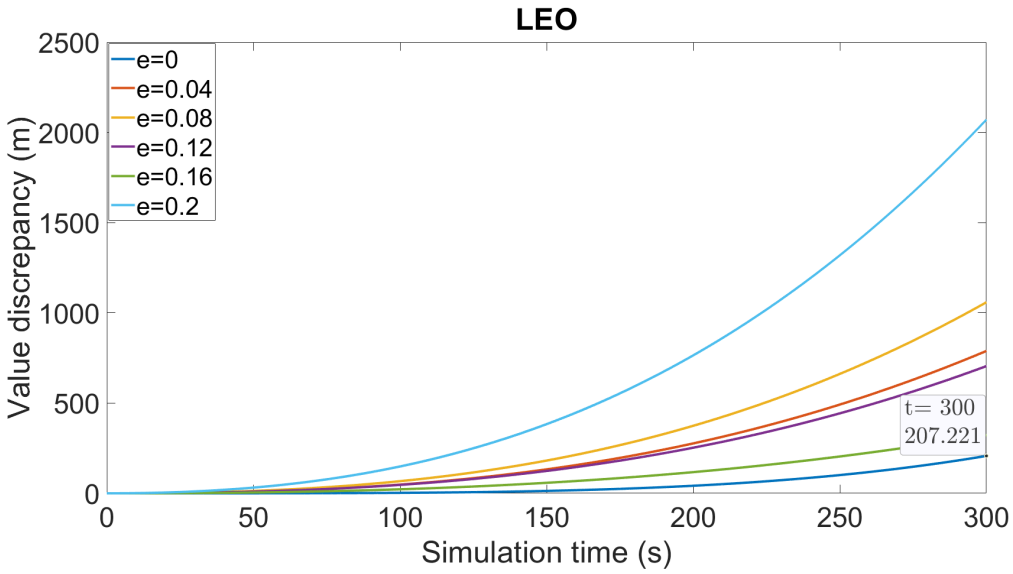

Figure 5.27 Discrepancy in position for different eccentricity values between 0 and 0.2 for two satellites in LEO.

has gone from 29 centimeters to 207 meters. This implies that the equations are not valid, for said propagation time, nor for the case of null eccentricity. The solution is to restrict the equations to a lower propagation time or use a better propagator.

After the previous analysis, a comparison of the estimated collision probability is made. To compare the results, the solution obtained with the HCW equations (both by propagating the position and the covariance matrix) will be compared with that obtained by propagating the positions with the Keplerian propagator (both the positions and the covariance matrix using the method of Monte Carlo).

The conditions of uncertainty and combined body radius will be the same as those of the previous sections. However, the miss distance will be practically zero. The initial data is assumed to be provided 5 minutes (300 seconds) before the instant of minimum relative distance and during that time the position and covariance matrix will be propagated. A very tight propagation time has been chosen due to the relative distance limitations of the HCW equations shown in the previous analysis. The comparison made for the satellites in MEO is shown in Figure 5.28.

Having used only 3,000 points in the Monte Carlo propagation, the estimated collision probability varies for the different eccentricities. However, they oscillate around the same value, showing high accuracy but low precision.

Likewise, and in accordance with what is shown in Figure 5.25, as the eccentricity increases, the estimated probability decreases (since the discrepancy in position increases and therefore the miss distance ceases to be near zero). However, for values close to $e = 0.15$, it seems that the solution again coincides with the real one, justifying what has already been stated. Finally, as the eccentricity increases, the estimated probability drops sharply.

Due to the difficult isolation of the error made when using the HCW equations with targets in non-circular orbits, it is hard to previously guarantee an allowable eccentricity value without making the appropriate estimates. However, a conclusion can be drawn: the higher the initial relative velocity between the bodies, the greater the error made. In part, it makes sense since the higher the relative speed the faster they separate and the more errors are made. And eccentricity has an indirect effect on speed.

It has been shown that for the same semi-major axis, close eccentricity values between the bodies guarantee greater precision. However, one wonders what happens if the semi-major axes are different. In that case, keeping the eccentricity of the chaser constant, there will be a value of the eccentricity of the target that in combination will produce an encounter at low relative speed

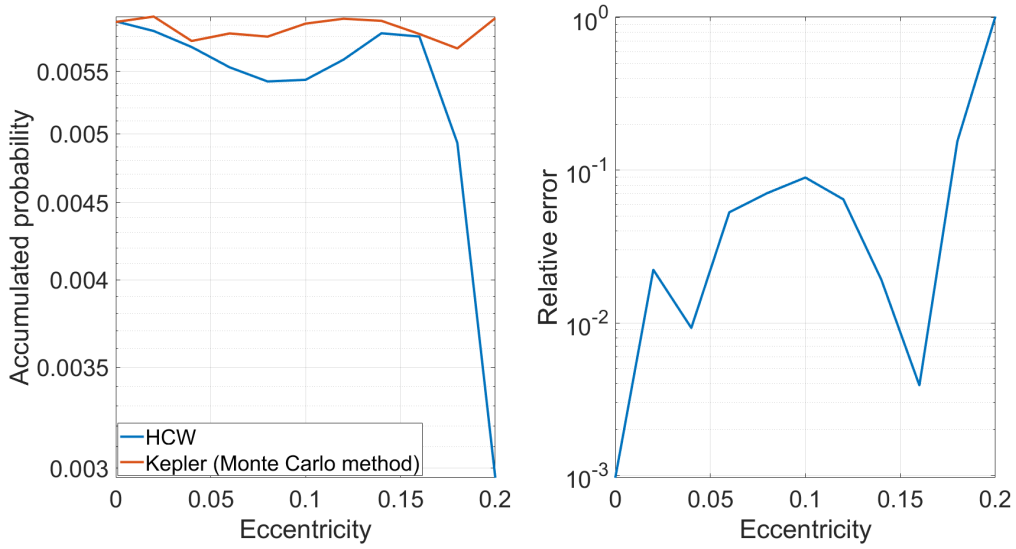

Figure 5.28 Estimated collision probability and relative error when using the HCW equations for satellites in MEO with a target in non-circular orbit for different eccentricity values.

and therefore the discrepancy will be small compared to the values obtained for eccentricities in its environment.

Nevertheless, apart from these special cases, it is proved that the greater the eccentricity considered, the greater the error made since these equations treat the target as if it were in a circular orbit.

6 Conclusions and future work

6.1 Conclusions

Throughout this project, some basic touches have been given of what the study of the probability of collision between orbiting bodies entails. However, it is an extremely complex subject and some aspects have been left uncovered.

In the first place, the method proposed by Patera is taken as a basis. While it is apparently a very robust method, it is a method that is strengthened by its assumptions. Hypotheses, which in reality are not fulfilled. A clear example is the fact that in order to develop the method and access the encounter plane, for example, it is necessary to know with accuracy the direction and orientation of the relative velocity. However, in reality the velocity can never be known without uncertainty. Instead, an average velocity is estimated.

Furthermore, the method is constructed considering a constant covariance matrix and assuming that the position is known at all times. This is another quite unrealistic hypothesis but which is nevertheless necessary to be able to pose the method. However, as has been performed after introducing the method, it is possible to add variations that bring it closer to reality. It is possible, for example, to be able to work with covariance matrices that vary at each instant of time or adapt this method to a different propagator such as the HCW equations.

Therefore, it is a good method that can be taken as a study base and subject to variations that allow a more realistic approach.

To extend the method, the HCW equations have been used extensively. The main reason for their use is that they have a linear solution, they are quite simple and also greatly reduce computing time. Thanks to these equations, it has been possible to propagate the covariance matrix with relative ease, speed and accuracy, while the Monte Carlo method has been subject to inaccuracies and long process times.

However, its use is quite limited. Although the effect of perturbations does not induce much more error in these equations than it does in Kepler equations, the relative distance of the bodies is critical. In addition to the serious limitation of only being able to study targets in circular or very slightly eccentric orbit, depending on the orbital segment they can only be used to propagate bodies for a couple of minutes without losing accuracy. Therefore, they are very powerful and useful equations to study encounters between bodies at low relative speed that are kept in close proximity (as in GEO), but they are not useful for studying fast encounters and much less for propagating bodies and uncertainty for hours or days before the encounter, what really needs to be done to ensure the safety of the satellite.

One of the most important results extracted from this work is the idea of the dilution region. One tends to think that as the lack of knowledge about a disastrous event increases, the more dangerous it becomes. And this is what happens under nominal conditions. However, in the particular case of the probability of collision, there comes a time when the less information we have, the more safe we feel, becoming a real ostrich paradox.

Therefore, this dilution region must always be taken into account and avoided at all costs as within this region whatever estimated value loses its usefulness. Although as discussed in Section 4.4.1 there are some methods to deal with this problematic, there is still no solution and the only remedy is to insist on more recent and accurate data.

Another important aspect extracted from this work is the importance of the type of orbit when computing the probability of collision. It is not the same to study the risk of collision between two satellites in low orbits than between two satellites in high orbits.

Depending on the type of encounter, it will last more or less time, and this will lead to a greater or lesser spread of uncertainty. Likewise, while in LEO, bodies will generally pass quickly in a couple of seconds or minutes, an encounter between two satellites in GEO can last for hours and involve relative trajectories that curve and intertwine. Furthermore, in the case of using the HCW equations as a propagator, it has been seen how the height of the orbit influences the limits of applicability.

In the same way, the segment of the satellite to be protected marks the types of perturbations to be considered. Bodies in low orbit will be subject to different perturbations than those of higher orbits. Although some perturbations such as the ones due to the non-spherical gravitational field of the Earth have the only complexity of the mathematical aspect, others such as atmospheric drag are highly dependent on the position, orientation and velocity of the body, subject to uncertainty and increasing it even more.

However, it should be noted that two bodies that meet are generally going to suffer perturbations of the same magnitude and direction. This slightly relaxes the importance of considering them in a short-term encounter since, as we have seen in Section 5.3, the discrepancy in the absolute position is compensated. However, for encounters of long duration and / or that start with the bodies very far apart, it is undoubtedly necessary to take them into account.

6.2 Future work

Although a general analysis of the basic problem of the collision between two bodies in space has been carried out, many fronts have been left open and issues undeveloped.

Firstly, the use of a Gaussian distribution. It has been justified by means of the *Central Limit Theorem* that it is a good distribution to use for modelling the problem of uncertainty. However, an alternative distribution, a variation, or the imprecision present in making such a hypothesis could have been analyzed in depth. Likewise, bodies in space are rarely spherical. Although approximating them as spheres is the best way to treat them from a didactic and conceptual point of view, there are enough tools to deal with all kinds of forms.

Another important aspect is the development of the process for capturing, analyzing and verifying the position and velocity data obtained. During this project they have been assumed as known initial data. However, obtaining them is not an easy process and is subject to numerous inaccuracies. The project could have been completed with a thorough analysis of this procedure.

Given that the objective of the project was to analyze the subject of collision risk in general, and all its implications, the type of orbit has not been a determining factor. That is why it has been possible to work with target orbits with zero eccentricity and therefore the HCW equations have been used. However, facing an exhaustive analysis and especially a standardization of a method or program that allows calculating values for any type of orbit, these equations fall short.

The alternative of a linear propagator that can operate with non-circular target orbits are the Tschauner-Hempel equations [31]. Said equations, despite presenting greater mathematical complexity than those of HCW, are subject to fewer restrictions and are currently widely used in rendezvous and collision problems between nearby bodies.

Furthermore, in order to develop a standardize method, it would be necessary to model all the perturbations. Currently there are the so-called *Simplified perturbations models*, often referred as SGP4 [32], used to calculate orbital state vectors of satellites and space debris relative to the inertial geocentric reference frame. These models predict the effect of perturbations caused by the

Earth's shape, drag, radiation, and gravitation effects from other bodies such as the sun and moon. An inclusion of these models in the method would solve the problem of perturbations.

Another fundamental aspect that must be addressed is the limits that mark the need to execute an evasion maneuver as well as when and how to perform it. The usual criteria consists on exceeding a collision probability threshold or a safety distance. Regarding to the optimal evasion maneuver problem, the current formulation allows to reduce it to an eigenvalue problem coupled to a simple nonlinear algebraic equation [33]. The optimization criterion consists of minimizing the maneuver cost in terms of delta-V magnitude to either maximize collision miss distance or to minimize Gaussian collision probability. In any case, the study of said maneuver for different scenarios would complement the subject of this project and the aspects mentioned in Section 1.1.3 would be covered.

Bibliography

[1] David Wright. Space debris. *Physics Today*, 60:35–, 10 2007.

[2] Tyler Reid. *Orbital Diversity for Global Navigation Satellite Systems*. PhD thesis, 06 2017.

[3] Toni Veikkolainen. *Database-wide studies on the validity of the Geocentric Axial Dipole hypothesis in the Precambrian*. PhD thesis, 10 2014.

[4] Salvatore Alfano and Daniel Oltrogge. Probability of collision: Valuation, variability, visualization, and validity. *Acta Astronautica*, 148:301–316, 2018.

[5] Vázquez Valenzuela. Mecánica orbital y vehículos espaciales tema 4.

[6] Sascha Metz. *Master Thesis: Implementation and comparison of data-based methods for collision avoidance in satellite operations*. PhD thesis, 07 2020.

[7] Brian Weeden. 2007 chinese anti-satellite test fact sheet. *Secure World Foundation*, 11 2010.

[8] Kelso TS. Analysis of the iridium 33 and cosmos 2251 collision. *Advanced Maui Optical and Space Surveillance Conference*, 09 2009.

[9] James S. Cooney. International space station (iss) orbital debris collision avoidance process. 10 2016.

[10] Michael Kalinski. Hypervelocity impact analysis of international space station whipple and enhanced stuffed whipple shields. page 299, 12 2004.

[11] Kenneth R Meyer. *Periodic solutions of the N-body problem*, volume 1719. Springer Science & Business Media, 1999.

[12] Demostración matemática de las leyes de kepler [mathematical proof of kepler's laws]. *https://ingenieriabasica.es/demostracion-matematica-leyes-de-kepler/*. Accessed: 2021-04-29.

[13] G. W. Hill. Researches in the lunar theory. *American Journal of Mathematics*, 1(1):5–26, 1878.

[14] W. H. Clohessy and R. S. Wiltshire. Terminal guidance system for satellite rendezvous. *Journal of the Aerospace Sciences*, 27(9):653–658, 1960.

[15] Michael J. Evans and Jeffrey S. Rosenthal. *Probability and Statistics: The Science of Ucertainty*. New York: W.H. Freeman Co., University of Toronto, 2010.

[16] 3σ rule for multivariate normal distribution. *https://math.stackexchange.com/questions/143377/3-sigma-rule-for-multivariate-normal-distribution*. Accessed: 2021-05-05.

[17] Sang Kwak and Jong Kim. Central limit theorem: The cornerstone of modern statistics. *Korean Journal of Anesthesiology*, 70:144, 04 2017.

[18] Svetlana Strbac-Savic, Ana Miletic, and Hana Stefanović. The estimation of pi using monte carlo technique with interactive animations. 10 2015.

[19] E Maten, T Doorn, J Croon, A Bargagli, Alessandro Di Bucchianico, and Olaf Wittich. Importance sampling for high speed statistical monte-carlo simulations, 11 2009.

[20] Rafael Vázquez Valenzuela and Francisco Gavilán Jiménez. Fundamentos de navegación aérea tema 8.

[21] G.E. Peterson. Comparison of collision risk from cola and kinetic gas theory for sun-synchronous orbits. 120:299–315, 01 2005.

[22] Salvatore Alfano. Review of conjunction probability methods for short-term encounters. *Advances in the Astronautical Sciences*, 127:719–746, 01 2007.

[23] Russell Patera. General method for calculating satellite collision probability. *Journal of Guidance Control and Dynamics - J GUID CONTROL DYNAM*, 24:716–722, 07 2001.

[24] Russell Patera. Collision probability for larger bodies having nonlinear relative motion. *Journal of Guidance Control and Dynamics - J GUID CONTROL DYNAM*, 29:1468–1472, 11 2006.

[25] Sever S Dragomir, Pietro Cerone, and Anthony Sofo. Some remarks on the trapezoid rule in numerical integration. *RGMIA research report collection*, 2(5), 1999.

[26] Russell Patera. Satellite collision probability for non-linear relative motion. *Journal of Guidance Control and Dynamics - J GUID CONTROL DYNAM*, 26:728–733, 09 2003.

[27] B. W. Silverman and D. M. Titterington. Minimum covering ellipses. *SIAM Journal on Scientific and Statistical Computing*, 1(4):401–409, 1980.

[28] Russell Patera. Calculating collision probability for arbitrary space vehicle shapes via numerical quadrature. *Journal of Guidance Control and Dynamics - J GUID CONTROL DYNAM*, 28:1326–1328, 11 2005.

[29] Michael Balch. A corrector for probability dilution in satellite conjunction analysis. 01 2016.

[30] H. Klinkrad, J. Alarcon, and Noelia Sánchez-Ortiz. Collision avoidance for operational esa satellites. *European Space Agency, (Special Publication) ESA SP*, 587:509, 07 2005.

[31] Koji Yamanaka and Finn Ankersen. New state transition matrix for relative motion on an arbitrary elliptical orbit. *Journal of Guidance Control and Dynamics - J GUID CONTROL DYNAM*, 25:60–66, 01 2002.

[32] David Vallado and Paul Crawford. Sgp4 orbit determination. 08 2008.

[33] Claudio Bombardelli and Javier Hernando-Ayuso. Optimal impulsive collision avoidance in low earth orbit. *Journal of Guidance, Control, and Dynamics*, 38:217–225, 02 2015.